

UC Davis

UC Davis Electronic Theses and Dissertations

Title

Computer Vision System and Experiment Design for Parabolic Flight Demonstration of Hard Disk Drives as CubeSat Reaction Wheels

Permalink

<https://escholarship.org/uc/item/0jk146tn>

Author

Cooper, Kylie Rae

Publication Date

2023

Peer reviewed|Thesis/dissertation

Computer Vision System and Experiment Design for Parabolic Flight
Demonstration of Hard Disk Drives as CubeSat Reaction Wheels

By

KYLIE RAE COOPER

THESIS

Submitted in partial satisfaction of the requirements for the degree of

MASTER OF SCIENCE

in

Mechanical and Aerospace Engineering

in the

OFFICE OF GRADUATE STUDIES

of the

UNIVERSITY OF CALIFORNIA

DAVIS

Approved:

Stephen K. Robinson, Chair

Sanjay S. Joshi

Richard S. Whittle

Committee in Charge

2023

CONTENTS

List of Figures	v
List of Tables	x
Abstract	xii
Acknowledgments	xiii
1 Introduction	1
1.1 Overview	1
1.2 Hard Disk Drives Repurposed as Reaction Wheels	2
1.3 Technology Readiness Level (TRL) Motivation	4
1.4 HDD-RW Testing Process	5
1.5 NASA Tech Flights Grant	7
2 Experiment Methodology	8
2.1 Introduction	8
2.2 Background	9
2.2.1 Aircraft Environment	9
2.2.2 Flight Profile	10
2.3 Experiment Design	13
2.3.1 Goal Definition	13
2.3.2 Hardware Overview	13
2.3.3 Test Case Definition	19
3 Computer Vision System Design	27
3.1 Introduction	27
3.2 Fiducial Marker System Design	27
3.2.1 Introduction	27
3.2.2 Fiducial Marker Selection	28
3.2.3 ArUco Dictionary Selection	30
3.2.4 ArUco Board	31
3.2.5 Laser Engraving Markers	32

3.3	Camera System Design	33
3.3.1	Introduction	33
3.3.2	Camera Selection	34
3.3.3	Camera Placement	37
3.3.4	Camera Reference Frame Definition	40
3.3.5	Calibration	40
3.4	Computer Vision System Ground Testing	58
3.4.1	Introduction	58
3.4.2	Experiment Procedure	58
3.4.3	Ground Testing Results	63
3.4.4	Operating Range Selection	77
3.4.5	Ground Testing Conclusions	78
3.4.6	Ground Testing Limitations	79
4	CubeSat Testbed In-Flight Attitude Estimation and Validation	80
4.1	Introduction	80
4.2	Reference Frame Conversion	81
4.2.1	Introduction	81
4.2.2	Cameras A-D to Chamber Reference Frame Conversion	81
4.2.3	Chamber IMUs Reference Frames Definitions	88
4.2.4	Cameras A-D to Inertial Reference Frame Conversion	91
4.3	Extended Kalman Filter Overview	95
4.3.1	Introduction	95
4.3.2	State Space Model	96
4.3.3	Extended Kalman Filter Design	97
4.3.4	Sensor Characterization	99
4.3.5	EKF Results	104
4.4	CubeSat Testbed Attitude Estimation Conclusions	114
4.5	CubeSat Testbed Attitude Estimation Limitations	115

5	Conclusion	116
5.1	Summary of Contributions	116
5.2	Lessons Learned	117
5.2.1	Experiment Methodology	117
5.2.2	Computer Vision System Design	118
5.2.3	CubeSat Testbed In-Flight Attitude Estimation and Validation . . .	118
5.3	Future Work	119
	Appendices	125
A	Experiment Design	126
A.1	CubeSat Testbed Electrical Schematics	126
A.1.1	CubeSat Testbed A	126
A.2	Chamber Drawings	129
A.3	CV System Electrical Schematics	133
B	Extended Kalman Filter Design	134
B.1	Matrix A Definition	134

LIST OF FIGURES

1.1	Commercial reaction wheel and HDD-RW cost vs. momentum storage comparison	3
1.2	TRL scale	5
2.1	G Force One Aircraft	9
2.2	Aircraft cabin environment	10
2.3	G Force One aircraft flight profile	11
2.4	CubeSat testbed hardware	14
2.5	Chamber installed in Zero-G aircraft	16
2.6	Computer Vision system hardware	17
2.7	Zero-G HDD-RW Experiment Layout	19
2.8	Flight Campaign 1 Hardware and Researcher Layout (Top View)	21
2.9	Zero-G HDD-RW Experimenters Performing Linear Ramp Experiment in FC1	22
2.10	Flight Campaign 2 Hardware and Researcher Layout (Top View)	24
2.11	Zero-G HDD-RW Experimenters Performing Stabilization Experiment in FC2	24
2.12	Flight Campaign 3 Hardware and Researcher Layout (Top View)	26
2.13	Zero-G HDD-RW Experimenters Performing Pointing Experiment in FC3 . .	26
3.1	Example Fiducial Markers: ARTag, AprilTag, and ArUco	29
3.2	ArUco marker size comparison	30
3.3	CubeSat testbed with ArUco board detected and estimated testbed axes drawn	32
3.4	ArUco face manufacturing: laser engraving single pass	33
3.5	Assembled ArUco faces	33
3.6	Camera configuration comparison	38
3.7	Calibration target with checkerboard corners detected (indicated with colored circles) and rows detected (indicated with straight lines connecting like-colored circles)	44
3.8	Camera Calibration Procedure	45

3.9	CubeSat testbed mounted on tool flange of UR5e robot arm and positioned in front of Camera E	59
3.10	Coordinate system definition for robot arm, CubeSat testbed, and Camera E	59
3.11	Robot arm in zeroed position (left) and close-up view of zeroing touch plate (right)	60
3.12	Zeroing touch plate to Camera E Measurements	61
3.13	CubeSat testbed experiment pose set	62
3.14	Summary of CV system ground testing procedure	63
3.15	CV system ground testing: measured distance versus ground truth distance .	64
3.16	CV system ground testing: measured distance error	65
3.17	CV system ground testing: distance measurement noise at 25% of the chamber's diagonal	67
3.18	CV system ground testing: CV system measured angle vs. ground truth angle	70
3.19	CV system ground testing: measured angle versus ground truth angle	71
3.20	CV system ground testing: measured angle error	72
3.21	CV system ground testing: angle measurement noise at 25% of the chamber's diagonal	74
3.22	CV system ground testing: measured distance error within specified operating range	77
3.23	CV system ground testing: measured angle error within specified operating range	78
4.1	Chamber Coordinate System Definition	82
4.2	CubeSat testbed trajectory in the chamber reference frame estimated from cameras A-D: Flight 6, CubeSat C1, Trial 1)	83
4.3	CubeSat testbed attitude in the chamber reference frame estimated from cameras A-D: Flight 6, CubeSat C1, Trial 1)	83
4.4	CubeSat testbed attitude in the chamber reference frame estimated from cameras A-D: Flight 6, CubeSat C1, Trial 5)	84

4.5	CubeSat testbed trajectory in the chamber reference frame estimated from cameras A-D: Flight 6, CubeSat C1, Trial 5)	84
4.6	CubeSat testbed attitude in the chamber reference frame estimated from cameras A-D: Flight 6, CubeSat C1, Trial 7)	85
4.7	CubeSat testbed trajectory in the chamber reference frame estimated from cameras A-D: Flight 6, CubeSat C1, Trial 7)	85
4.8	CubeSat testbed attitude in the chamber reference frame estimated from cameras A-D: Flight 6, CubeSat C1, Trial 8)	86
4.9	CubeSat testbed trajectory in the chamber reference frame estimated from cameras A-D: Flight 6, CubeSat C1, Trial 8)	86
4.10	CubeSat testbed attitude in the chamber reference frame estimated from cameras A-D: Flight 6, CubeSat C1, Trial 10)	87
4.11	CubeSat testbed trajectory in the chamber reference frame estimated from cameras A-D: Flight 6, CubeSat C1, Trial 10)	87
4.12	IMU D Rotation and Acceleration Rates in the Chamber Reference Frame: Flight 6, CubeSat C1, Trial 1)	89
4.13	IMU D Rotation and Acceleration Rates in the Chamber Reference Frame: Flight 6, CubeSat C1, Trial 5)	89
4.14	IMU D Rotation and Acceleration Rates in the Chamber Reference Frame: Flight 6, CubeSat C1, Trial 7)	90
4.15	IMU D Rotation and Acceleration Rates in the Chamber Reference Frame: Flight 6, CubeSat C1, Trial 8)	90
4.16	IMU D Rotation and Acceleration Rates in the Chamber Reference Frame: Flight 6, CubeSat C1, Trial 10)	91
4.17	CubeSat testbed attitude in the inertial reference frame estimated from cameras A-D: Flight 6, CubeSat C1, Trial 1)	93
4.18	CubeSat testbed trajectory in the inertial reference frame estimated from cameras A-D: Flight 6, CubeSat C1, Trial 5)	93
4.19	CubeSat testbed trajectory in the inertial reference frame estimated from cameras A-D: Flight 6, CubeSat C1, Trial 7)	94

4.20	CubeSat testbed attitude in the inertial reference frame estimated from cameras A-D: Flight 6, CubeSat C1, Trial 8)	94
4.21	CubeSat testbed trajectory in the inertial reference frame estimated from cameras A-D: Flight 6, CubeSat C1, Trial 10)	95
4.22	Extended Kalman Filter Overview	96
4.23	CubeSat Testbed B Gyroscope Calibration (Presented in Testbed Body Reference Frame)	100
4.24	CubeSat Testbed C1 Gyroscope Calibration (Presented in Testbed Body Reference Frame)	101
4.25	CubeSat Testbed C2 Gyroscope Calibration (Presented in Testbed Body Reference Frame)	101
4.26	Camera D Gyroscope Calibration (Presented in Gyroscope Reference Frame)	103
4.27	CubeSat testbed attitude estimated by EKF: Flight 6, CubeSat C1, Trial 1)	105
4.28	CubeSat testbed attitude (euler angles) estimated by EKF: Flight 6, CubeSat C1, Trial 1)	106
4.29	CubeSat testbed attitude estimated by EKF: Flight 6, CubeSat C1, Trial 5)	107
4.30	CubeSat testbed attitude (euler angles) estimated by EKF: Flight 6, CubeSat C1, Trial 5)	108
4.31	CubeSat testbed attitude estimated by EKF: Flight 6, CubeSat C1, Trial 7)	109
4.32	CubeSat testbed attitude (euler angles) estimated by EKF: Flight 6, CubeSat C1, Trial 7)	110
4.33	CubeSat testbed attitude estimated by EKF: Flight 6, CubeSat C1, Trial 8)	111
4.34	CubeSat testbed attitude (euler angles) estimated by EKF: Flight 6, CubeSat C1, Trial 8)	112
4.35	CubeSat testbed attitude estimated by EKF: Flight 6, CubeSat C1, Trial 10)	113
4.36	CubeSat testbed attitude (euler angles) estimated by EKF: Flight 6, CubeSat C1, Trial 10)	114
A.1	CubeSat Testbed A Electrical Schematic	126
A.2	CubeSat Testbed B Electrical Schematic	127

A.3	CubeSat Testbed C1 & C2 Electrical Schematic	128
A.4	Chamber Isometric View	129
A.5	Chamber Top View	130
A.6	Chamber Middle Bracket	131
A.7	Chamber Corner Bracket	132
A.8	CV System Electrical Schematic	133

LIST OF TABLES

2.1	Zero-G Flight Profile for HDD-RW Experiment	12
2.2	Zero-G Flight Callouts	13
2.3	CubeSat Testbed Summary	15
2.4	CV System Camera Summary	18
2.5	Zero-G HDD-RW Test Case Definition for all Flight Campaigns	20
3.1	CV System Camera Trade Study Summary	36
3.2	Chamber camera configuration study results	39
3.3	Camera calibration results summary	46
3.4	Calibration Results for Camera A (FC1)	47
3.5	Calibration Results for Camera A (FC2)	48
3.6	Calibration Results for Camera B (FC2)	49
3.7	Calibration Results for Camera C (FC2)	50
3.8	Calibration Results for Camera D (FC2)	51
3.9	Calibration Results for Camera A (FC3)	52
3.10	Calibration Results for Camera B (FC3)	53
3.11	Calibration Results for Camera C (FC3)	54
3.12	Calibration Results for Camera D (FC3)	55
3.13	Calibration Results for Camera E (FC3)	56
3.14	Calibration Results for GoPro (FC3)	57
3.15	CV system distance accuracy and standard deviation results (green = lowest absolute value, red = highest absolute value)	69
3.16	CV system angle accuracy and standard deviation results (green = lowest absolute value, red = highest absolute value)	76
4.1	Cameras A-D to Chamber Reference Frame Conversion	82
4.2	Camera IMUs A-D to Chamber Reference Frame Conversion	88
4.3	Gyroscope Measurement Characteristics, Presented in the CubeSat Testbed Body Frame	102

4.4	Camera D Gyroscope Measurement Characteristics, Presented in the Gyro- scope Reference Frame	103
5.1	TRL evaluation of HDD-RW technology after the completion of the Zero-G HDD-RW project	120

ABSTRACT

Computer Vision System and Experiment Design for Parabolic Flight Demonstration of Hard Disk Drives as CubeSat Reaction Wheels

This thesis presents the design of a parabolic flight experiment and the development of the supporting systems to demonstrate hard disk drives functioning as CubeSat reaction wheels. Commercially available CubeSat reaction wheels are costly due to their precise manufacturing requirements, flywheel balancing, and limited amount of vendors. University-built CubeSat reaction wheels can prove to be failure-prone and time-consuming due to the expertise and machinery needed to manufacture, assemble, and test each unit. Through three years of research and testing, the Human/Robotics/Vehicle Integration and Performance (HRVIP) Laboratory in the UC Davis Center for Spaceflight Research (CSFR) developed a low-cost, reliable, readily available solution to the CubeSat reaction wheel cost versus risk trade-off by repurposing hard disk drives (memory storage devices commonly used in laptops) as CubeSat reaction wheels. Testing the Hard Disk Drive Reaction Wheels (HDD-RWs) in parabolic flights allowed for characterization of their performance in the fully unconstrained free-floating environment of microgravity. The design of the parabolic flight experiment system is presented, herein, with a focus on design for human operation and safety in the dynamic flight environment. Five CubeSat testbeds, each containing HDD-RWs, were developed for testing in the parabolic flights, and a supporting computer vision system was designed utilizing ArUco markers for external attitude determination of the CubeSat testbeds. The measurement accuracy and noise of the computer vision system was characterized on-ground through precise placement of the ArUco markers with a UR5e robot arm. Flight data from the computer vision system was integrated into an Extended Kalman Filter and shown to validate the CubeSat testbed onboard attitude determination method. Through the parabolic flight experiment and data validation with the supporting computer vision system, the Technology Readiness Level of the HDD-RWs was raised from TRL 4 (component and/or breadboard validation in laboratory environment) to TRL 6 (system/subsystem model or prototype demonstration in a relevant environment). HDD-RWs were shown to be a promising alternative to commercial and in-house built CubeSat reaction wheels.

ACKNOWLEDGMENTS

I have been extremely fortunate to be part of the the Human/Robotics/Vehicle Integration and Performance (HRVIP) Lab at UC Davis, and to receive the support of many brilliant engineers and wonderful friends as I have pursued my masters degree. In particular, I would like to acknowledge the contributions of the Zero-G HDD-RW team that I have had the pleasure of leading over the course of this project.

To the undergraduate researchers who have worked on this project: this would not have been possible without your support. Ashna Reddy and Miranda Godinez - thank you for believing in this project from the start and for pioneering the design of the chamber and computer vision system. Chris Andrade, Natasha Evans, and Dzuy Nguyen - thank you for your extensive hardware designs and late nights of prototyping, as well as your positive attitudes and unwavering determination. Zoe Wilf and Kelden Ben-Ora - thank you for being ready to tackle any problem we would throw at you, for protecting the chamber, and for bringing the energy we needed to support our final flight campaign.

To Abhay Negi, my project co-lead, thank you for your dedication to the project and your persistence through our many late nights of debugging and countless hours of soldering. No matter the problem, I always knew I could count on you.

To Dr. Robinson - I could not ask for a better adviser; whether it was guiding the direction of the project, sorting our screwdriver kit in the Zero-G hangar, or grabbing brunch to talk about career paths, there is no doubt that you have supported our team in every way possible. More than anything, thank you for encouraging us to take risks and to have fun in everything we do.

And finally, to Chris Andrade and Rachel Pride, the masters students who now take over the development of the HDD-RW technology, thank you for believing in this technology and putting in the effort to get it to orbit. I wish you the best of luck in your work, and look forward to seeing your developments. *Per aspera ad astra.*

Chapter 1

Introduction

1.1 Overview

The work presented in this thesis is the product of the Zero-G Hard Disk Drive Reaction Wheel (HDD-RW) project at the University of California, Davis Center for Spaceflight Research (CSFR). The objective of the Zero-G HDD-RW project was to demonstrate hard disk drives (HDDs) as CubeSat reaction wheels through microgravity parabolic flight testing. This project was awarded the NASA Flight Opportunities Program’s “TechFlights” research grant, which made parabolic flight testing possible. The Zero-G HDD project was led by two masters students, Abhay Negi and the author, and results from the project are presented in two master theses - this thesis and Negi’s thesis [1]. The author would also like to acknowledge the contributions of the undergraduate researchers that supported various aspects of the Zero-G HDD-RW project, including: Zoe Wilf, Chris Andrade, Natasha Evans, Dzuy Nguyen, Ashna Reddy, and Miranda Godinez. The work presented within this thesis is a reflection of the combined efforts from the author, Negi, and the supporting undergraduate researchers.

This thesis will describe the Zero-G HDD-RW experiment design and the development of a supporting Computer Vision (CV) system for attitude verification of the experiment testbeds, while [1] analyzes the performance of the HDD-RWs. The structure is as follows: Chapter 1 describes the motivation for the Zero-G HDD-RW project; Chapter 2 outlines the design of the Zero-G HDD-RW hardware, software, and operations; Chapter 3 describes the design, manufacturing, and on-ground testing of the CV system; and Chapter 4 presents the

CV system results from parabolic flight testing. Finally, Chapter 5 summarizes the findings of the Zero-G HDD-RW experiment design and CV system, and discusses lessons learned to provide guidance to future developers.

1.2 Hard Disk Drives Repurposed as Reaction Wheels

Reaction wheels are widely-used satellite components that enable the control of satellite attitude, or orientation. Reaction wheels consist of a precisely manufactured flywheel mounted to a motor that can provide bidirectional and variable speed control. They can be used to control the rotation rates and orientation of a spacecraft by changing the angular velocity of the flywheel and leveraging the principle of conservation of angular momentum. While they cannot increase or decrease the total magnitude of angular momentum of a satellite, like thrusters or magnetorquers can, a reaction wheel works by changing the distribution of angular momentum within the system. Reaction wheels are often critical to space missions, since they add attitude stabilization and pointing capabilities to a spacecraft.

Commercially available reaction wheels are costly due to requirements for precise manufacturing, flywheel balancing, and a limited number of vendors. In-house built reaction wheels can prove to be failure-prone and time-consuming due to the expertise and machinery needed to manufacture, assemble, and test each unit. Commercial reaction wheels for CubeSats, small satellites which are often built from commercial off-the-shelf (COTS) hardware to reduce development cost and time, range from 2700 USD to 35000 USD per unit [1]. A minimum of three reaction wheels are needed to form a reaction wheel system that provides full three-axis spacecraft control, and a fourth unit is often added for redundancy and fault protection. CubeSat developers, especially those at the university level, must address this cost versus risk tradeoff when developing low-cost missions that require attitude control. Oftentimes, this forces CubeSat developers to assume the risk of in-house reaction wheel design, manufacturing, and testing for each unit, or to forgo reaction wheels entirely.

The Human/Robotics/Vehicle Integration and Performance Laboratory in the UC Davis Center for Spaceflight Research has developed a low-cost, reliable, readily available solution to the CubeSat reaction wheel cost versus risk tradeoff by repurposing HDDs as reaction wheels. HDDs are memory storage devices commonly used in laptops. They contain a pre-

cisely manufactured, well-balanced disk mounted to a Brushless DC (BLDC) motor, thereby providing the mechanical hardware foundation of a reaction wheel. By replacing the electronics board with a custom Electronic Speed Controller (ESC), the motor can be commanded to spin the disk bidirectionally through variable speed profiles, thereby providing the control foundation of a reaction wheel. Three main sizes of HDDs, 1.8", 2.5", and 3.5", were studied due to their appropriate form factors for CubeSats.

Momentum storage (the product of a reaction wheel's maximum rotational velocity and its moment of inertia) is a common way to characterize the performance of a reaction wheel. HDDs repurposed as reaction wheels offer competitive momentum storage capabilities to commercial reaction wheels while only costing 50 USD to 150 USD per unit, as shown below in Figure 1.1.

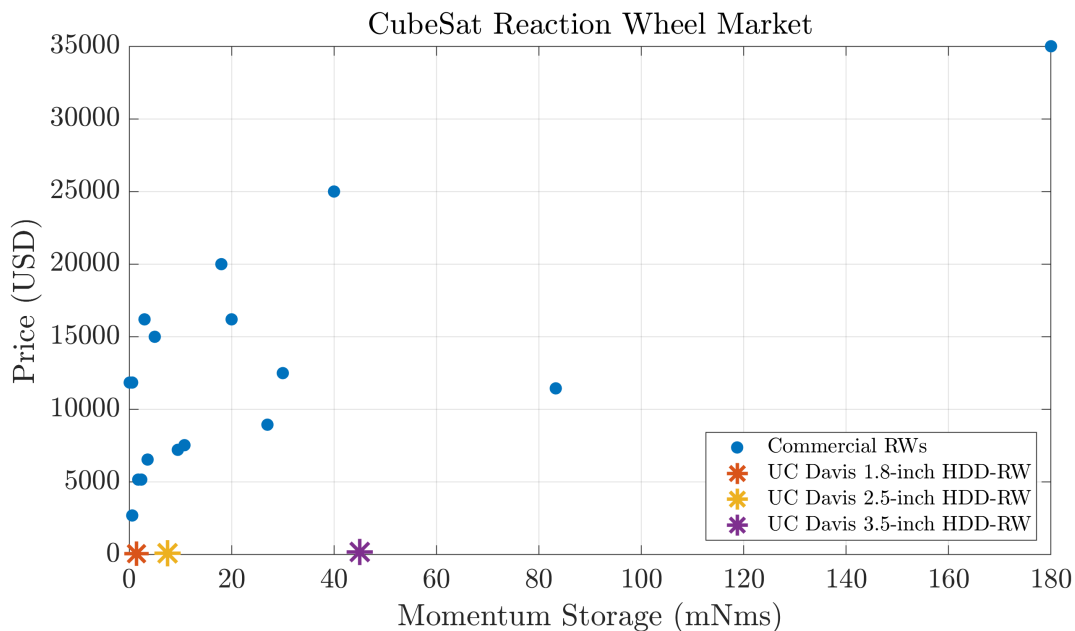


Figure 1.1: Commercial reaction wheel and HDD-RW cost vs. momentum storage comparison

HDDs are also readily available within a few days to a few weeks from most major suppliers, providing time savings compared to the typical 6 week to 6 month lead time of commercial reaction wheels. While Solid State Drives (SSDs) are replacing HDDs in most current laptops due to their superior memory storage capabilities and smaller form factor, HDDs are still readily available, and will continue to be readily available for the foreseeable future. By leveraging the manufacturing maturity of the HDD industry, HDD-RWs can

provide significant cost and time reductions for low-budget or rapid development CubeSat missions while maintaining competitive momentum storage performance with commercial reaction wheel options. In particular, this technology has been developed with the intention of lowering the cost of entry for university students to learn to design, test, and fly CubeSats with attitude control systems that can be afforded on university budgets.

1.3 Technology Readiness Level (TRL) Motivation

The Technology Readiness Level (TRL) scale is a measurement system defined by NASA that evaluates the maturity of spaceflight technology. New technologies begin at TRL 1 and move up the scale as critical development and testing milestones are met. TRL 9, the highest readiness level, is assigned to a technology after it has flown and operated successfully in space. The TRL scale is important in both defining a path to qualifying technology for spaceflight, and in identifying how much risk a technology poses on a spaceflight mission. After reaching TRL 9, a technology is considered to be “flight proven” going forward. Note that a technology does not reach a TRL until it meets all of the supporting criteria. Figure 1.2 below demonstrates the TRL levels defined by NASA. TRLs 1-4 define the technology research phases, and can be performed in laboratory environments. TRLs 5-7 define the technology demonstration phases and require testing in a relevant space environment (ex: Thermal Vacuum/TVAC testing, vibration testing). TRLs 8-9 define the system test, launch, and operations phases and must be performed in space.

The goal of the Zero-G HDD-RW project was to raise the TRL of the HDD-RW technology from TRL 4 (component and/or breadboard validation in laboratory environment) to TRL 6 (system/subsystem model or prototype demonstration in a relevant environment). Raising the TRL of the HDD-RWs increased confidence in the technology, and served as a stepping stone to actual utilization of the technology in spaceflight.

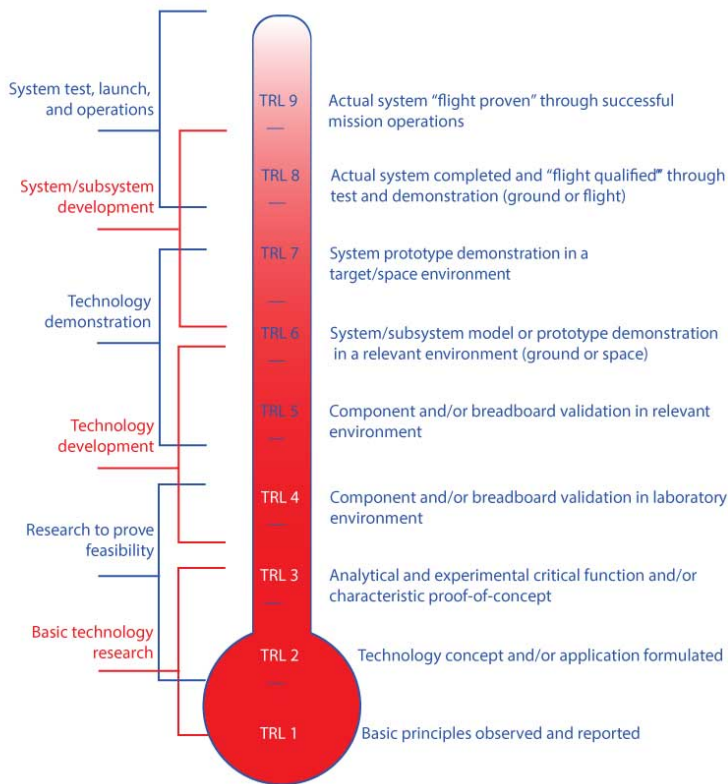


FIGURE G.4-1 Technology Readiness Levels

Figure 1.2: TRL scale [2]

1.4 HDD-RW Testing Process

Spaceflight preparation is expensive, challenging, and time consuming; factors such as high rocket launch costs, limited manifest opportunities, constrained data rates, and multi-year CubeSat development timelines makes methodical pre-flight preparation critical. Raising the TRL of the HDD-RWs through extensive on-ground testing was an important risk reduction step to mature the technologies and to maximize their likelihood of success prior to their first spaceflight demonstration.

Prior to the Zero-G HDD-RW project, several steps were taken to push each of the 1.8", 2.5", and 3.5" HDD-RW technologies up the TRL scale and through the technology research phases (TRLs 1-4). First, the HDDs were electrically modified to spin bidirectionally and with variable speeds through the implementation of new Electronic Speed Controllers (ESCs). Next, individual HDD-RWs were shown to have sufficient control authority to stabilize and point a platform hung by a fishing line in a single axis of "free" rotation.

Finally, prototype CubeSats were then developed with three identical HDD-RWs mounted on each of the prototype CubeSat’s axes to provide 3 axis control. The HDD-RWs were shown to have sufficient control authority to stabilize and point the prototype CubeSats hung by a fishing line in arbitrary axes.

Pushing the HDD-RWs through the technology demonstration phases, TRLs 5-7, requires specialized equipment to simulate the space environment. Rocket launch vibration loads, for example, can be simulated through testing on an electrodynamic vibration testbed, and the vacuum of space can be simulated by running the HDD-RWs in a vacuum or thermal vacuum (TVAC) chamber. The fully unconstrained free-floating environment of microgravity, however, is especially challenging to replicate without going to space. Fishing line tests can provide one rotational degree of freedom (DOF) for testing; however, the testbed is subject to increasing counter torque as the fishing line winds up. To truly simulate the microgravity environment of space, and to observe cross-coupling effects, the HDD-RWs need to be tested in an environment that provides 3 rotational DOF. Two main testing methods were considered for raising the TRL of the HDD-RWs to 6: air bearing platforms, and parabolic flights.

Air bearing testbeds are the most commonly-used platforms for performing attitude control system (ACS) verification testing, and have been in use in the space industry since 1960 [3]. Air bearings provide a thin cushion of air upon which the testbed can move with minimal friction. Two forms of air bearing testbeds exist: planar systems, which provide one rotational and two translational degrees of freedom, and rotational systems, which are fixed in translation but provide 3 rotational degrees of freedom (one axis is unconstrained, two axes are constrained). Spherical air bearings are most commonly used in rotational systems, and can provide up to ± 90 degrees of rotation in the constrained axes.

Parabolic flights utilize an aircraft flying in a trajectory that simulates the “microgravity” or “zero-gravity (0G)” environment of space through a free falling maneuver. In this free-fall maneuver, the inertial force from the aircraft’s downward acceleration and the normal force from the aircraft to researchers and test articles inside the cabin due to gravity cancel out to near-zero. Testing in parabolic flights is the closest simulation of the fully unconstrained free-floating environment of microgravity that can be achieved without utilizing a rocket

launch or entering orbit.

While both air bearing testbeds and parabolic flights are common methods of testing space hardware, parabolic flights were ultimately chosen as the test platform for the HDD-RWs based on their ability to provide an environment that allows for fully unconstrained 3DOF rotation. Parabolic flights may be superior to air bearing testbeds in their ability to allow for unconstrained motion; however, they do have their limitations. The microgravity quality provided in each flight is dependent on flight conditions in the airspace and on manual control by the aircraft pilots. Also, while the HDD-RW testbeds were not constrained in translation or rotation in parabolic flights, they were constrained by time - parabolic maneuvers provide a maximum of approximately 15-20 seconds of continuous microgravity time per parabola.

1.5 NASA Tech Flights Grant

The NASA Tech Flights Grant is a funding source that enables research in commercial flights such as high altitude balloons, suborbital vehicles, and parabolic aircraft [4]. The UC Davis HRVIP lab submitted a technical proposal to NASA Tech Flights in May 2020 to raise the TRL of the HDD-RWs from 4 to 6 through testing in parabolic flights. The proposal was accepted in October 2020 [5], and awarded \$450,000 to develop the HDD-RWs and supporting equipment to perform tests in four parabolic flights provided by the Zero-G Corporation onboard the G-Force One B727 aircraft. Due to the success of the first four flights, the project was awarded an additional \$174,000 in August 2022 to fund two additional parabolic flights with Zero-G. This thesis will focus on the Zero-G HDD-RW parabolic flight experiment design, hardware design, and testbed attitude verification over each of the six Zero-G flights.

Chapter 2

Experiment Methodology

2.1 Introduction

The design of the Zero-G HDD-RW experiment was highly dependent on understanding the parabolic flight environment and the G Force One aircraft layout. While the HDD-RWs will eventually be used for CubeSat attitude control maneuvers in space, the parabolic flight experiments were designed for human operation in a highly dynamic environment. Multiple unique requirements and constraints existed for these experiments that would not normally be factors for a CubeSat mission in space.

First and foremost, the experiment needed to be designed for human operation and human safety. Parabolic flights induce a dynamic environment, with quick transitions between microgravity (0g) and hypergravity (up to 1.8g). These rapidly evolving gravity levels posed three main challenges to experiment operation: short experiment duration, possible motion sickness in researchers, and safe containment of free-floating hardware. The designs of all the hardware and experiment operations took into account the environment variability and safety of the experiment operators.

Another notable difference between preparation for the parabolic flight experiments and an orbital mission is that the testbeds were considered prototypes, and did not need to be space qualified for these experiments. For example, the prototype CubeSat testbeds and all supporting hardware used in the parabolic flights did not need to be vibration tested, since these units were not launched to space. Therefore, testbed designs leveraged prototyping methods such as 3D printing and laser cutting for rapid development and cost effectiveness.

2.2 Background

2.2.1 Aircraft Environment

The G Force One Aircraft, shown in Figure 2.1, is a specially modified Boeing 727-200F aircraft that accommodates multiple concurrent reduced gravity experiments. The forward portion of the cabin is an open area, approximately 60 ft length x 10 ft diameter, where research experiments are stationed in designated locations. The aft portion of the cabin contains seats for researchers during takeoff and landing. In general, experiment teams are each provided 10 ft of space along the cabin's open area, while certain smaller experiments can be performed in the seating area. The walls and floors of the aircraft are padded to prevent researcher injury while free-floating.



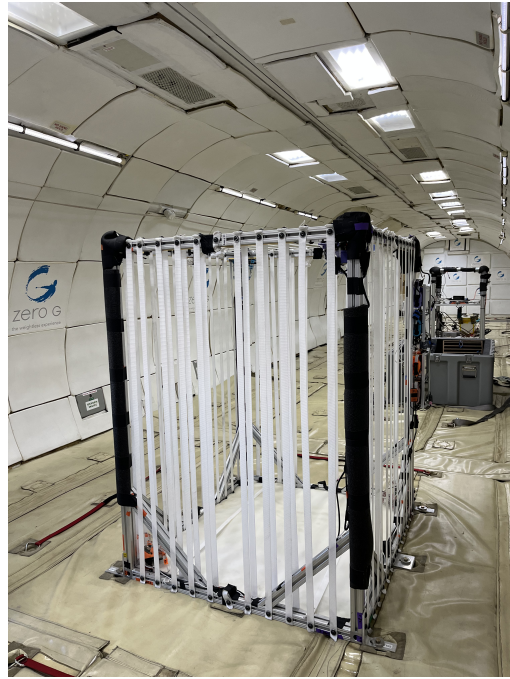
Figure 2.1: G Force One Aircraft [6]

Experiment hardware can be loaded with a forklift through the aircraft's cargo door (shown below in Figure 2.2), which provides 84" height x 134" width of loading access, and can be bolted onto the aircraft's floor mounting pattern if needed. An onboard storage container is shared between all experimenters for smaller hardware and loose tools. The onboard storage container cannot be accessed during parabolic maneuvers - it must be accessed on ground or during straight and level flight (i.e. after takeoff but before the first set of parabolas, in any break in between parabolas sets, or after the final parabola set but prior to landing).

Power can be provided to experiments from the aircraft as necessary, although it was not used for any systems on the HDD-RW experiments. The cabin has incandescent lighting overhead and LED lights both overhead and on the aircraft walls. The lighting environment has been tuned to a color temperature of 5600 Kelvin to simulate “sunlight-quality illumination.”



(a) Loading Zero-G HDD-RW experiment hardware through G Force One’s cargo door



(b) Forward facing view of aircraft cabin, with Zero-G HDD-RW chamber in foreground

Figure 2.2: Aircraft cabin environment

2.2.2 Flight Profile

Parabolic flights utilize an aircraft flying in a trajectory that simulates the microgravity environment of space through a free falling maneuver. In this maneuver, researchers in the cabin “fall” at the same acceleration rate as the aircraft - when that rate is approximately equal to Earth’s gravitational acceleration of 9.81 m/s^2 , the inertial force from the aircraft’s downward acceleration and the normal force from the aircraft to the researchers due to gravity cancel out to near-zero [7]. Thus, the researchers and test articles in the aircraft cabin experience a simulated microgravity environment similar to that experienced by satellites and astronauts in orbit.

While multiple flight providers have achieved the microgravity environment, this section will focus on the flight mechanics of the Zero-G Corporation’s G Force One aircraft. Each parabola begins with a 1.8g pull up and ends with a 1.8g pull out, as shown below in Figure 2.3.

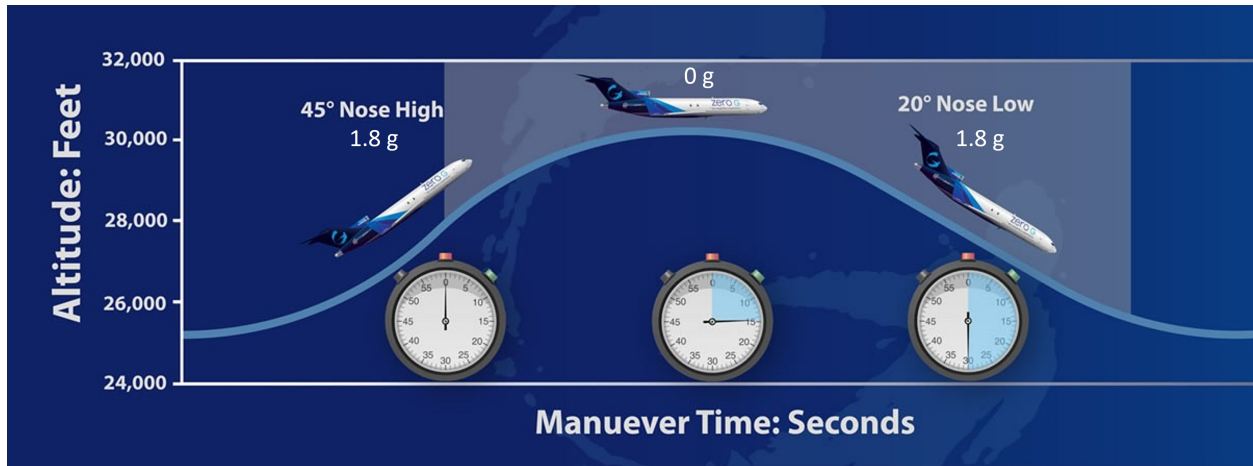


Figure 2.3: G Force One aircraft flight profile (image sourced from [6], and annotated by the author)

By varying the parabola profile, the G Force One aircraft is able to simulate multiple reduced gravity levels important for spaceflight testing, including martian gravity ($\frac{1}{3}g$), lunar gravity ($\frac{1}{6}g$), and microgravity ($0g$). For this experiment, microgravity was the target environment. On each of the six flights taken, the aircraft performed a total of 30 parabolas in the following sequence: 2 martian parabolas, 3 lunar parabolas, and 25 microgravity parabolas, as shown in Table 2.1. Although the martian and lunar parabolas were not needed for this experiment, they were helpful for researcher acclimation to the low gravity environment, and served as a training ground for experiment operations. Parabolas were split into sets of 5, with a few minutes of break in between each set while the aircraft turned around to stay within its designated airspace.

Table 2.1: Zero-G Flight Profile for HDD-RW Experiment

Parabola Set	Parabola Type	Number of Parabolas
1	Martian ($\frac{1}{3}$ g)	2
	Lunar ($\frac{1}{6}$ g)	3
Straight and Level - Aircraft is turning around in airspace (appx 5 min)		
2	0g	5
Straight and Level - Aircraft is turning around in airspace (appx 5 min)		
3	0g	5
Straight and Level - Aircraft is turning around in airspace (appx 5 min)		
4	0g	5
Straight and Level - Aircraft is turning around in airspace (appx 5 min)		
5	0g	5
Straight and Level - Aircraft is turning around in airspace (appx 5 min)		
6	0g	5
Straight and Level - Experiments are complete		

Verbal callouts are utilized to indicate transition periods in the flight profile. Due to the limited microgravity duration, recognizing and responding to callouts is an important part of experiment operations. Table 2.2 below summarizes the Zero-G verbal callouts and their meanings.

Table 2.2: Zero-G Flight Callouts

Callout	G Level	Callout Meaning
On the pull	1.8g	Aircraft is pulling up into the parabola.
Pushing over	1.8g \rightarrow 0g	Aircraft is nearing the top of the parabola, and transitioning from hypergravity to microgravity.
Release	0g	Microgravity has officially begun.
Feet down, coming out	1.8g	Aircraft is nearing the end of the parabola, and is transitioning from microgravity to hypergravity.
Straight and level	1 g	Aircraft is turning around in between parabola sets.

2.3 Experiment Design

2.3.1 Goal Definition

The Zero-G HDD-RW experiment was a technology demonstration aimed at raising the TRL of HDD-RWs from TRL 4 to TRL 6. Testing the reaction wheels in a microgravity environment with fully unconstrained 3 rotational DOF allowed for characterization of their performance as a 3 axis CubeSat attitude control system. The goals of this experiment were:

1. Demonstrate each form factor of the HDD-RW technology performing 3-axis attitude control in a microgravity environment.
2. Characterize the input command to output response of each HDD-RW.

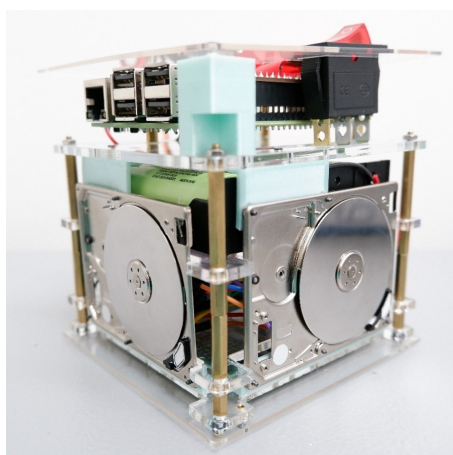
2.3.2 Hardware Overview

CubeSat Testbeds

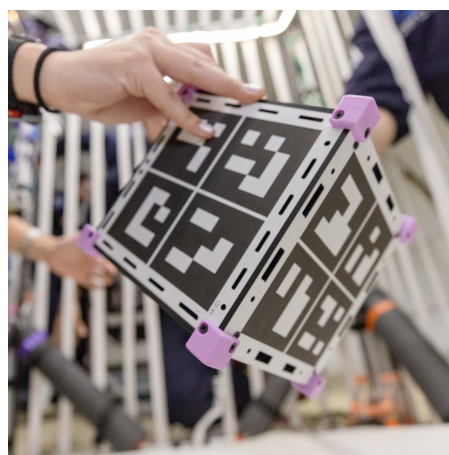
The CubeSat testbeds were the supporting platforms for testing the HDD-RWs. Each CubeSat testbed contained three of the same size and model HDD-RWs, with one mounted on each of the testbed's X, Y, and Z axes. A total of five CubeSat testbeds were developed - two containing 1.8" HDD-RWs, one containing 2.5" HDD-RWs, and two containing 3.5" HDD-RWs. The CubeSat testbed structures were made of laser-cut acrylic and 3D prints. Rounded

3D printed bumper guards were attached to all corners of the CubeSat testbeds to protect researchers from sharp corners. Bumper guards were color coded for easy identification of each CubeSat testbed. An example of the internal electronics stack of a CubeSat testbed is shown below in Figure 2.4a; for detailed schematics of the CubeSat testbed electrical designs, see Appendix A.1.

Although onboard attitude estimates were determined from Inertial Measurement Units (IMUs) built into each CubeSat testbed, four of the five testbeds also had ArUco markers engraved on the exterior, as shown below in Figure 2.4b, to allow for testbed pose (position and attitude) estimation through computer vision. The computer vision system is described in detail in Chapter 3.



(a) Internal electronics stack of CubeSat testbed A1 with 1.8" HDD-RWs



(b) CubeSat testbed C1 with exterior ArUco markers

Figure 2.4: CubeSat testbed hardware

Each CubeSat testbed consisted of the following main components:

- 3 HDD-RWs (one on each of the X, Y, and Z axes) of a specific size
- Raspberry Pi (RPi) 3B+ computer for running flight software and interfacing with sensors
- IMU with a gyroscope for measuring three-axis rotational velocity and an accelerometer for measuring three-axis linear acceleration rates
- Power sensor for measuring HDD-RW input voltage and total current draw

- Independently-powered Real Time Clock (RTC) for keeping correct time after power cycling system
- Control panel consisting of screen, buttons, and LEDs to allow experimenter interfacing with the CubeSat during flight
- Li-ion cells for power

Table 2.3: CubeSat Testbed Summary

CubeSat Testbed ID	HDD-RWs Size (x3)	Outer Dimensions	Face Design	Identifying Color
A1	1.8"	10cm x 10cm x 10cm	ArUco Markers	Light Blue
A2	1.8"	10cm x 10cm x 10cm	ArUco Markers	Light Blue
B	2.5"	15cm x 15cm x 15cm	ArUco Markers	Royal Blue
C1	3.5"	15cm x 15cm x 15cm	ArUco Markers	Pink
C2	3.5"	15cm x 15cm x 15cm	Clear Acrylic	Green

Chamber

The chamber was a parallelepiped structure constructed of Aluminum 80/20 beams and fixed rigidly to the aircraft floor, as shown below in Figure 2.5a. It had the dual purpose of 1) containing the CubeSat testbeds during free-floating trials to protect researchers and 2) providing mounting points for the computer vision system cameras and screens. Fabric straps were fastened to the sides and top of the chamber with sufficient spacing to prevent the CubeSats from escaping while allowing for researchers to reach in and manipulate the CubeSat testbeds. For detailed working drawings of the chamber, see Appendix A.2.

Note that only one CubeSat testbed was tested inside the chamber at a time, as shown below in Figure 2.5b. After the first flight campaign, it was determined that certain researchers had sufficient experience to perform the same experiment in parallel outside of the chamber. Thus, in flight campaigns 2 and 3, one CubeSat testbed was tested inside the chamber (referred to as the “Chamber Experiment”) while 1-2 other CubeSats testbeds were tested in an “External Experiment” located in an open area next to the chamber.

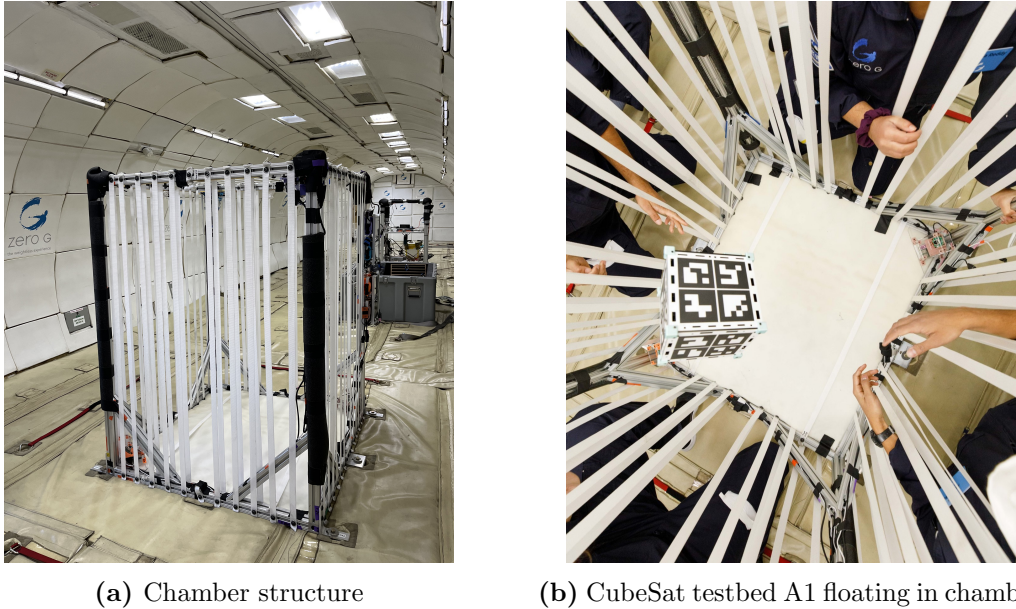
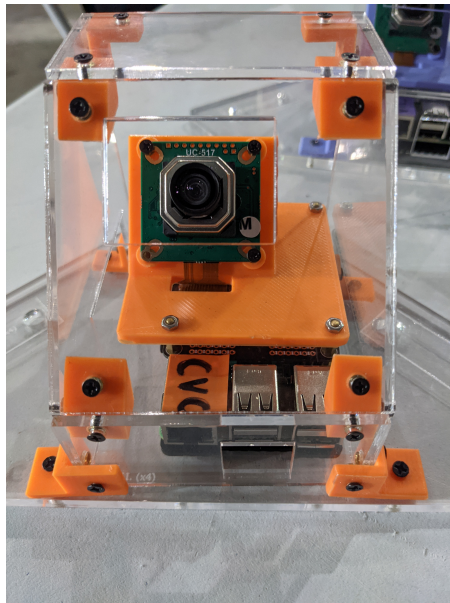


Figure 2.5: Chamber installed in Zero-G aircraft

Computer Vision System

A computer vision system was developed for external attitude determination of the free-floating CubeSat testbeds. External attitude determination allowed for verification of the CubeSat testbed’s onboard attitude determination method. A protective acrylic housing was designed and fabricated for each camera unit to protect the cameras and sensors from collision with the free-floating CubeSat testbeds, as shown in Figure 2.6a. Each camera was connected to a touch screen that displayed live video feed of the experiment, as shown below in Figure 2.6b. The touch screens also allowed experiment operators to start and stop the video recording as necessary. Videos were recorded for each experiment trial, and post-processed to track the pose of the CubeSat testbeds. These data were then combined with the CubeSat’s IMU data in an Extended Kalman Filter (EKF) for improved pose estimation. For additional information on the design, fabrication, and structural verification

of the computer vision system, see Chapter 3. For additional information on the CV system and EKF results, see Chapter 4.



(a) Camera C protective acrylic housing



(b) CV system touch screens

Figure 2.6: Computer Vision system hardware

Each camera unit consisted of the following main components:

- Arducam 12MP camera for recording video of the experiments
- Raspberry Pi (RPI) 3B+ computer for running flight software, interfacing with camera, and reading data from sensors
- Inertial Measurement Unit (IMU) with a gyroscope for measuring three-axis rotational velocity and an accelerometer for measuring three-axis linear acceleration rates of the aircraft
- Independently-powered Real Time Clock (RTC) for keeping correct time after power cycling system
- Touch screen for turning the corresponding camera on or off
- Battery bank to power the corresponding camera, sensors, and screen

Table 2.4: CV System Camera Summary

Camera ID	Position (see Figure 2.7)	Purpose	Identifying Color
A	Top of chamber, angled inward	Chamber Experiment	Purple
B	Top of chamber, angled inward	Chamber Experiment	Blue
C	Bottom of chamber, angled inward	Chamber Experiment	Orange
D	Bottom of chamber, angled inward	Chamber Experiment	Pink
E	Top of chamber, angled outward	External Experiment	Green

Experiment Layout

Figure 2.7 below depicts the overall layout of the experiment hardware in the aircraft. The chamber was fixed to the aircraft floor, and all computer vision system hardware was rigidly attached to the frame of the chamber. During the microgravity portion of each parabola, a single CubeSat testbed was deployed inside the chamber for the “Chamber Experiment”, while 1-2 CubeSat testbeds were simultaneously deployed outside of the chamber for the “External Experiment”. Cameras A-D tracked the Chamber Experiment CubeSat testbed, while Camera E tracked the External Experiment CubeSat testbed(s).

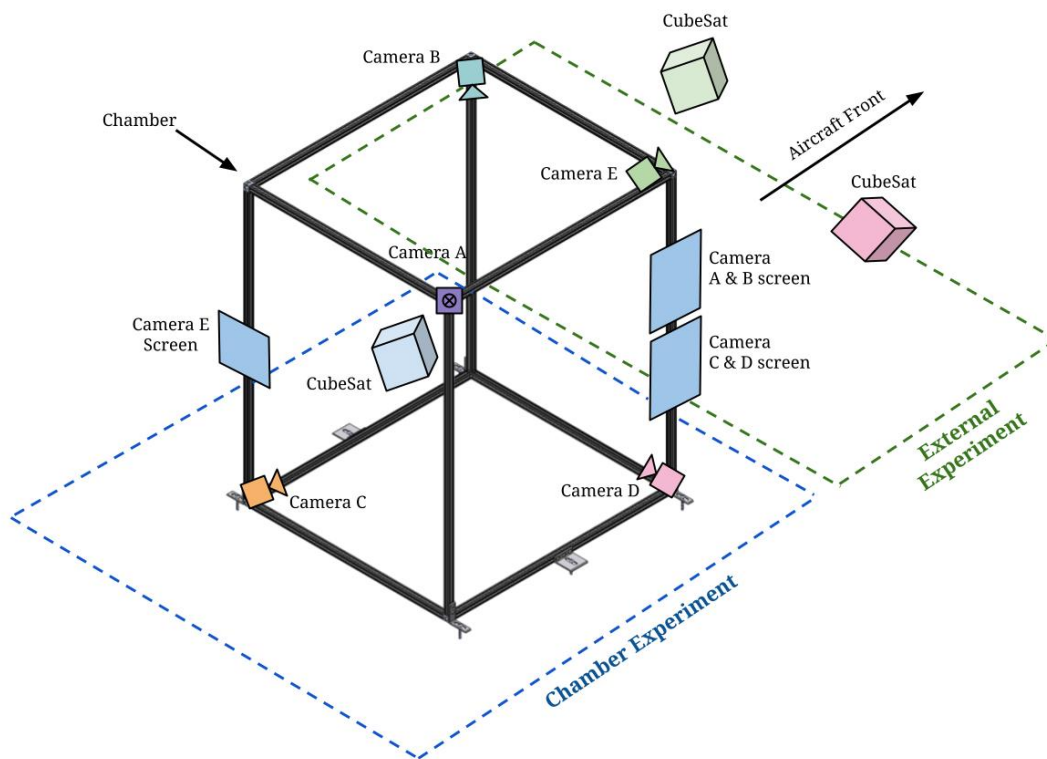


Figure 2.7: Zero-G HDD-RW Experiment Layout

2.3.3 Test Case Definition

Three major HDD-RW attitude control cases were defined for this project: linear ramp, stabilization, and pointing. Flight Campaign 1 (FC1) focused on the linear ramp tests, Flight Campaign 2 (FC2) focused on the stabilization tests, and Flight Campaign 3 (FC3) focused on the pointing tests, as shown in Table 2.5. Two parabolic flights were performed in each flight campaign. Note that this section will present the objectives and operations for

each test case; however, the results of the test cases are analyzed in Abhay Negi’s thesis [1].

Table 2.5: Zero-G HDD-RW Test Case Definition for all Flight Campaigns

Flight Campaign	Flight Number	Chamber Experiment	External Experiment	CubeSat Testbeds Used
1	1	Linear Ramp	N/A	B
	2	Linear Ramp	N/A	B
2	3	3-Axis Stabilization	3-Axis Stabilization	C1, C2
	4	3-Axis Stabilization	3-Axis Stabilization	C1, C2
3	5	3-Axis Pointing	3-Axis Pointing	B, C1, C2
	6	3-Axis Pointing	3-Axis Pointing	B, C1, C2

FC1: Linear Ramp Test

In the linear ramp case, the CubeSat testbed was deployed by hand with minimal initial rotation and the HDD-RWs were ramped from zero motor speed to their max motor speed at a linear rate. This allowed for characterization of the HDD-RW input/output response, as well as estimation of the torque that they provided on the CubeSat testbeds. Starting with the linear ramp case generated valuable data for characterization of the HDD-RW motors, and served as a proving ground for the Zero-G HDD-RW hardware and software designs. The linear ramp case was the simplest case, both in terms of software and operations, which allowed for experiment operators to practice operations in the dynamic environment of parabolic flights, and to revise experiment hardware and operations prior to the more complicated stabilization and pointing tests in the following flight campaigns. The main objectives of this test were as follows:

- LR-1. Characterize the relationship between the HDD-RW input command and the resulting CubeSat angular velocity.

LR-2. Analyze the repeatability of the HDD-RWs when performing the same linear ramp sequence multiple times.

Verification of the ramp objectives occurs through the two independent techniques for measuring testbed attitude: gyroscope data numerical integration and CV data attitude estimation. Objective LR-1 is satisfied if a consistent relationship is found between the HDD-RW input command and the measured CubeSat angular velocity. Objective LR-2 is satisfied if the HDD-RW ramp performance is found to be consistent across in-flight trials and consistent with on-ground testing. Since this was performed on FC1, only one CubeSat was tested at a time, and all tests were performed within the chamber. Figure 2.8 below shows the researcher and hardware layout for the ramp tests performed in FC1; labels R1-R5 indicate the researchers' designated positions. Figure 2.9 provides a view of the chamber experiment operations during flight.

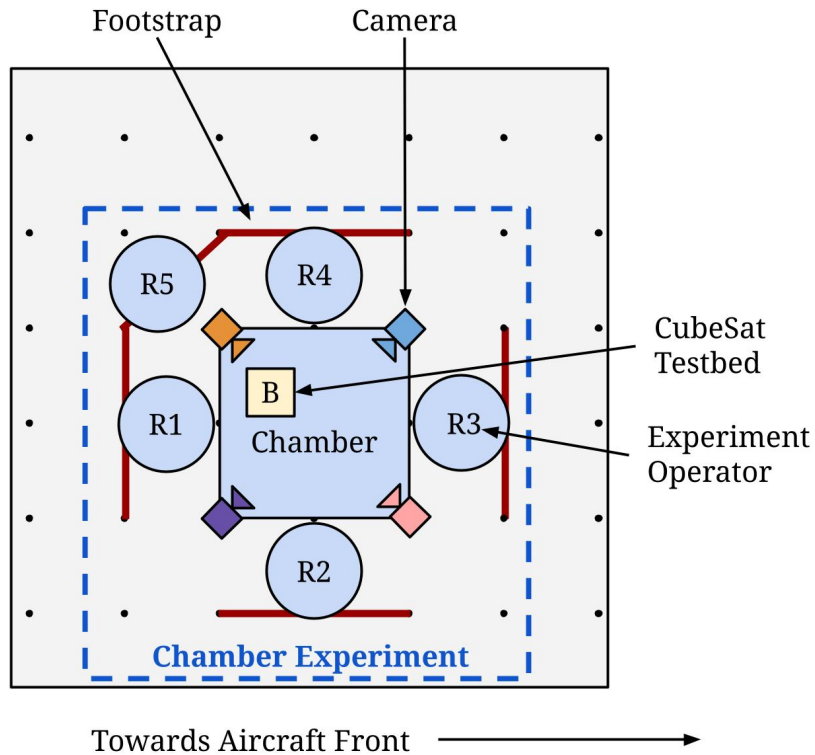


Figure 2.8: Flight Campaign 1 Hardware and Researcher Layout (Top View)



Figure 2.9: Zero-G HDD-RW Experimenters Performing Linear Ramp Experiment in FC1

FC2: Stabilization Test

Stabilization is a crucial CubeSat ACS capability; for example, a CubeSat may need to perform a stabilization maneuver to detumble after deployment, or to null disturbances introduced by solar pressure, atmospheric drag, gravity gradient, magnetic fields, or thrust vector misalignment. In the stabilization test case, the CubeSat testbed was deployed by hand with a random initial rotational speed and axis, and used the HDD-RWs to absorb the imparted momentum to reduce its body rotational rates to near zero, relative to an inertial reference frame. The stabilization controller design was informed by data from the linear ramp tests, and the human-guided experiment operations were informed from the operational experience of performing the linear ramp tests. The main objectives of the stabilization test were as follows:

- S-1. Analyze the ability of the HDD-RW and controller system to null out disturbances applied along arbitrary axes.
- S-2. Analyze the ability of the HDD and controller system to hold a fixed position in an inertial reference frame once disturbances have been nulled out.

Verification of the stabilization objectives occurs through gyroscope data analysis. Ob-

jective S-2 is satisfied for a trial if gyroscope readings can be maintained below a specified angular rate threshold for a sustained amount of time. Objective S-1 is satisfied for the stabilization test set if Objective S-2 is met for an initial disturbance torque that is hand-applied in any arbitrary direction. Note that the stabilization tests are analyzed in Abhay Negi's thesis [1].

After observing that parabolic flight floating times were shorter than expected in FC1, the external experiment was added in FC2. The external experiment removed the volume constraints of the chamber, which allowed for slightly longer free-floating time (5-7 seconds in external experiment vs. 3-5 seconds in chamber experiment). This was especially important for the stabilization tests, as the CubeSat had to respond to an input disturbance and null its rotation rates within a few seconds. Longer float times gave the controller more time to respond, and provided insight on the controller's stability. For FC2, one CubeSat was operated in the external experiment by experimenters with operational experience from FC1, while one CubeSat was operated concurrently in the chamber experiment by new team members. Figure 2.10 below shows the researcher and hardware layout for the stabilization tests performed in FC2; labels R1-R5 indicate the researchers' designated positions. Figure 2.11 provides a view of the experiment layout and operations during flight, with the external experiment in the foreground and the chamber experiment in the background.

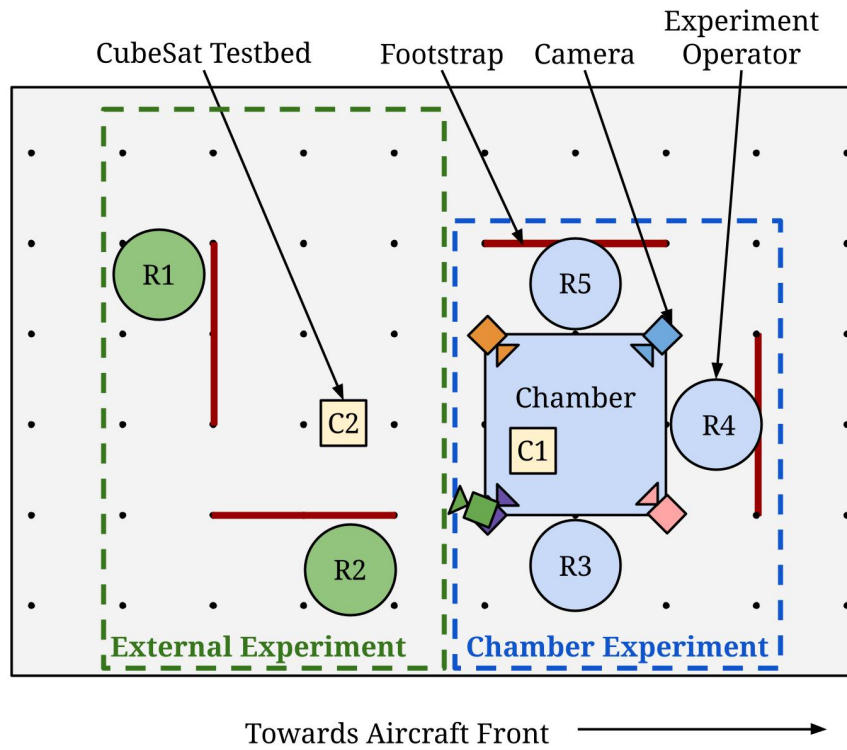


Figure 2.10: Flight Campaign 2 Hardware and Researcher Layout (Top View)

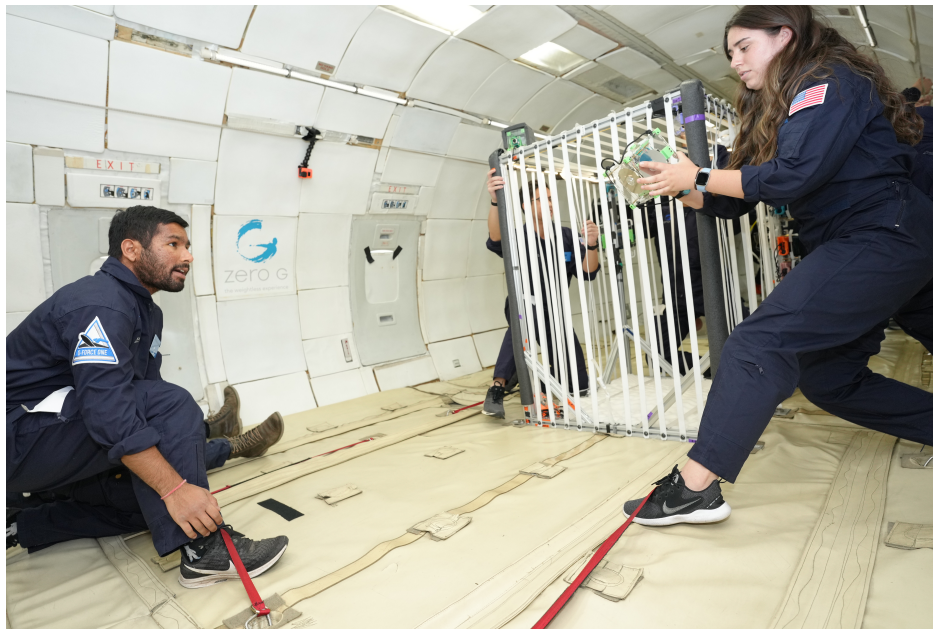


Figure 2.11: Zero-G HDD-RW Experimenters Performing Stabilization Experiment in FC2

FC3: Pointing Test

Pointing is another crucial CubeSat ACS capability; for example, a CubeSat may need to point an antenna towards a ground station for communications or a sensor at a specified target for remote sensing. In the pointing case, the CubeSat testbed was deployed by hand with minimal initial rotation during the microgravity portion of each parabola, and used the HDD-RWs to perform a rotation about a pre-specified axis. Varying the target pointing angle and pointing axis was important to ensure that the HDD-RWs could point the testbed to any arbitrary orientation. The controller design and experiment operations were both informed by the linear ramp and stabilization tests. The main objectives of this test were as follows:

- P-1. Analyze the ability of the HDD-RWs and controller system to rotate to pre-specified orientations.
- P-2. Analyze the ability of the HDD and controller system to hold a fixed position in an inertial reference frame once the pointing maneuver has been performed.

Verification of the pointing objectives occurs through the two independent techniques for measuring testbed attitude: gyroscope data numerical integration and CV data attitude estimation. Objective P-1 is satisfied if camera-attitude and integrated-gyroscope data indicates that the CubeSat performed the desired rotation within a specified angular threshold. Objective P-2 is satisfied if the target can be held for a sustained amount of time. Note that the pointing tests are analyzed in Abhay Negi's thesis [1].

After analyzing data from FC2, it was determined that running the Chamber Experiment and External Experiment in parallel was very beneficial due to the longer observed CubeSat testbed floating times in the External Experiment. In addition, the operations were updated such that two CubeSats were tested concurrently in the external experiment, with one experienced experimenter operating each external CubeSat testbed. Thus, in FC3, three CubeSats were tested concurrently - one in the Chamber Experiment, and two in the External Experiment, as shown in Figure 2.12 below. Figure 2.13 provides a view of the experiment layout and operations during flight, with the external experiment in the foreground and the chamber experiment in the background.

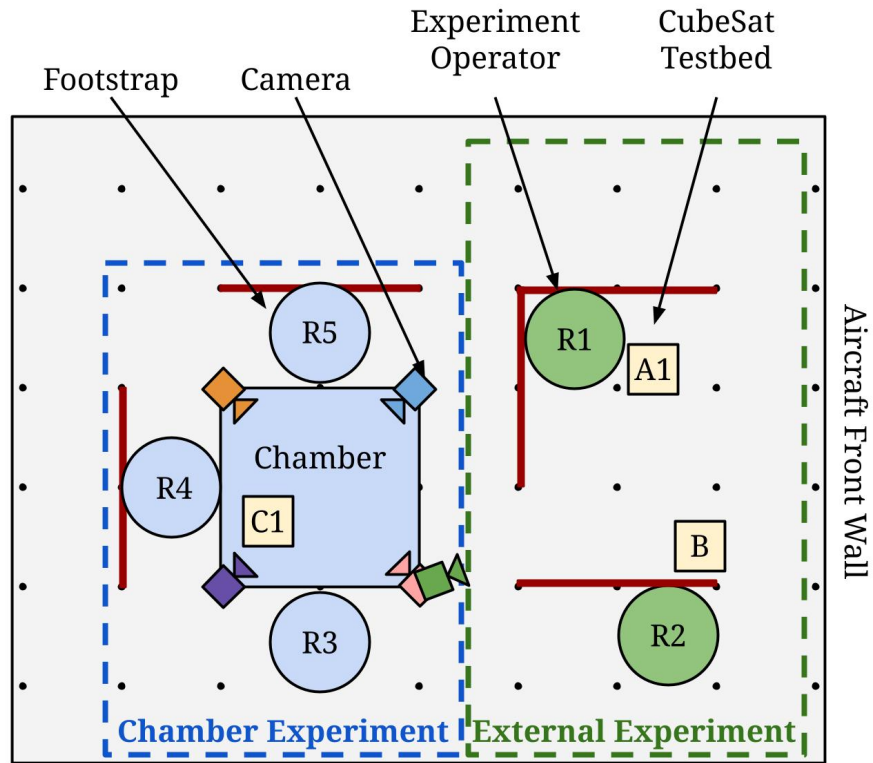


Figure 2.12: Flight Campaign 3 Hardware and Researcher Layout (Top View)



Figure 2.13: Zero-G HDD-RW Experimenters Performing Pointing Experiment in FC3

Chapter 3

Computer Vision System Design

3.1 Introduction

The computer vision (CV) system was designed for external pose (attitude and position) determination of the CubeSat testbeds. The CV system served four main functions:

1. Validation of the attitude estimates that were input to the CubeSat testbed stabilization and pointing controllers
2. Redundant, external attitude determination method in case of CubeSat testbed internal gyroscope data dropout, error, or file corruption
3. Position and attitude state measurement source for post-processing use in an Extended Kalman Filter (EKF)
4. Video documentation and visualization of the experiment trials

This chapter is organized as follows: Section 3.2 describes the fiducial marker selection process and marker system design; Section 3.3 describes the camera selection, placement, and calibration; and Section 3.4 describes the ground testing process and results.

3.2 Fiducial Marker System Design

3.2.1 Introduction

Fiducial markers are objects with distinct visual characteristics that can be identified as landmarks when placed in a camera's field of view (FOV). Many types of fiducial markers

exist, each with a specific encoding that allows them to be distinguished from other objects or markers in the camera’s FOV. Certain fiducial markers also allow for marker pose evaluation relative to the camera.

Fiducial markers were used in the Zero-G HDD-RW project to obtain the pose of the CubeSat testbeds relative to each camera in the CV system. Video of a CubeSat testbed’s motion was captured throughout each experiment trial and post-processed after the Zero-G flights to determine the trajectory and orientation of the CubeSat testbed over the trials. The processed CV data was combined with the CubeSat testbed’s onboard gyroscope measurements in an Extended Kalman Filter (EKF) to provide a best estimate of the CubeSat testbed’s pose over each experiment (Chapter 4). This section details the fiducial marker selection and implementation for the Zero-G HDD-RW project.

3.2.2 Fiducial Marker Selection

Fiducial markers are widely used in fields such as manufacturing, robotics, Unmanned Aircraft Systems (UAS), and Augmented Reality (AR) as reference points and/or pose measurement techniques. This review will focus on open source planar markers used for pose estimation, as they are most relevant to the Zero-G HDD-RW project.

Fiducial markers most commonly come in circular and square shapes, with unique internal patterns that allow for marker identification. They are often black and white, like QR codes, although some greyscale and multi-colored options exist. From literature review of [8] and [9], ARTag, AprilTag, and ArUco markers were identified as the three most widely used open source fiducial markers with state-of-the-art performance in accuracy and precision. Each of these are planar, square, black-and-white fiducial markers with significant heritage in robotic and UAS navigation systems. While each of these marker types can look similar, as shown in Figure 3.1, the detection software, accuracy and precision, and community support vary.

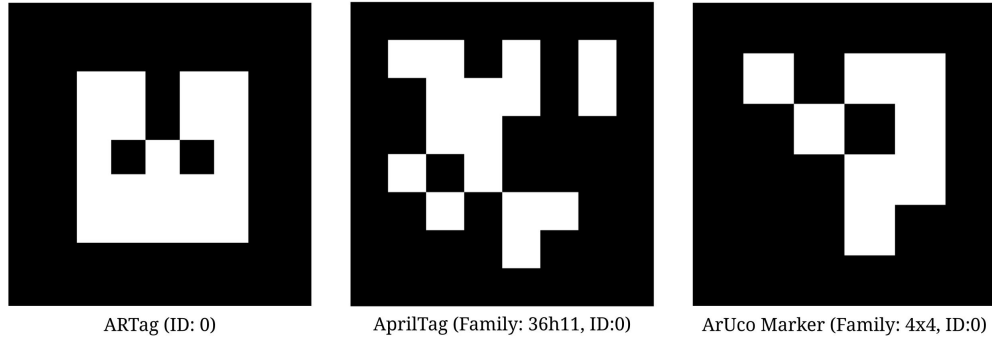


Figure 3.1: Example Fiducial Markers: ARTag [10], AprilTag [11], and ArUco [12]

The most important selection criteria for identifying an appropriate fiducial marker type for the Zero-G HDD-RW system are listed below:

- Attitude accuracy and precision across various angles within the expected operating range of 70 in (178 cm), defined by the chamber’s diagonal distance.
- Position accuracy and precision within the expected operating range of 70 in (178 cm), defined by the chamber’s diagonal distance.
- Package support for combining pose estimates of multiple markers along a 3D shape
- Compatibility with low-cost cameras
- Documentation and community support

ARTag was shown to have low marker detection rates for single marker systems with large outliers and standard deviation in marker groups in [8]. AprilTag outperformed ArUco in attitude estimation accuracy results in [8] and [9], but was shown to be more sensitive to translational and rotational motion blur in [8].

After investigating the implementation of both AprilTag and ArUco, ArUco was chosen for the Zero-G HDD-RW project due to its extensive documentation and community support, ease of implementation, robustness against motion blur, and competitive position and attitude accuracy results. Ground tests performed in the HRVIP lab to characterize the accuracy and precision of the Zero-G HDD-RW ArUco system are described in Section 3.4.

3.2.3 ArUco Dictionary Selection

Each ArUco marker is made of two parts: a black outer border and an internal matrix which defines the marker pattern. The internal matrix is made up of bits, which specify whether a portion of the matrix is black or white. The number of bits in a marker's internal matrix determines the marker size; for example, a marker in the 4x4 ArUco dictionary contains 16 bits. Figure 3.2 below provides an example of the difference between markers in the 4x4, 5x5, 6x6, and 7x7 ArUco dictionaries. Note how for the same marker side length, the internal bit side length decreases with increasing marker size.

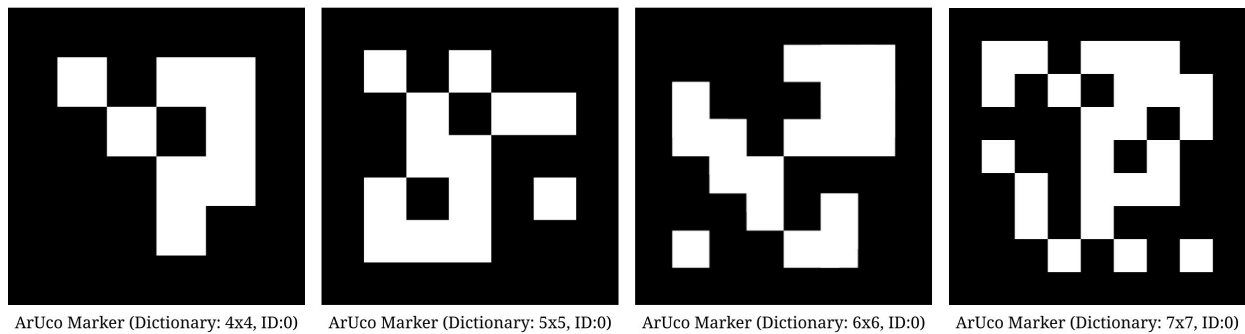


Figure 3.2: ArUco marker size comparison

There is a trade-off between marker size, inter-marker distance, and marker detection time. Inter-marker distance describes how similar a marker's pattern is to other markers in the same dictionary. High inter-marker distance means that markers are unique and not likely to be misidentified as a different marker; low inter-marker distance means that marker patterns can be similar to each other and therefore are more likely to be misidentified. Although a large marker size allows for a high quantity of unique patterns to be developed, it leads to a small inter-marker distance and longer detection time; conversely, a smaller marker size allows for higher inter-marker distance and lower detection times. ArUco offers predefined dictionaries with varying numbers of markers and marker sizes so users may select the best option for their project. In general, it is best practice to determine the dictionary that fits the minimum number of markers and minimum marker size necessary for a given project, to both maximize inter-marker distance and minimize detection time.

For the Zero-G HDD-RW project, the same ArUco board definition was used on each CubeSat testbed. Five faces used four markers each, and one face used three markers, for a

combined total of 23 unique markers in the ArUco board definition of each CubeSat testbed. The ArUco dictionary with the smallest marker size, 4x4, and lowest amount of available markers, 50, was chosen for the project.

3.2.4 ArUco Board

ArUco provides the capability to define a 3D group of markers, called an ArUco Board, with known positions and orientations relative to each other. If any one marker in the board is detected, the pose of the entire board can be estimated. This approach was utilized for the Zero-G HDD CubeSat testbeds; multiple markers were placed on each face of the testbed, and the overall pose of the testbed could be estimated from detection of any single marker or any combination of markers.

Multiple markers were used per CubeSat testbed face to allow for testbed pose estimation in the case of partial occlusion. Experiment operators needed to release and catch the CubeSat testbed by hand, which would cause partial occlusion of the CubeSat testbed faces at the beginning and end of each trial. Designing the testbed to have multiple markers per face made the CV system more robust to these occlusion cases - if one marker was occluded, any combination of other visible, detectable markers could be used to estimate the testbed pose.

An example of ArUco board detection on a CubeSat testbed is demonstrated below in Figure 3.3. Marker IDs are labeled for each detected ArUco marker, and the testbed axes are drawn from the estimated ArUco board pose.

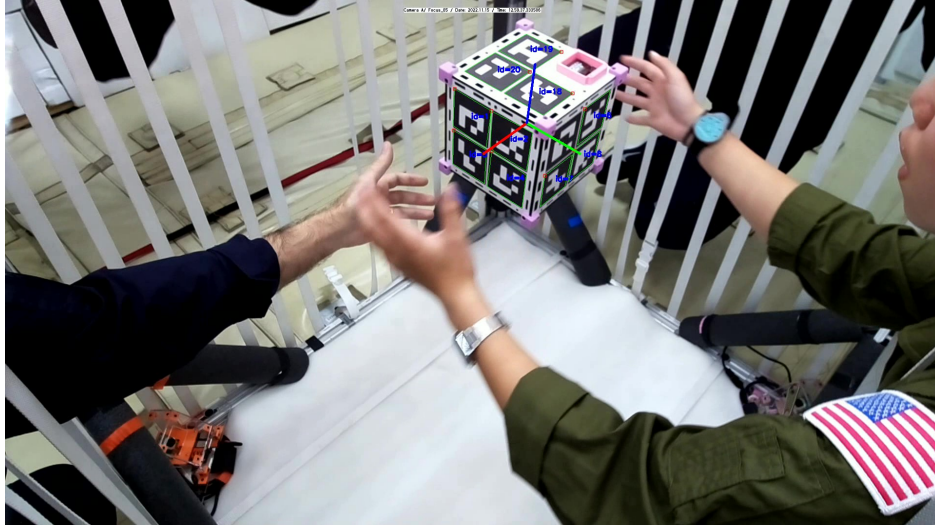


Figure 3.3: CubeSat testbed with ArUco board detected and estimated testbed axes drawn

3.2.5 Laser Engraving Markers

Accurate, repeatable manufacturing of the ArUco markers was important for ensuring that the physical setup of the ArUco board and the software definition of the ArUco board closely aligned. To address this, the markers were laser engraved onto the acrylic faces of the CubeSat testbeds with the Trotec Speedy 400 laser engraver in the UC Davis Engineering Student Design Center (ESDC). The laser engraver has an accuracy of ± 0.015 mm across its entire workspace.

Two-toned acrylic, with a thin white layer on top of a black base layer, was utilized to achieve the pattern of the ArUco markers. Laser engraving into the sheet removed the white layer and revealed the black acrylic in specified areas, as shown below in Figure 3.4. Approximately 0.15mm of material was removed from the surface during the engraving process, which was assumed to be negligible such that the markers were still treated as 2D patterns. Each face was also engraved with the corresponding CubeSat testbed ID (A1, A2, B, C1, or C2) and ArUco board axis ($\pm X, Y, Z$). Mounting holes were cut into the acrylic for testbed assembly and ventilation slots were cut to prevent overheating of the CubeSat testbed's Li-ion cells and Raspberry Pi computer.

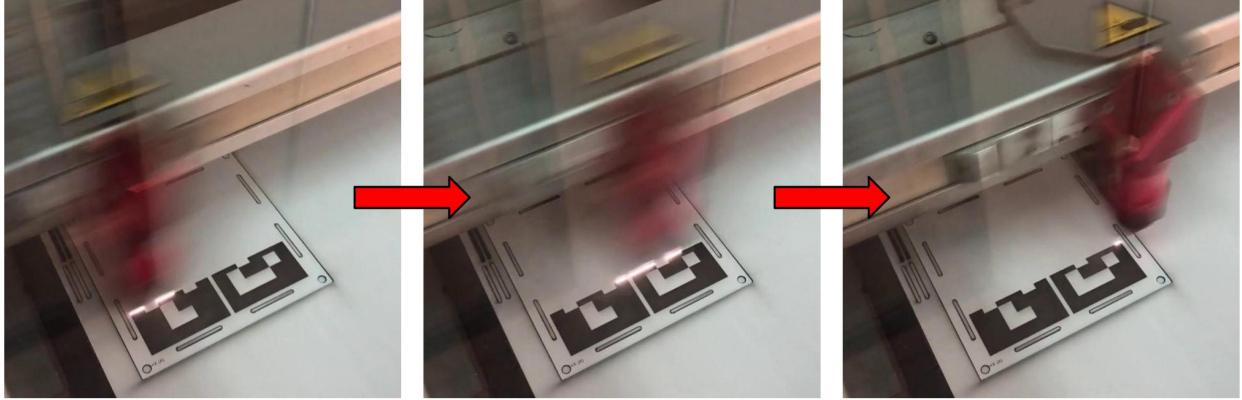


Figure 3.4: ArUco face manufacturing: laser engraving single pass

The CubeSat testbed faces were then assembled together to accurately achieve the physical ArUco board, as shown in Figure 3.5 below.



Figure 3.5: Assembled ArUco faces

3.3 Camera System Design

3.3.1 Introduction

The design of the camera system directly impacted the fidelity of the computer vision results; the cameras needed to record clear video with minimal frame dropouts for accurate marker detection and pose estimation, and they had to be placed such that the experiment

areas had full and redundant coverage. This section presents the camera system design, including: camera selection process, camera system layout, and camera calibration process.

3.3.2 Camera Selection

A camera trade study was conducted to ensure that the ArUco markers could be adequately detected within the 70 in (178 cm) expected operating range of the chamber experiment, defined by the chamber's diagonal distance. The cameras had to provide sufficient video resolution for accurate detection of the markers; low resolution video would blur the edges and patterns of the fiducial markers, making marker detection more difficult and pose estimation less accurate. The cameras also had to provide sufficient frame rate for smooth motion capture and data analysis without measurement aliasing. While the camera FOV was an important consideration, multiple cameras were used together to provide redundant coverage of the experiment areas; therefore, a strict requirement was not set for the FOV.

The camera focus had to be fixed or manually adjustable; although a camera with autofocus may provide clearer video over the entire operating range, the camera calibration focal length parameters would vary every time the camera automatically refocused. It was important that the camera calibration parameters were measured for the specific camera focal length used; mismatches between the two would result in inaccurate pose estimates [13]. Therefore, autofocus was not used for any camera selected; instead, a single adequate focus value was maintained for all experiments. Cameras with manually adjustable focus were preferred over fixed focus cameras such that the focus could be tuned for optimal clarity in the chamber and external experiments, if needed. Manual adjustment came in two forms: physically controlled with a knob or button, and software controlled through user input to a small motor that adjusted the lens. Preference was given to cameras with software-controlled (motorized) focus such that the focus value of each camera could be individually tuned and recorded more easily and precisely, both on the ground and in flight, as needed.

Requirements were set for the CV system cameras based on the Zero-G HDD-RW project needs and on literature review of similar systems [13] [14]. The requirements were as follows:

- The video resolution shall be at least 1080p.
- The video frame rate shall be at least 30 fps.

- The photo quality shall be at least 8MP.
- The cameras shall not use autofocus during experiments .
- The camera focus should be manually adjustable (preference given to software-controlled focus).
- The camera cost shall be no more than \$200 per unit.

Five main cameras were considered for the Zero-G HDD-RW CV system: the GoPro Hero 7, the Logitech C920 HD PRO Webcam, the Raspberry Pi Camera Module V2, the Raspberry Pi High Quality (HQ) Camera, and the Arducam 12MP Camera. It is important to note that the Raspberry PI HQ Camera and the Arducam 12MP camera utilize the same IMX477 sensor, but vary in their focus options. Table [3.1](#) below compares the specifications of each of the camera candidates:

Table 3.1: CV System Camera Trade Study Summary

Camera Model	Diagonal FOV	Video Resolutions & Max Frame Rate	Photo Quality	Focus Options	Unit Cost
GoPro Hero 7 [15]	129.53°	4K / 60 fps 2.7K / 120 fps 1440p / 120 fps 1080p / 240 fps 960p / 240 fps 720p / 240 fps	12 MP	Fixed focus	\$200
Logitech C920 HD PRO Webcam [16]	78°	1080p / 30 fps 720p / 30 fps	15 MP	Autofocus or software defined focus	\$70
RPi Camera Module V2 [17]	73.9°	1080p / 30 fps 720p / 60 fps	8 MP	Fixed focus	\$30
RPi HQ Camera IMX477 [18]	63°	1080p / 30 fps 720p / 60 fps 640p / 90 fps	12 MP	Manually set focus knob	\$50
Arducam 12MP IMX477 [19]	82.72°	1080p / 30 fps 720p / 60 fps 640p / 90 fps	12 MP	Autofocus or software defined focus	\$75

All cameras considered in Table 3.1 met the requirements set for the Zero-G HDD-RW CV system, and thus were all expected to provide sufficient ArUco detection capabilities. Although the GoPro Hero 7 was superior in the video resolution and frame rate categories, the camera had no focus adjustment option; therefore, it was not selected for the Zero-G

HDD-RW project.

Out of the options with manually controllable focus, the Logitech C920 HD PRO Webcam, the Raspberry Pi High Quality (HQ) Camera, and the Arducam 12MP Camera were shown to have similar technical specifications and prices. The Raspberry Pi High Quality (HQ) Camera lacked the software controllable focus of the other two options, so it was also eliminated from consideration.

From further inspection of the Logitech and Arducam camera operations, the Arducam 12MP camera was selected since it provided more compatibility with Raspberry Pi and Python. Compatibility with Raspberry Pi and Python allowed for the system to be highly configurable; for example, the videos were recorded simultaneously with IMU and RTC data, video frames were annotated with experiment information, video file names were customized with experiment-specific naming conventions, and cameras were controlled via a touch screen “control panel” for starting/stopping video and tuning the focus. All Arducam cameras were purchased between September 2021 and May 2022.

3.3.3 Camera Placement Chamber Experiment

A study was performed to determine the optimal camera placement configuration within the chamber experiment area. Each configuration was evaluated based on its total volumetric coverage and redundant volumetric coverage. Total volumetric coverage was quantified as the percentage of the chamber’s volume that fell within the FOV of any one of the cameras in the system - higher total volumetric coverage resulted in fewer “dead zones” where the CubeSat could not be seen by any camera. Redundant coverage was quantified as the percentage of the chamber’s volume that fell within the FOV of any two (or more) of the cameras in the system - it represented the system’s robustness to a single camera failure or occlusion. Three configurations, referred to as A, B, and C, were evaluated. Figure 3.6 below visualizes the camera placement for each configuration and their respective chamber coverage.

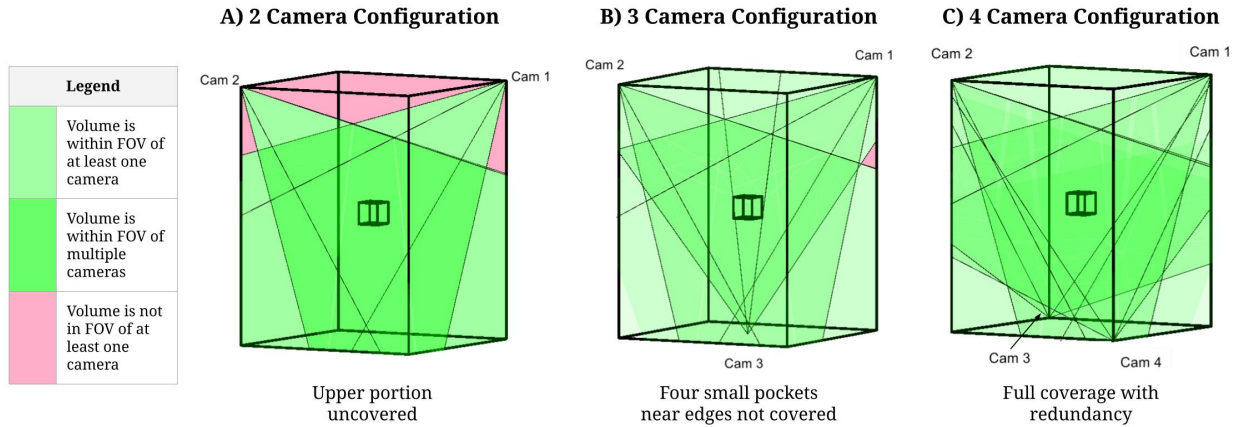


Figure 3.6: Camera configuration comparison

Configuration A consisted of two cameras mounted on opposite corners at the top of the chamber. The cameras were angled downwards at 45 degrees to view the experiment area. Configuration A resulted in 81.0% total volumetric coverage, and 51.0% redundant volumetric coverage with the two cameras. There was a dead zone at the top of the chamber in this configuration, where 19.0% of the chamber’s volume was not within the FOV of any camera.

Configuration B consisted of three cameras - two mounted on opposite corners of the top of the chamber, and one mounted at the bottom center of the chamber. The top cameras were angled downwards at 45 deg, while the bottom camera looked straight upward. Configuration B resulted in 98.4% total volumetric coverage. This configuration also had higher redundant coverage than Configuration A; 61.3% of the chamber’s volume was within the FOV of at least two of the three cameras simultaneously, and 24.4% of the chamber’s volume was within the FOV of all three cameras simultaneously. There were small dead zones along the chamber’s vertical bars where 1.6% of the chamber’s volume was not within the FOV of any camera.

Configuration C consisted of four cameras - two mounted on opposite corners of the top of the chamber, and two mounted on opposite corners of the bottom of the chamber. The top cameras were angled downwards at 45 degrees, while the bottom cameras were angled upwards at 45 degrees. Configuration C achieved 100% total chamber volumetric coverage. This configuration had the highest redundant volumetric coverage; 76.1% of the chamber’s

volume was within the field of view of at least two of the four cameras simultaneously, 57.4% of the chamber’s volume was within the FOV of at least three of the four cameras simultaneously, and 33.4% of the chamber’s volume was within the FOV of all four cameras simultaneously.

Table 3.2 below summarizes the findings of the chamber camera coverage study. Configuration C was chosen for its full chamber volumetric coverage and high redundant volumetric coverage.

Table 3.2: Chamber camera configuration study results

Chamber Volume Coverage Criteria (Results in % of Chamber Volume)	Camera Configuration		
	A	B	C
Dead zone	19.0%	1.6%	0.0%
Total Volumetric Coverage	81.0%	98.4%	100.0%
2 Camera Redundant Volumetric Coverage	51.0%	61.3%	76.1%
3 Camera Redundant Volumetric Coverage	-	24.4%	57.4%
4 Camera Redundant Volumetric Coverage	-	-	33.4%

External Experiment

The external experiment was added for FC2 and FC3, and thus a camera system was added to record video of the external experiment trials. The system was designed to have a single camera, Camera E, mounted on the top of the chamber. The external experiment also utilized a GoPro camera provided by Zero-G Corp that was mounted to the aircraft wall. Together, Camera E and the GoPro provided near 100% total volumetric coverage of the external experiment volume. Although a detailed design study was not performed for the external experiment camera system, the total volumetric coverage was tested experimentally before flight, and proven to not have any significant dead zones that would affect experiment operations or data collection. Because the external experiment volume was larger than the chamber experiment volume, and researchers were floating alongside the testbeds in the external experiment area while performing the trials (leading to frequent occlusion of the CubeSat testbeds), Camera E was added primarily for video documentation of the trials,

rather than for CubeSat testbed pose estimation.

3.3.4 Camera Reference Frame Definition

All pose estimates from OpenCV are defined in the camera’s reference frame. For each camera, this is defined as follows: the x axis points horizontally to the right in the camera’s view, the y axis points vertically downwards in the camera’s view, and the z axis points into camera’s view. The origin is centered in the camera’s view.

3.3.5 Calibration

Introduction

OpenCV represents cameras with a simple pinhole model that assumes all light passes through a single point in the camera. While this model is useful, it does not accurately describe the use of a real camera. Real cameras use lenses to gather more light than a pinhole camera; this leads to higher quality images and videos with rapid exposures, but it also introduces distortion into each frame. To represent a real camera with the OpenCV pinhole model, the camera must be calibrated to quantify its distortion parameters and intrinsic parameters. The distortion parameters consist of radial and tangential distortion coefficients, while the intrinsic parameters consist of the camera’s focal length and optical center.

These parameters are combined to remove distortion in images and videos and to establish a relationship between 2D points in the recorded frames and 3D points in the real world; therefore, calibration must occur prior to extracting pose information from ArUco markers. Calibration was a crucial step in the development of the CV system, and had to be performed thoroughly and correctly to ensure the accuracy of the ArUco pose estimation. The calibration parameters do not change with the operation of the camera, as long as no camera settings (e.g. focus values) change; therefore, the process only had to be performed once for each camera at its specified focus value. The equations and methodology presented in this section are found in [20], [21], and [22].

Distortion Parameters

There are two main types of distortion: radial and tangential. Radial distortion depends on the curvature of a camera’s lens, and makes straight lines appear curved or “fisheye”

near the edges of an image. Radial distortion is represented as follows in Equation 3.1 and Equation 3.2, where (x, y) corresponds to the original location of a point on an image in the camera's reference frame, $(x_{corrected}, y_{corrected})$ corresponds to the new location of the corrected point in the camera's reference frame, r corresponds to the radial distance from the optical center, and k_1 , k_2 , and k_3 correspond to the radial distortion coefficients. Note that k_3 is often set to zero for lenses without high distortion.

$$x_{corrected} = x(1 + k_1r^2 + k_2r^4 + k_3r^6) \quad (3.1)$$

$$y_{corrected} = y(1 + k_1r^2 + k_2r^4 + k_3r^6) \quad (3.2)$$

Tangential distortion arises from manufacturing imperfections that cause the camera's lens to not be perfectly parallel to the imaging plane. It results in rotation and/or skew of the image. Tangential distortion is represented as follows in Equation 3.3 and Equation 3.4 where (x, y) corresponds to the original location of a point on an image in the camera's reference frame, $(x_{corrected}, y_{corrected})$ corresponds to the new location of the corrected point in the camera's reference frame, r corresponds to the radial distance from the optical center, and p_1 and p_2 refer to the tangential distortion coefficients.

$$x_{corrected} = x + [2p_1xy + p_2(r^2 + 2x^2)] \quad (3.3)$$

$$y_{corrected} = y + [p_1(r^2 + 2y^2) + 2p_2xy] \quad (3.4)$$

The distortion coefficients are combined into a 5x1 distortion vector as shown in Equation 3.5 below:

$$\text{Distortion Coefficients} = (k_1, k_2, p_1, p_2, k_3) \quad (3.5)$$

Intrinsic Parameters

The intrinsic parameters describe the camera's focal length (f_x, f_y) and optical center (c_x, c_y) . The focal length describes the distance between the optical center of the lens and the camera's sensor. The optical center parameters describe the displacement between the camera's imaging chip and the center of the image plane (caused by manufacturing imperfections). The focal length and optical center parameters are combined into a 3x3 camera matrix in OpenCV, as described below in Equation 3.6:

$$\begin{bmatrix} f_x & 0 & c_x \\ 0 & f_y & c_y \\ 0 & 0 & 1 \end{bmatrix} \quad (3.6)$$

Extrinsic Parameters

In addition to evaluating the distortion parameters and intrinsic parameters of the camera, the pose of the calibration target is also determined and stored in the extrinsic matrix. The extrinsic matrix consists of a rotation matrix and translation vector that describe the rotation and position of the calibration target in the camera's reference frame, as described in Equation 3.7 below. While the distortion and intrinsic parameters of a camera stay constant with a camera's operation (given that the camera settings, such as focal length, do not change), the extrinsic matrix changes as the calibration target is moved to different poses.

$$W = \begin{bmatrix} R_{3x3} & t_{3x1} \end{bmatrix} \quad (3.7)$$

Reprojection Error

After calculating a camera's distortion parameters and intrinsic parameters, it is necessary to quantify the accuracy of the calibration process - both for the calibration image dataset as a whole and for each individual calibration image. This can provide insight regarding the quality of the calibration, and can also identify images that should be removed from consideration during the calibration process; for example, some input calibration images may be subject to motion blur, occlusion, reflection or improper lighting, or the calibration target may be too far away for proper detection.

A common method of quantifying calibration accuracy is through reprojection error. First, the calibration is performed: points on a well-known calibration pattern are detected, from which the distortion, intrinsic, and extrinsic parameters are calculated. Next, the distortion, intrinsic, and extrinsic parameters are used to reproject the calibration pattern onto the image to estimate the originally detected points. The difference between the estimated points and the detected points in the image yields the reprojection error. OpenCV defines reprojection error as the total sum of squared distances between the detected points and the reprojected points in an image; the RMS of total reprojection error is returned for both the

individual images and for the calibration as a whole.

A reprojection error threshold of 1.0px was set for FC1 in the Zero-G HDD-RW camera calibration process based on evaluation of the calibration results. Visual inspection of the calibration images showed that in the FC1 images with a reprojection error of 1.0px or higher, the calibration board was generally subject to motion blur, was placed at a high rotation angle, or was very far from the camera. Similarly, a reprojection error threshold of 0.6px was set for FC2 and FC3. A smaller calibration board was used for FC2 and FC3 than FC1, since it needed to fit in the aircraft's onboard storage during flight. Any images that yielded an RMS reprojection error greater than the threshold would be removed from the calibration image set, and the calibration would be performed again with only the images that previously passed the reprojection threshold.

Camera Calibration Process

Planar checkerboards are often used as calibration targets for their well-known and easily detectable pattern. To ensure that the calibration is as accurate as possible, it is important for the checkerboard to be rigid, high contrast, and minimally reflective. The pattern must also be sized appropriately to be detected by the calibration process at varying distances from the camera.



Figure 3.7: Calibration target with checkerboard corners detected (indicated with colored circles) and rows detected (indicated with straight lines connecting like-colored circles)

For the Zero-G HDD-RW experiment, a black and white checkerboard pattern (shown above in Figure 3.7) was printed on an aluminum sheet (1/8" thick) and stored at the bottom of the chamber. During the calibration procedure, the pattern was displayed by hand in front of each camera at varying distances and angles relative to the camera. It was also moved laterally across the camera's FOV at varying distances to capture the distortion near the edges of the FOV. A video was recorded of the calibration procedure, from which frames were extracted and stored as images. Images of the calibration procedure were fed into a Python script that utilized OpenCV's calibration procedure. Note that the calibration procedure was performed on the ground for FC1 and in-flight for FC2 and FC3. Calibrating in flight yielded a more accurate camera calibration model, since the calibration procedure was performed in the operating environment. The calibration procedure is summarized below in Figure 3.8.

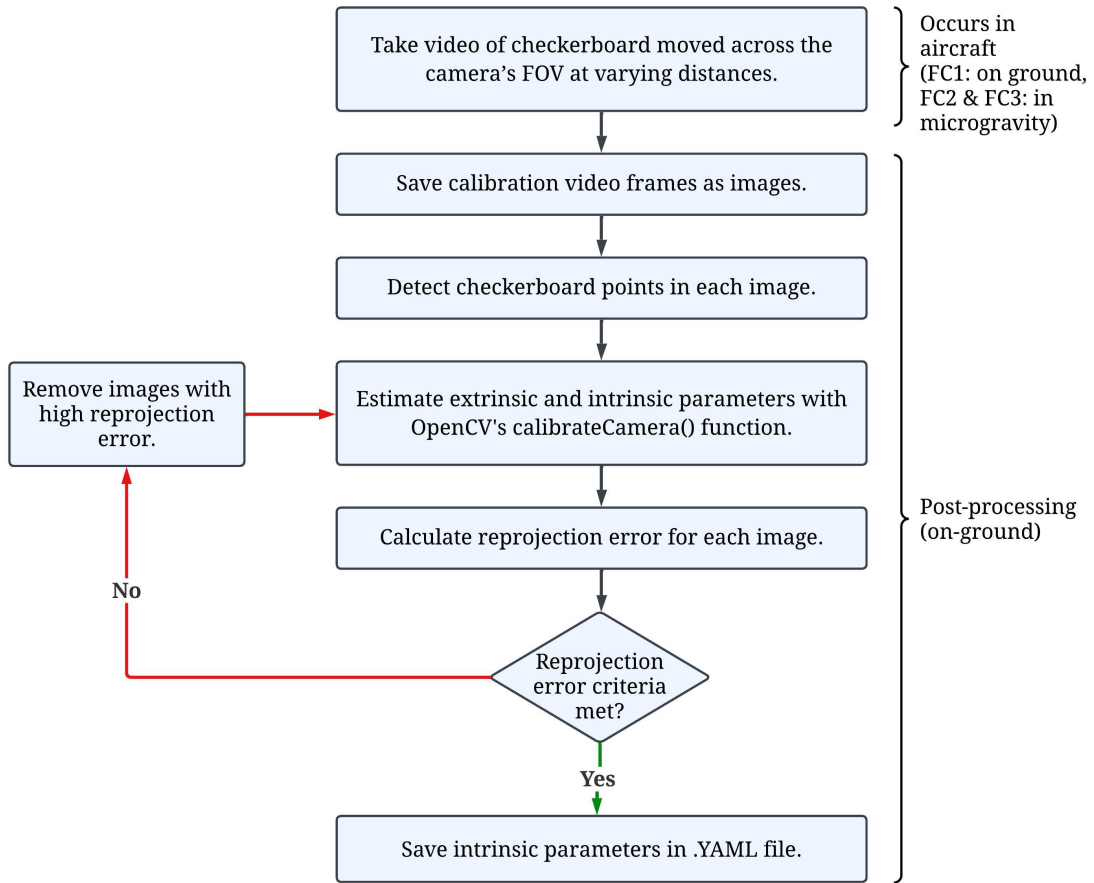


Figure 3.8: Camera Calibration Procedure

Camera Calibration Results

Table 3.3 below summarizes the calibration environment and reprojection RMS error for each of the cameras in each flight campaign. The next sections will then describe the results for each camera in detail.

Table 3.3: Camera calibration results summary

FC	Camera	Calibration Environment	Focus	Num. of Images	Reprojection RMS Error (px)
1	A	On ground	0	181	0.662 px
	B	Not calibrated	0	N/A	Assumed same as FC1 Cam A
	C	Not calibrated	0	N/A	Assumed same as FC1 Cam A
	D	Not calibrated	0	N/A	Assumed same as FC1 Cam A
	E	N/A	N/A	N/A	N/A: No external experiment
	GOPRO	N/A	N.A	N/A	N/A: No external experiment
2	A	0G (F4)	85	78	0.193 px
	B	0G (F4)	25	51	0.117 px
	C	0G (F4)	170	185	0.288 px
	D	0G (F4)	75	100	0.242 px
	E	Not calibrated	0	N/A	Assumed same as FC3 Cam E
	GOPRO	Not calibrated	0	N/A	Assumed same as FC3 GOPRO
3	A	0G (F5)	85	96	0.254 px
	B	0G (F5)	25	42	0.240 px
	C	0G (F5)	170	43	0.260 px
	D	0G (F5)	75	73	0.318 px
	E	0G (F5)	0	83	0.152 px
	GOPRO	0G (F6)	Default	48	0.144 px

Flight Campaign 1

Camera A A total of 199 images were recorded for Camera A’s FC1 calibration. During the checkerboard pattern detection step, 17 images were rejected for partial or full failure of pattern detection. On the first round of calibration, the overall reprojection RMS error was .665 px; 1 image was then identified to fail the reprojection error criteria, and was removed from the dataset. The calibration was performed again with the 181 accepted images, resulting in a final overall reprojection RMS error of 0.662 px. The resulting distortion parameters, camera matrix, and RMS reprojection errors are shown below in Table 3.4.

Table 3.4: Calibration Results for Camera A (FC1)

Distortion Vec. (Eq. 3.5)	$\begin{bmatrix} 1.399e - 02 & 6.440e - 02 & 2.119e - 04 & 4.599e - 04 & -3.863e - 01 \end{bmatrix}$
Camera Matrix (Eq. 3.6)	$\begin{bmatrix} 1.278e + 03 & 0. & 9.712e + 02 \\ 0. & 1.277e + 03 & 5.164e + 02 \\ 0. & 0. & 1. \end{bmatrix}$
RMS Reprojection Error with Failed Points	<p>Reprojection RMS Error First Iteration - Including Outliers Flight Campaign 1: Camera A Calibration</p> <p>Reprojection RMS Error (px)</p> <p>Image Number</p> <p>• Non-Outlier • Outlier --- Overall RMS Error: 0.665 px</p>
RMS Reprojection Error - Final	<p>Reprojection RMS Error Final - No Outliers Flight Campaign 1: Camera A Calibration</p> <p>Reprojection RMS Error (px)</p> <p>Image Number</p> <p>• Non-Outlier --- Overall RMS Error: 0.662 px</p>

Flight Campaign 2

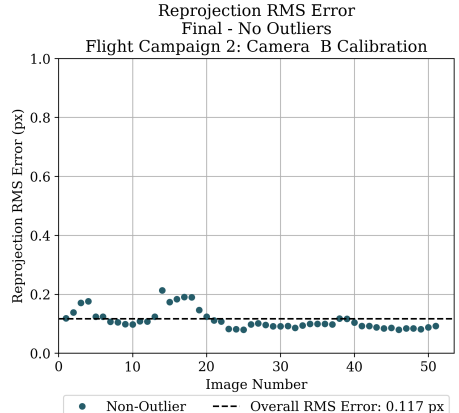
Camera A A total of 169 images were recorded for Camera A’s FC2 calibration. During the pattern detection step, 89 images were rejected for partial or full failure of pattern detection. On the first round of calibration, the overall reprojection RMS error was 0.902 px; 3 images were then identified to fail the reprojection error criteria, and were removed from the dataset. The calibration was performed again with the 77 accepted images, resulting in a final overall reprojection RMS error of 0.193 px. The resulting distortion parameters, camera matrix, and RMS reprojection errors are shown below in Table 3.5.

Table 3.5: Calibration Results for Camera A (FC2)

Distortion Vec. (Eq. 3.5)	$\begin{bmatrix} 8.531e-02 & -7.279e-01 & 5.025e-04 & 1.071e-03 & 2.400e+00 \end{bmatrix}$
Camera Matrix (Eq. 3.6)	$\begin{bmatrix} 1.261e+03 & 0. & 9.759e+02 \\ 0. & 1.260e+03 & 5.140e+02 \\ 0. & 0. & 1. \end{bmatrix}$
RMS Reprojection Error with Failed Points	
RMS Reprojection Error - Final	

Camera B A total of 51 images were recorded in Camera B’s FC2 calibration procedure. During the checkerboard pattern detection step, 0 images were rejected for partial or full failure of pattern detection. The calibration resulted in a final overall reprojection RMS error of 0.117 px, with no images failing the reprojection criteria; therefore, only one round of calibration was necessary. The resulting distortion parameters, camera matrix, and RMS reprojection errors are shown below in Table 3.6.

Table 3.6: Calibration Results for Camera B (FC2)

Distortion Vec. (Eq. 3.5)	$\begin{bmatrix} 5.754e - 02 & -2.719e - 01 & 3.491e - 04 & 7.960e - 04 & 4.722e - 01 \end{bmatrix}$
Camera Matrix (Eq. 3.6)	$\begin{bmatrix} 1.205e + 03 & 0. & 9.498e + 02 \\ 0. & 1.205e + 03 & 5.940e + 02 \\ 0. & 0. & 1. \end{bmatrix}$
RMS Reprojection Error - Final	

Camera C A total of 197 images were recorded in Camera C’s FC2 calibration procedure. During the checkerboard pattern detection step, 10 images were rejected for partial or full failure of pattern detection. On the first round of calibration, the overall reprojection RMS error was 0.394 px; 3 images were then identified to fail the reprojection error criteria, and were removed from the dataset. The calibration was performed again with the 184 accepted images, resulting in a final overall reprojection RMS error of 0.288 px. The resulting distortion parameters, camera matrix, and RMS reprojection errors are shown below in Table 3.7.

Table 3.7: Calibration Results for Camera C (FC2)

Distortion Vec. (Eq. 3.5)	$\begin{bmatrix} 7.654e - 02 & -3.252e - 01 & -3.760e - 03 & 3.770e - 03 & 5.045e - 01 \end{bmatrix}$
Camera Matrix (Eq. 3.6)	$\begin{bmatrix} 1.293e + 03 & 0. & 9.492e + 02 \\ 0. & 1.291e + 03 & 4.991e + 02 \\ 0. & 0. & 1. \end{bmatrix}$
RMS Reprojection Error with Failed Points	<p style="text-align: center;">Reprojection RMS Error First Iteration - Including Outliers Flight Campaign 2: Camera C Calibration</p> <p style="text-align: center;">Reprojection RMS Error (px)</p> <p style="text-align: center;">Image Number</p> <p style="text-align: center;">● Non-Outlier ● Outlier --- Overall RMS Error: 0.394 px</p>
RMS Reprojection Error - Final	<p style="text-align: center;">Reprojection RMS Error Final - No Outliers Flight Campaign 2: Camera C Calibration</p> <p style="text-align: center;">Reprojection RMS Error (px)</p> <p style="text-align: center;">Image Number</p> <p style="text-align: center;">● Non-Outlier --- Overall RMS Error: 0.288 px</p>

Camera D A total of 103 images were recorded in Camera D’s FC2 calibration procedure. During the checkerboard pattern detection step, 0 images were rejected for partial or full failure of pattern detection. On the first round of calibration, the overall reprojection RMS error was 0.351 px; 3 images were then identified to fail the reprojection error criteria, and were removed from the dataset. The calibration was performed again with the 100 accepted images, resulting in a final overall reprojection RMS error of 0.242 px. The resulting distortion parameters, camera matrix, and RMS reprojection errors are shown below in Table 3.8.

Table 3.8: Calibration Results for Camera D (FC2)

Distortion Vec. (Eq. 3.5)	$\begin{bmatrix} 5.357e - 02 & -2.408e - 01 & 4.940e - 04 & 7.430e - 04 & 1.126e - 01 \end{bmatrix}$
Camera Matrix (Eq. 3.6)	$\begin{bmatrix} 1.271e + 03 & 0. & 9.631e + 02 \\ 0. & 1.270e + 03 & 5.586e + 02 \\ 0. & 0. & 1. \end{bmatrix}$
RMS Reprojection Error with Failed Points	<p>Reprojection RMS Error First Iteration - Including Outliers Flight Campaign 2: Camera D Calibration</p> <p>Reprojection RMS Error (px)</p> <p>Image Number</p> <p>● Non-Outlier ● Outlier --- Overall RMS Error: 0.351 px</p>
RMS Reprojection Error - Final	<p>Reprojection RMS Error Final - No Outliers Flight Campaign 2: Camera D Calibration</p> <p>Reprojection RMS Error (px)</p> <p>Image Number</p> <p>● Non-Outlier --- Overall RMS Error: 0.242 px</p>

Flight Campaign 3

Camera A A total of 104 images were recorded for Camera A’s FC3 calibration. During the pattern detection step, 7 images were rejected for partial or full failure of pattern detection. On the first round of calibration, the overall reprojection RMS error was 0.271 px; one image was then identified to fail the reprojection error criteria, and was removed from the dataset. The calibration was performed again with the 96 accepted images, resulting in a final overall reprojection RMS error of 0.254 px. The resulting distortion parameters, camera matrix, and RMS reprojection errors are shown below in Table 3.9.

Table 3.9: Calibration Results for Camera A (FC3)

Distortion Vec. (Eq. 3.5)	$\begin{bmatrix} 1.278e - 01 & -1.035e + 0 & -3.443e - 03 & -4.063e - 03 & 3.078 + 00 \end{bmatrix}$
Camera Matrix (Eq. 3.6)	$\begin{bmatrix} 1.261e + 03 & 0. & 9.545e + 02 \\ 0. & 1.259e + 03 & 5.104e + 02 \\ 0. & 0. & 1. \end{bmatrix}$
RMS Reprojection Error with Failed Points	
RMS Reprojection Error - Final	

Camera B A total of 53 images were recorded in Camera B’s FC3 calibration procedure. During the checkerboard pattern detection step, 11 images were rejected for partial or full failure of pattern detection. The calibration results in a final overall reprojection RMS error of 0.240 px, with no images failing the reprojection criteria; therefore, only one round of calibration was necessary. The resulting distortion parameters, camera matrix, and RMS reprojection errors are shown below in Table 3.10.

Table 3.10: Calibration Results for Camera B (FC3)

Distortion Vec. (Eq. 3.5)	$\begin{bmatrix} 6.854e - 02 & -4.417e - 01 & 9.300e - 04 & -1.883e - 03 & 7.472e - 01 \end{bmatrix}$
Camera Matrix (Eq. 3.6)	$\begin{bmatrix} 1.263e + 03 & 0. & 9.590e + 02 \\ 0. & 1.264e + 03 & 5.981e + 02 \\ 0. & 0. & 1. \end{bmatrix}$
RMS Reprojection Error - Final	

Camera C A total of 48 images were recorded in Camera C’s FC3 calibration procedure. During the checkerboard pattern detection step, 5 images were rejected for partial or full failure of pattern detection. The calibration results in a final overall reprojection RMS error of 0.260px, with no images failing the reprojection criteria; therefore, only one round of calibration was necessary. The resulting distortion parameters, camera matrix, and RMS reprojection errors are shown below in 3.11.

Table 3.11: Calibration Results for Camera C (FC3)

Distortion Vec. (Eq. 3.5)	$\begin{bmatrix} 5.838e - 02 & -3.350e - 01 & -8.249e - 04 & -1.844e - 03 & 5.760e - 01 \end{bmatrix}$
Camera Matrix (Eq. 3.6)	$\begin{bmatrix} 1.303e + 03 & 0. & 9.206e + 02 \\ 0. & 1.303e + 03 & 4.945e + 02 \\ 0. & 0. & 1. \end{bmatrix}$
RMS Reprojection Error - Final	

Camera D A total of 78 images were recorded in Camera C’s FC3 calibration procedure. During the checkerboard pattern detection step, 5 images were rejected for partial or full failure of pattern detection. The calibration results in a final overall reprojection RMS error of 0.318px, with no images failing the reprojection criteria; therefore, only one round of calibration was necessary. The resulting distortion parameters, camera matrix, and RMS reprojection errors are shown below in 3.12.

Table 3.12: Calibration Results for Camera D (FC3)

Distortion Vec. (Eq. 3.5)	$\begin{bmatrix} 1.012e - 01 & -6.028e - 01 & -8.071e - 03 & 2.815e - 03 & 1.173e + 00 \end{bmatrix}$
Camera Matrix (Eq. 3.6)	$\begin{bmatrix} 1.252e + 03 & 0. & 9.708e + 02 \\ 0. & 1.251e + 03 & 5.275e + 02 \\ 0. & 0. & 1. \end{bmatrix}$
RMS Reprojection Error - Final	

Camera E A total of 351 images were recorded in Camera E’s FC3 calibration procedure. During the checkerboard pattern detection step, 67 images were rejected for partial or full failure of pattern detection. On the first round of calibration, the overall reprojection RMS error was 5.729 px; 201 images were then identified to fail the reprojection error criteria, and were removed from the dataset. The calibration was performed again with the 83 accepted images, resulting in a final overall reprojection RMS error of 0.152 px. The resulting distortion parameters, camera matrix, and RMS reprojection errors are shown below in Table 3.13.

Table 3.13: Calibration Results for Camera E (FC3)

Distortion Vec. (Eq. 3.5)	$\begin{bmatrix} 1.281e - 01 & -8.591e - 01 & 8.228e - 04 & 7.151e - 05 & 2.025e + 00 \end{bmatrix}$
Camera Matrix (Eq. 3.6)	$\begin{bmatrix} 1.328e + 03 & 0. & 9.594e + 02 \\ 0. & 1.333e + 03 & 4.894e + 02 \\ 0. & 0. & 1. \end{bmatrix}$
RMS Reprojection Error with Failed Points	<p>Reprojection RMS Error First Iteration - Including Outliers Flight Campaign 3: Camera E Calibration</p> <p>Reprojection RMS Error (px)</p> <p>Image Number</p> <p>● Outlier ● Non-Outlier --- Overall RMS Error: 5.729 px</p>
RMS Reprojection Error - Final	<p>Reprojection RMS Error Final - No Outliers Flight Campaign 3: Camera E Calibration</p> <p>Reprojection RMS Error (px)</p> <p>Image Number</p> <p>● Non-Outlier --- Overall RMS Error: 0.152 px</p>

Go Pro A total of 95 images were recorded in the GoPro’s FC3 calibration procedure. During the checkerboard pattern detection step, 8 images were rejected for partial or full failure of pattern detection. On the first round of calibration, the overall reprojection RMS error was 4.396 px; 42 images were then identified to fail the reprojection error criteria, and were removed from the dataset. The calibration was performed again with the 45 accepted images, resulting in a final overall reprojection RMS error of 0.144 px. The resulting distortion parameters, camera matrix, and RMS reprojection errors are shown below in Table 3.14.

Table 3.14: Calibration Results for GoPro (FC3)

Distortion Vec. (Eq. 3.5)	$\begin{bmatrix} -3.201e - 01 & 3.923e - 01 & -3.169e - 03 & 9.619e - 04 & -5.176e - 01 \end{bmatrix}$
Camera Matrix (Eq. 3.6)	$\begin{bmatrix} 9.521e + 02 & 0. & 9.722e + 02 \\ 0. & 9.528e + 02 & 5.457e + 02 \\ 0. & 0. & 1. \end{bmatrix}$
RMS Reprojection Error with Failed Points	
RMS Reprojection Error - Final	

3.4 Computer Vision System Ground Testing

3.4.1 Introduction

On-ground testing of the computer vision system served two main purposes: 1) tuning the ArUco board detection and pose estimation parameters and 2) quantifying the accuracy and noise of the computer vision system across multiple CubeSat testbed poses within the expected operating range. While initial accuracy and noise estimates for ArUco markers could be gathered from literature review, there were several variables that made the Zero-G HDD-RW computer vision system unique and that necessitated system characterization - including the camera selection, marker dictionary, marker size, board layout, calibration procedure, operating range, and operating environment. The following sections detail the ground testing experiment procedure, results, conclusions, and limitations.

3.4.2 Experiment Procedure

To characterize the performance of the CV system, the CubeSat testbed was placed in multiple predetermined static poses relative to Camera E while it recorded video; CubeSat testbed pose estimates were then determined from post processing Camera E's videos and were compared to known ground truth values. Since all cameras in the CV system were of the same model and underwent the same calibration process, it was assumed that the performance of all cameras would be similar to Camera E's performance. Accurate, repeatable placement of the CubeSat testbed in the predetermined poses was crucial for ensuring trustworthy ground truth pose measurements. A Universal Robotics UR5e robot arm in the HRVIP lab was chosen as the appropriate tool for performing the CubeSat testbed placement, due to its pose repeatability of ± 0.03 mm. The CubeSat testbed was mounted on the UR5e tool flange with a custom laser cut mount designed by UC Davis undergraduate student Zoe Wilf, as shown below in Figure 3.9.

Camera E was mounted to the rigid structure of the chamber, which was placed in front of the robot arm and securely bolted to a floor plate to prevent movement or misalignment during the test. The predetermined poses in the experiment set were defined in Camera E's coordinate system. Since inputs to the robot arm had to be defined in the robot's own coordinate system, it was first necessary to determine the coordinate transformation between

Camera E's coordinate system, the robot arm's coordinate system, and the CubeSat testbed's coordinate system - all of which are defined below in Figure 3.10.

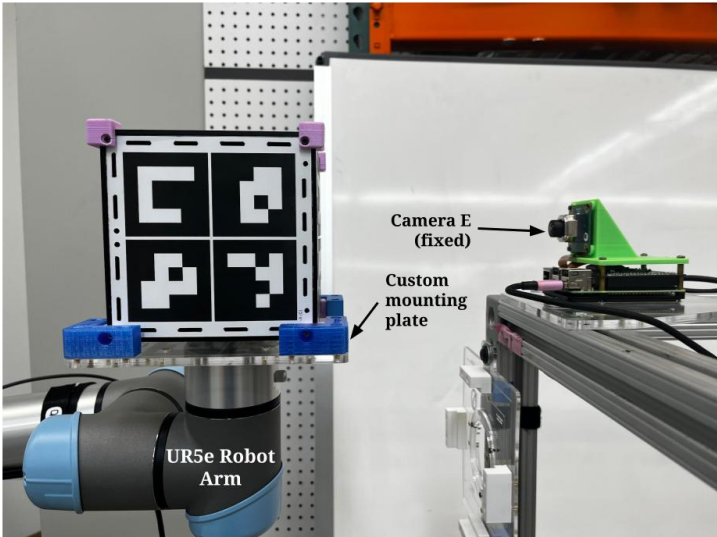


Figure 3.9: CubeSat testbed mounted on tool flange of UR5e robot arm and positioned in front of Camera E

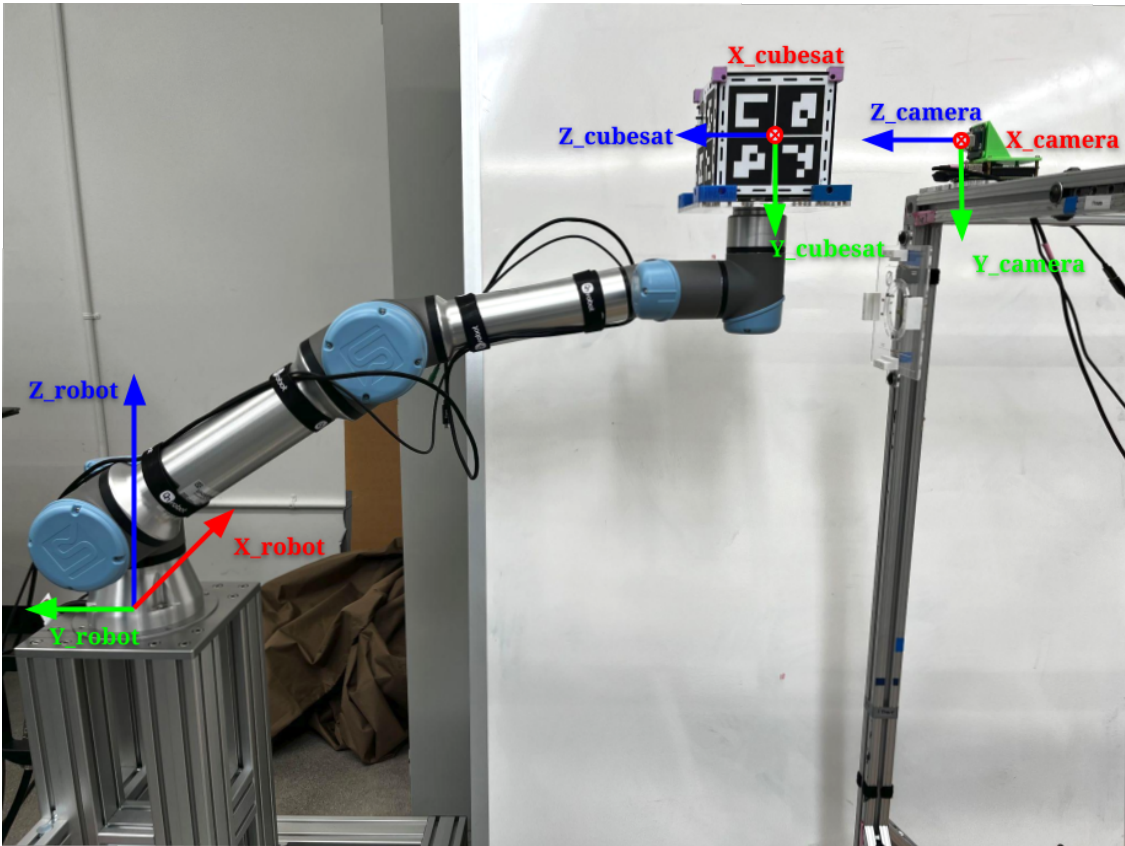


Figure 3.10: Coordinate system definition for robot arm, CubeSat testbed, and Camera E

First, the rotation between the robot and camera coordinate system was determined. By aligning a laser with the robot's y axis, and projecting it along the chamber bar that was aligned with the camera's z axis, the angle between the robot's y axis and the chamber was measured to be 0.12° . Thus, the angle between the camera's z axis and the robot's y axis was taken as 0.12° . Next, a custom laser cut zeroing touch plate designed by UC Davis undergraduate student Zoe Wilf was mounted securely to the chamber below Camera E. The touch plate provided a known zeroing point for the UR5e arm/CubeSat testbed assembly to an accuracy of ± 0.150 mm in the robot arm's x, y, and z axes. The distance between the zeroing plate and Camera E's lens was measured with calipers, as shown in Figure 3.12. The UR5e was then moved until the CubeSat testbed face pressed securely against the touch plate, as shown below in Figure 3.11. The CubeSat testbed's x, y, and z distances and rotations were recorded in the robot's coordinate system at the zeroing position. Combined with the known distance between the zeroing plate and Camera E, the transformation between the CubeSat testbed's geometric center in the robot's reference frame and Camera E's reference frame was determined. The predetermined poses were then converted from Camera E's reference frame to the robot's reference frame, so that the arm could be commanded into the predetermined poses.

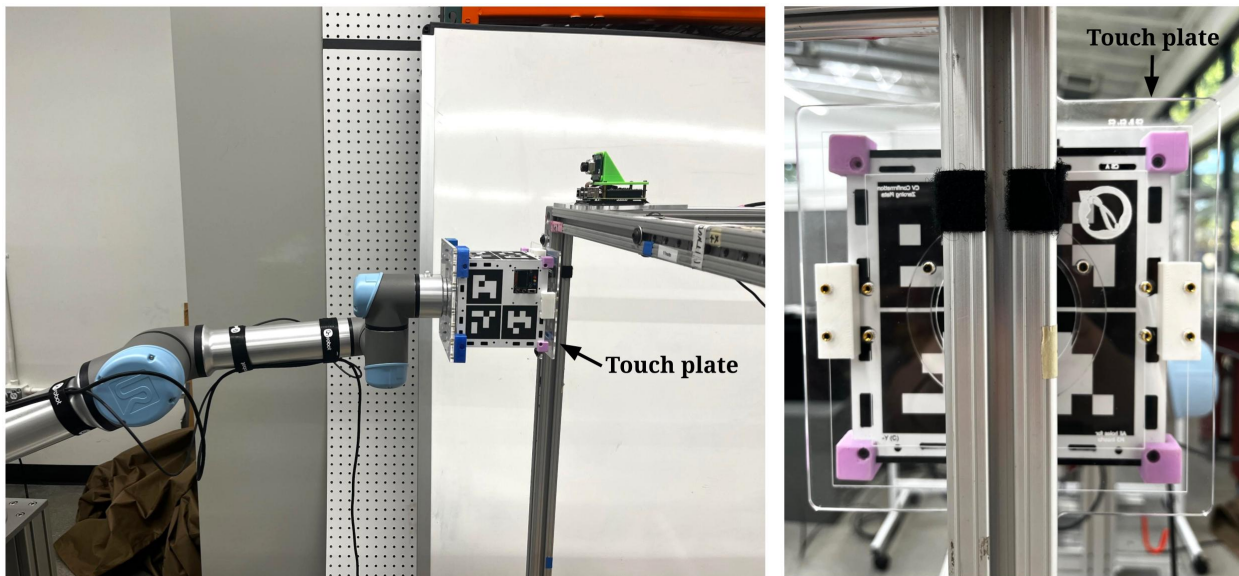


Figure 3.11: Robot arm in zeroed position (left) and close-up view of zeroing touch plate (right)

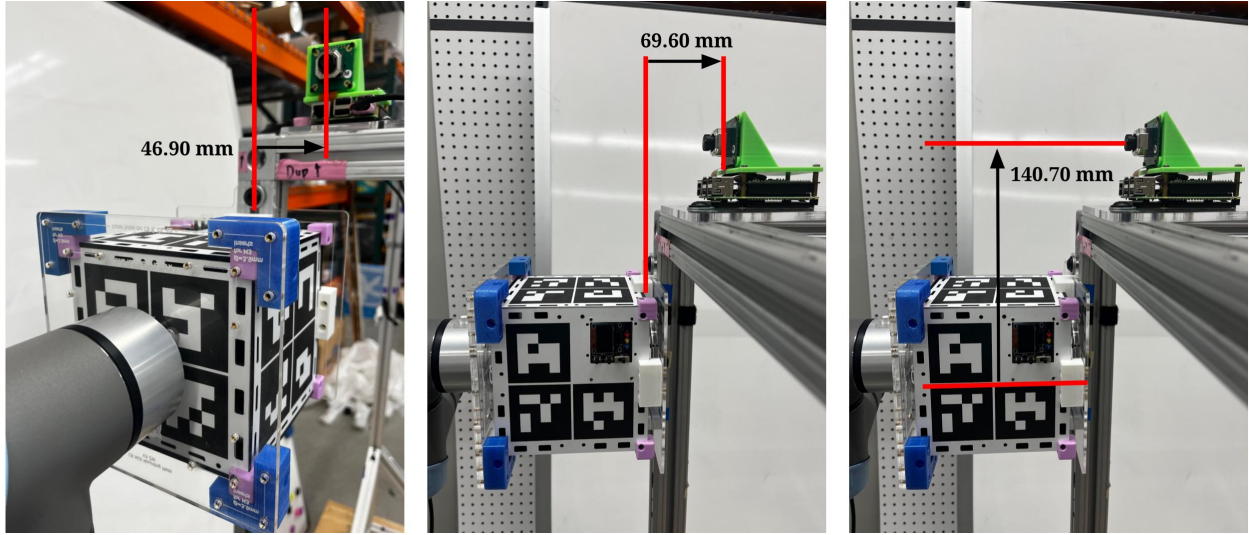


Figure 3.12: Zeroing touch plate to Camera E Measurements

A total of twenty unique poses were tested along the camera's centerline. The experimental set's upper distance limit was bounded by the length of the chamber's diagonal, which was the maximum operating distance from any camera to the CubeSat testbed during chamber experiments, while the lower limit was bounded by the minimum operating distance from any camera to the CubeSat testbed during chamber experiments, which was taken as 15% of the chamber's diagonal. Five distances were chosen in the experimental set: 15% of the chamber's diagonal (26.8 cm), 25% of the chamber's diagonal (44.6 cm), 50% of the chamber's diagonal (89.3 cm), 75% of the chamber's diagonal (133.9 cm), and 100% of the chamber's diagonal (178.6 cm). At each of these five distances, the CubeSat testbed was rotated about its y axis, which was aligned with the camera's y axis, to four predetermined rotations: 0° , 15° , 30° , and 45° . Note that the CubeSat testbed was not rotated about its x and z axes for any poses in the experimental set; however, given additional time, it would be recommended to perform this additional testing. Each of the poses in the experimental set are demonstrated below in Figure 3.13.

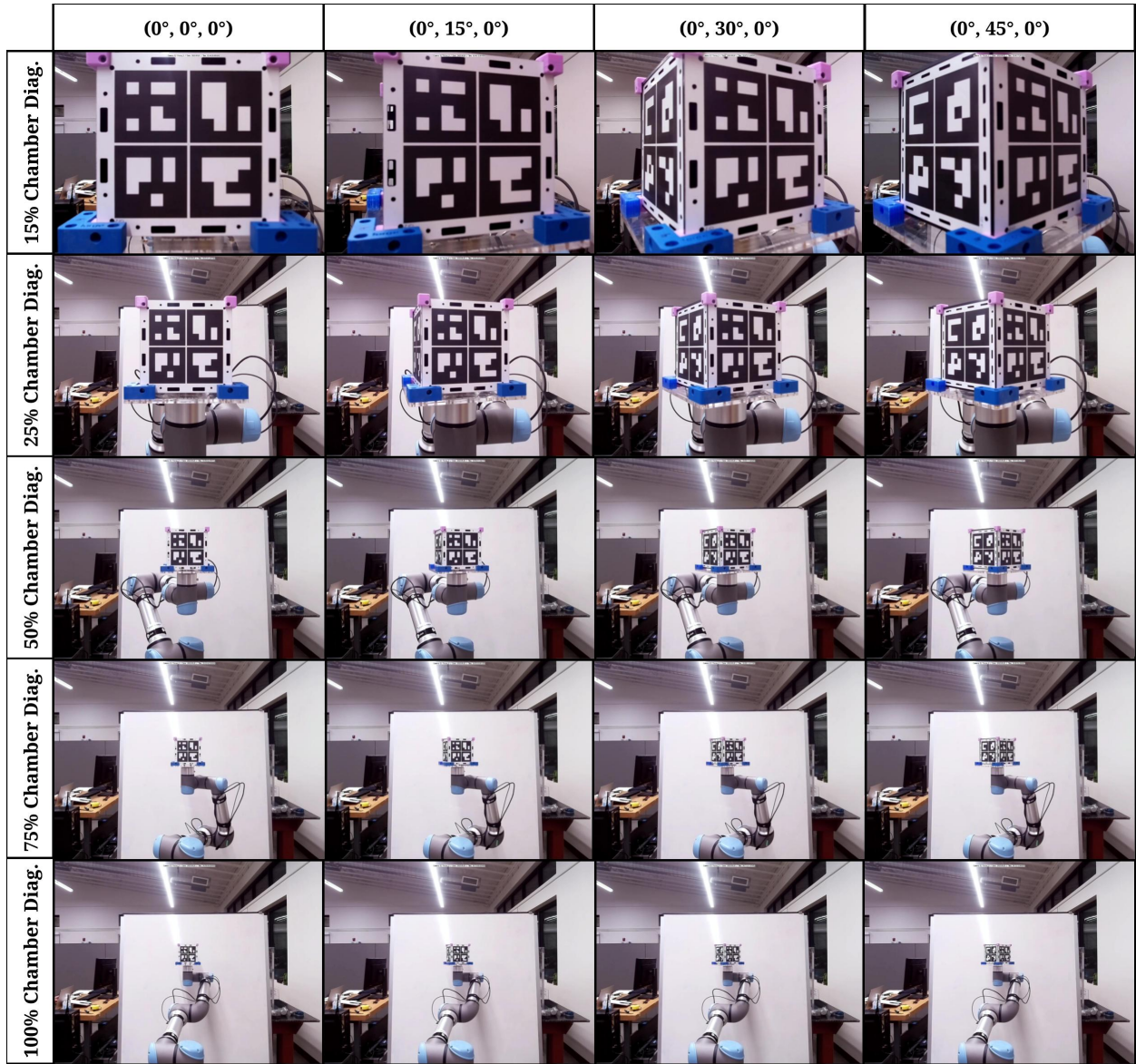


Figure 3.13: CubeSat testbed experiment pose set

At each pose, a 15-17 second 30fps video was recorded of the CubeSat testbed, resulting in approximately 450-500 video frames of the CubeSat testbed per pose. Each video was post processed to estimate the ArUco board's pose. Results from the ArUco board pose estimation were compared against the known robot arm pose to characterize the accuracy and noise of the ArUco detection in each pose. Figure 3.14 below summarizes the ground testing experiment procedure.

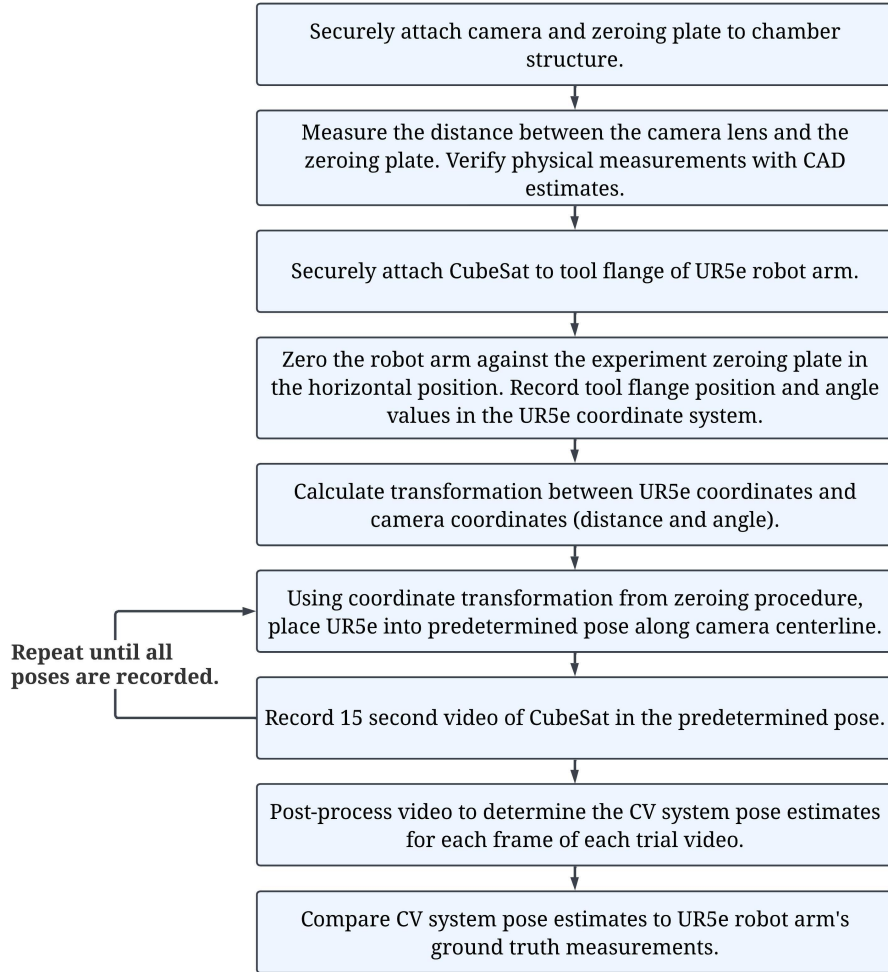


Figure 3.14: Summary of CV system ground testing procedure

3.4.3 Ground Testing Results

After performing the ground test procedure, the videos were post-processed to estimate the CubeSat testbed's pose at each step. The following results characterize the CV system's accuracy and noise in both distance and angle.

Distance Results

CV Measured Distance versus Ground Truth Distance Figure 3.15 below demonstrates the CV system's distance measurements of the CubeSat testbed in Camera E's reference frame versus the ground truth distance (measured by the robot arm) for each pose in the experiment set. The measurement index plotted on the x axis corresponds to the total number of frames processed in the experiment, while the y axes correspond to the CubeSat's

distance value in the camera's x, y, and z axes.

During the experiment, the CubeSat testbed was moved backward along the camera's z axis, but kept fixed in position along the camera's x and y axes. The z axis measurements were shown to follow the ground truth distance values for each pose in the experiment set, with increasing error as the CubeSat testbed moved further away from the camera. While the CubeSat testbed was only moved along the camera's z axis, errors were also evident in the x and y axes, with the highest absolute measurement error at the most distant positions. Note that at the most distant position, the percent error in the x and y axes were both less than 1%. The points where the highest measurement noise was demonstrated corresponded to the orientation where the CubeSat testbed was facing the camera directly, with 0° rotation in all axes. This indicated that the CV distance estimation error and measurement noise in each axis was dependent on both the CubeSat testbed's distance from the camera and on its orientation relative to the camera.

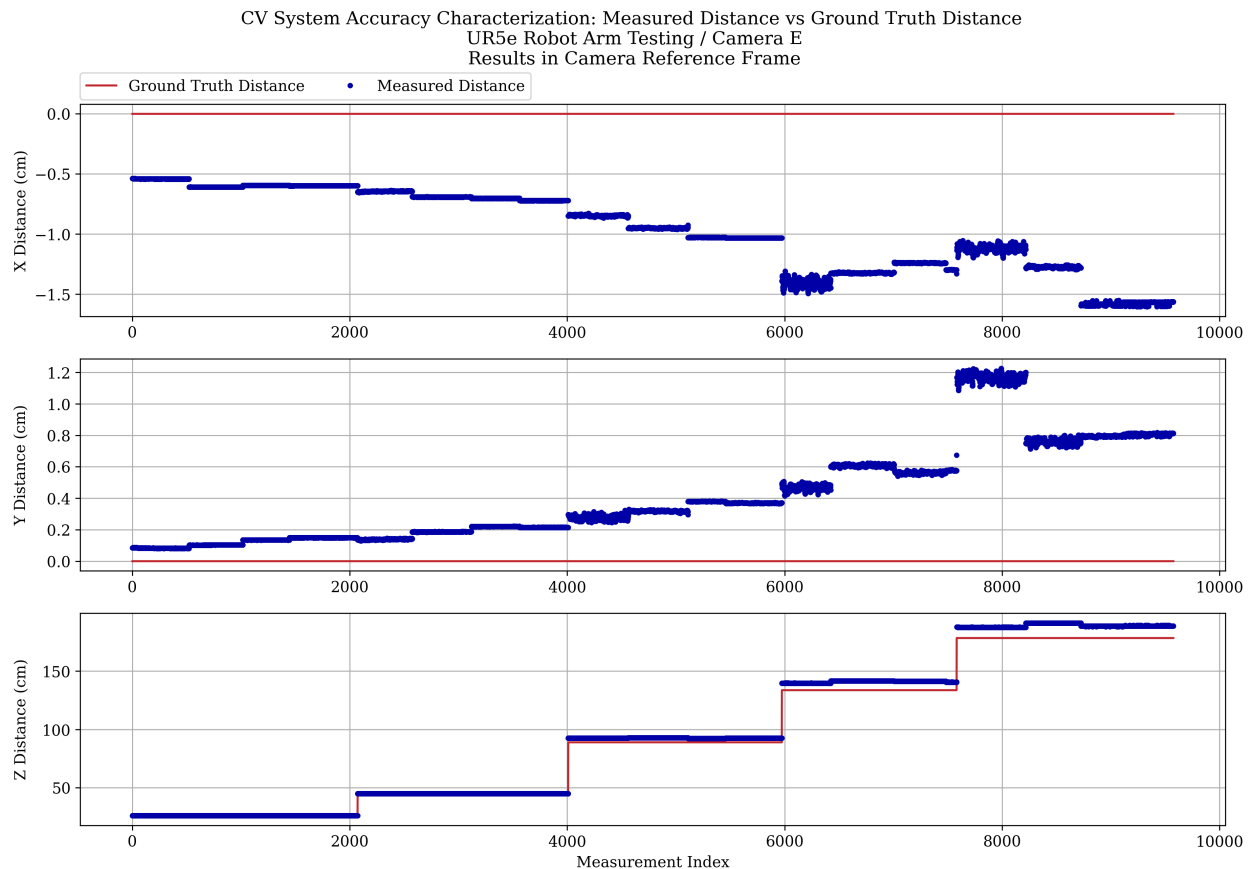


Figure 3.15: CV system ground testing: measured distance versus ground truth distance

Mean Distance Measurement Error Figure 3.16 demonstrates the relationship between the CV system’s mean distance estimation error, CubeSat testbed distance in the camera’s y axis, and CubeSat testbed orientation relative to the camera. The red, blue, green, and gray lines correspond to the 0° , 15° , 30° , and 45° orientations, respectively.

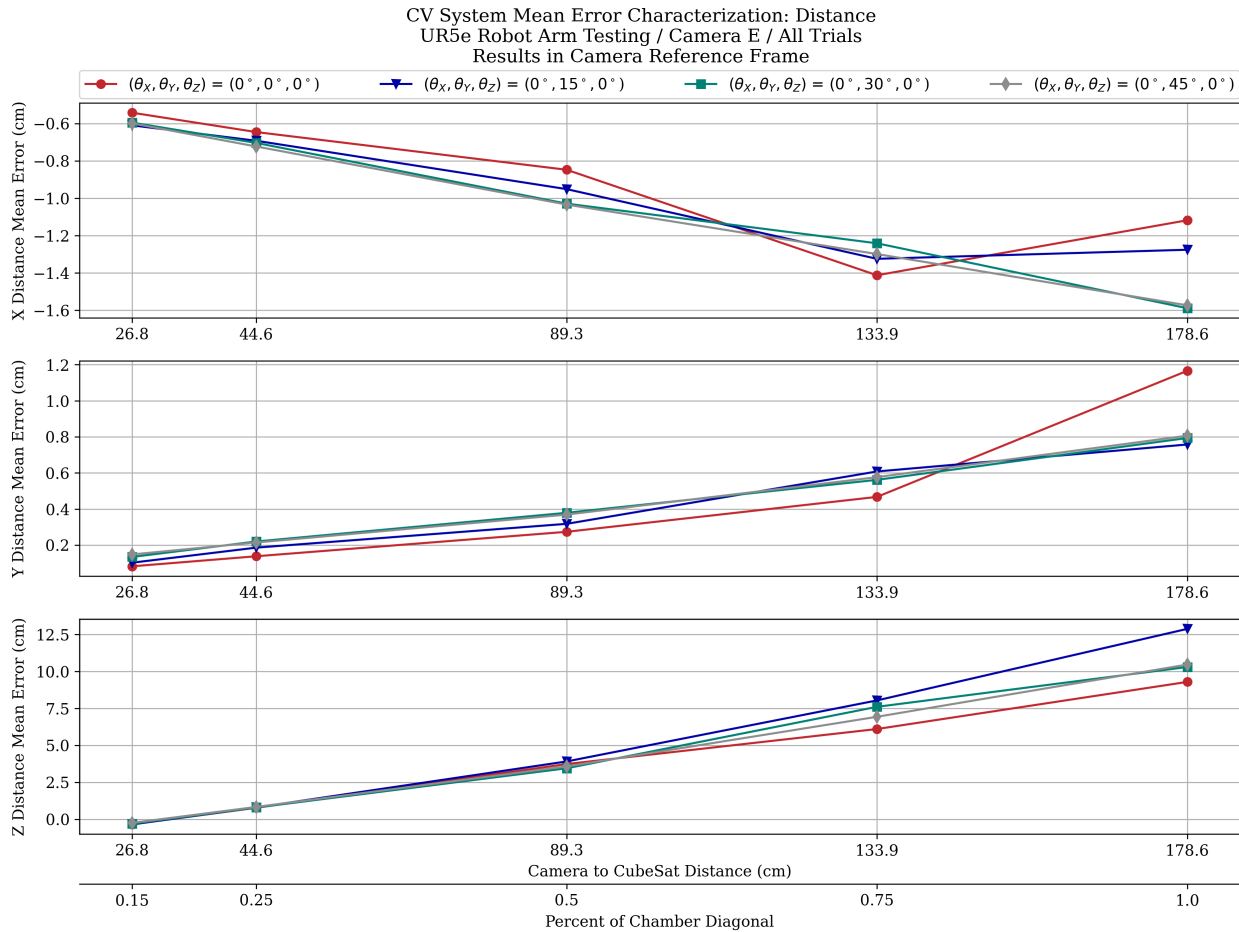


Figure 3.16: CV system ground testing: measured distance error

In the camera’s x axis, the 30° and 45° orientations demonstrated a nearly linear relationship between mean x distance error and CubeSat testbed distance to the camera. The 0° and 15° orientations both had slope discontinuities at the poses corresponding to 75% of the chamber’s distance. Mean x distance errors for every pose estimate in the experiment set were negative, indicating that the CV system had a bias in the camera’s negative x direction. The minimum and maximum mean x distance errors in the 0° orientation were -0.541 cm and -1.412 cm respectively, corresponding to 15% of the chamber’s distance and 75% of the chamber’s distance. The minimum and maximum mean x distance errors in the 15° orienta-

tion were -0.609 cm and -1.324 cm, corresponding to 15% of the chamber's distance and 75% of the chamber's distance. The minimum and maximum mean x distance errors in the 30° orientation were -0.594 cm and -1.589 cm, corresponding to 15% of the chamber's distance and 100% of the chamber's distance. The minimum and maximum mean x distance errors in the 45° orientation were -0.599 cm and -1.574 cm, corresponding to 15% of the chamber's distance and 100% of the chamber's distance.

In the camera's y axis, the 15°, 30°, and 45° orientations demonstrated a nearly linear relationship between mean y distance error and CubeSat testbed distance to the camera. The 0° orientation had a slope discontinuity at the pose corresponding to 75% of the chamber's distance. Mean y distance errors for every pose estimate in the experiment set were positive, indicating that the CV system had a bias in the camera's positive y direction. The minimum and maximum mean y distance errors in the 0° orientation were 0.083 cm and 1.166 cm respectively, corresponding to 15% of the chamber's distance and 100% of the chamber's distance. The minimum and maximum mean y distance errors in the 15° orientation were 0.103 cm and 0.758 cm, corresponding to 15% of the chamber's distance and 100% of the chamber's distance. The minimum and maximum mean y distance errors in the 30° orientation were 0.135 cm and 0.794 cm, corresponding to 15% of the chamber's distance and 100% of the chamber's distance. The minimum and maximum mean y distance errors in the 45° orientation were 0.149 cm and 0.807 cm, corresponding to 15% of the chamber's distance and 100% of the chamber's distance.

In the camera's z axis, all orientations demonstrated a nearly linear relationship between mean z distance error and CubeSat testbed distance to the camera, with the 0° orientation having a subtle slope discontinuity at 50% of the chamber's diagonal. Mean z distance errors for every pose estimate in the experiment set were positive, except at the poses corresponding to 15% of the chamber's diagonal. The minimum and maximum mean z distance errors in the 0° orientation were -0.328 cm and 9.291 cm respectively, corresponding to 15% of the chamber's distance and 100% of the chamber's distance. The minimum and maximum mean z distance errors in the 15° orientation were -0.336 cm and 12.875 cm, corresponding to 15% of the chamber's distance and 100% of the chamber's distance. The minimum and maximum mean z distance errors in the 30° orientation were -0.290 cm and 10.298 cm, corresponding

to 15% of the chamber’s distance and 100% of the chamber’s distance. The minimum and maximum mean z distance errors in the 45° orientation were -0.234 cm and 10.463 cm, corresponding to 15% of the chamber’s distance and 100% of the chamber’s distance.

Distance Measurement Noise The CV system distance measurement noise was observed to be approximately Gaussian across most poses in the experiment set. For example, Figure 3.17 below demonstrates the histograms and Gaussian fits for the x, y, and z distance measurements in all tested orientations at 25% of the chamber’s diagonal.

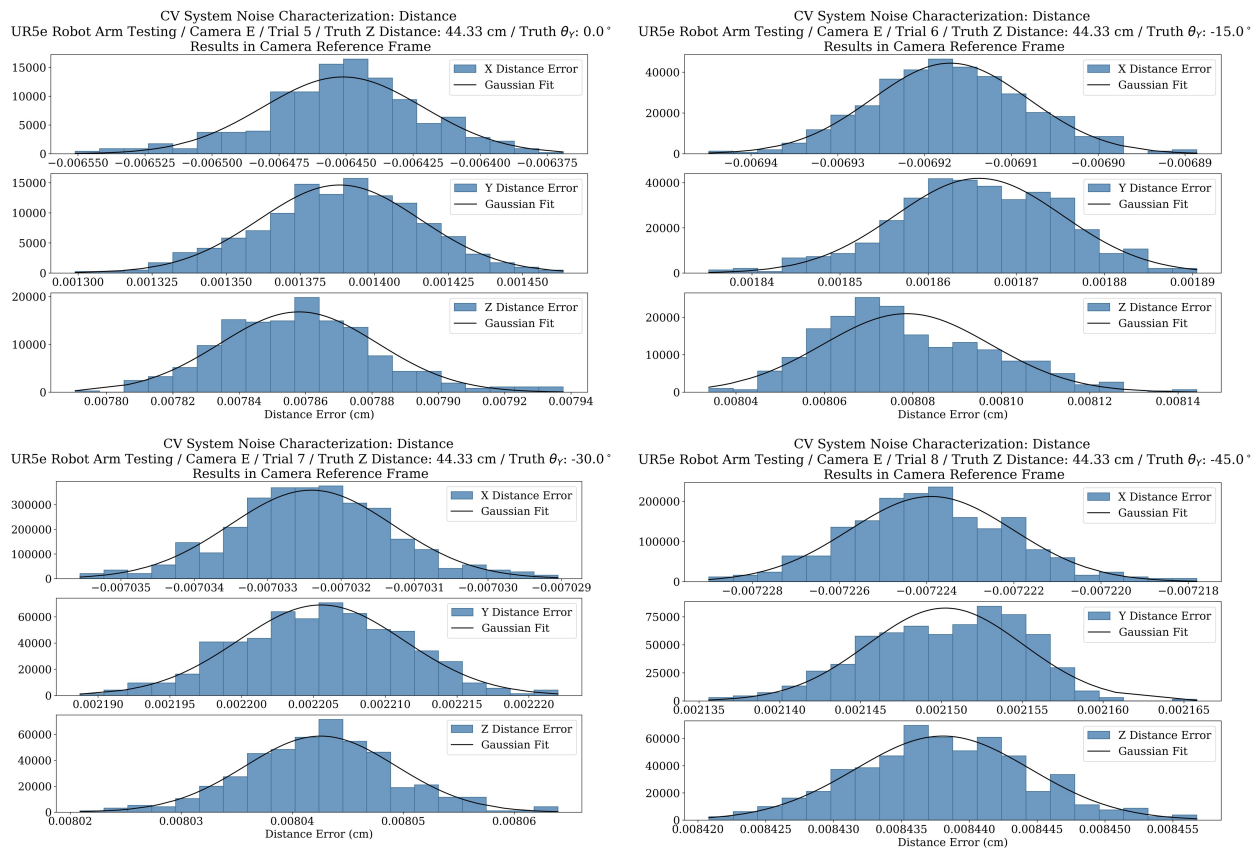


Figure 3.17: CV system ground testing: distance measurement noise at 25% of the chamber’s diagonal

Distance Results Summary All mean distance error and standard deviation values are listed below in Table 3.15 below for the experiment set. In each column, the lowest absolute value is highlighted in green and the highest absolute value is highlighted in red. Each of the X, Y, and Z axes experienced their minimum mean distance error at 15% of the chamber’s diagonal and their maximum mean distance error at 100% of the chamber diagonal. The minimum X standard deviation was observed at 15% of the chamber’s diagonal, while the

minimum Y and Z standard deviations were observed at 25% of the chamber's diagonal. The maximum X, Y, and Z standard deviations were observed at 75%, 50%, and 100% of the chamber's diagonal, respectively. In general, the distance error results followed a linear trend in all axes until approximately 75% of the chamber's diagonal; thus, in this range, the distance error could be approximated and corrected for when post-processing the CV data from parabolic flights.

Table 3.15: CV system distance accuracy and standard deviation results (green = lowest absolute value, red = highest absolute value)

Ground Truth Pose		Mean Distance Error (cm)			Standard Deviation (cm)		
Distance (cm)	Rotation	X	Y	Z	X	Y	Z
15% Chamber Diagonal: 26.785 cm	(0°, 0°, 0°)	-0.541	0.083	-0.328	0.001	0.001	0.002
	(0°, 15°, 0°)	-0.609	0.103	-0.336	0.000	0.001	0.002
	(0°, 30°, 0°)	-0.594	0.135	-0.290	0.000	0.000	0.001
	(0°, 45°, 0°)	-0.599	0.149	-0.234	0.000	0.000	0.001
25% Chamber Diagonal: 44.641 cm	(0°, 0°, 0°)	-0.645	0.139	0.786	0.003	0.003	0.002
	(0°, 15°, 0°)	-0.692	0.187	0.808	0.001	0.001	0.002
	(0°, 30°, 0°)	-0.703	0.221	0.804	0.000	0.001	0.001
	(0°, 45°, 0°)	-0.722	0.215	0.844	0.000	0.000	0.001
50% Chamber Diagonal: 89.282 cm	(0°, 0°, 0°)	-0.847	0.274	3.741	0.005	0.013	0.005
	(0°, 15°, 0°)	-0.951	0.318	3.917	0.004	0.004	0.013
	(0°, 30°, 0°)	-1.029	0.379	3.455	0.001	0.001	0.003
	(0°, 45°, 0°)	-1.034	0.369	3.580	0.000	0.001	0.002
75% Chamber Diagonal: 133.924 cm	(0°, 0°, 0°)	-1.412	0.468	6.108	0.033	0.015	0.020
	(0°, 15°, 0°)	-1.324	0.608	8.040	0.003	0.006	0.019
	(0°, 30°, 0°)	-1.241	0.562	7.608	0.002	0.007	0.018
	(0°, 45°, 0°)	-1.299	0.577	6.934	0.003	0.010	0.041
100% Chamber Diagonal: 178.565 cm	(0°, 0°, 0°)	-1.118	1.166	9.291	0.024	0.023	0.044
	(0°, 15°, 0°)	-1.276	0.758	12.875	0.007	0.017	0.030
	(0°, 30°, 0°)	-1.589	0.794	10.298	0.009	0.003	0.107
	(0°, 45°, 0°)	-1.574	0.807	10.463	0.014	0.006	0.167

Angle Results

Measured Angle versus Ground Truth Angle Figure 3.18 below plots the the CV system’s measured angle in the y axis versus the robot arm’s ground truth angle. It is evident that the highest angle measurement error and variation occur at the lower rotation angles, and that the lowest angle measurement error and variation occur at the higher rotation angles.

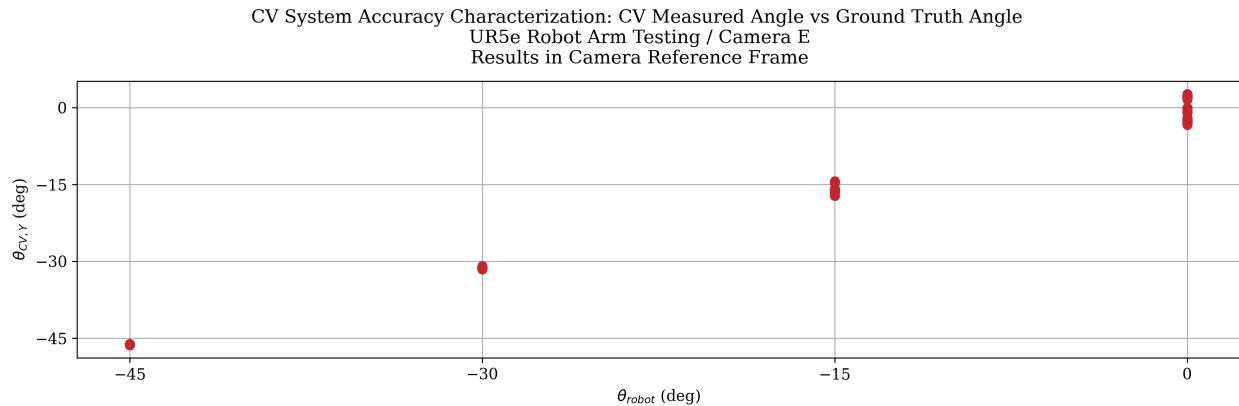


Figure 3.18: CV system ground testing: CV system measured angle vs. ground truth angle

Figure 3.19 below demonstrates the CV system’s angle measurements versus the ground truth distance (measured by the robot arm) for each pose in the experiment set. The measurement index plotted on the x axis corresponds to the total number of frames processed in the experiment, while the y axes correspond to the CubeSat testbed’s rotation about each of its axes.

During the experiment, the CubeSat testbed was rotated about its y axis, which was aligned with the camera’s y axis, to four preset rotations at each distance in the experiment set. While the CubeSat testbed was only rotated about its y axis, errors were evident in the θ_X and θ_Z values, with varying levels of noise across poses. The θ_Y measurements were shown to follow the ground truth angle values for each pose in the experiment set, with increasing error as the CubeSat testbed moved further away from the camera. This indicated that the angle estimation error in each axis was dependent on both the CubeSat testbed’s distance from the camera and on its orientation relative to the camera.

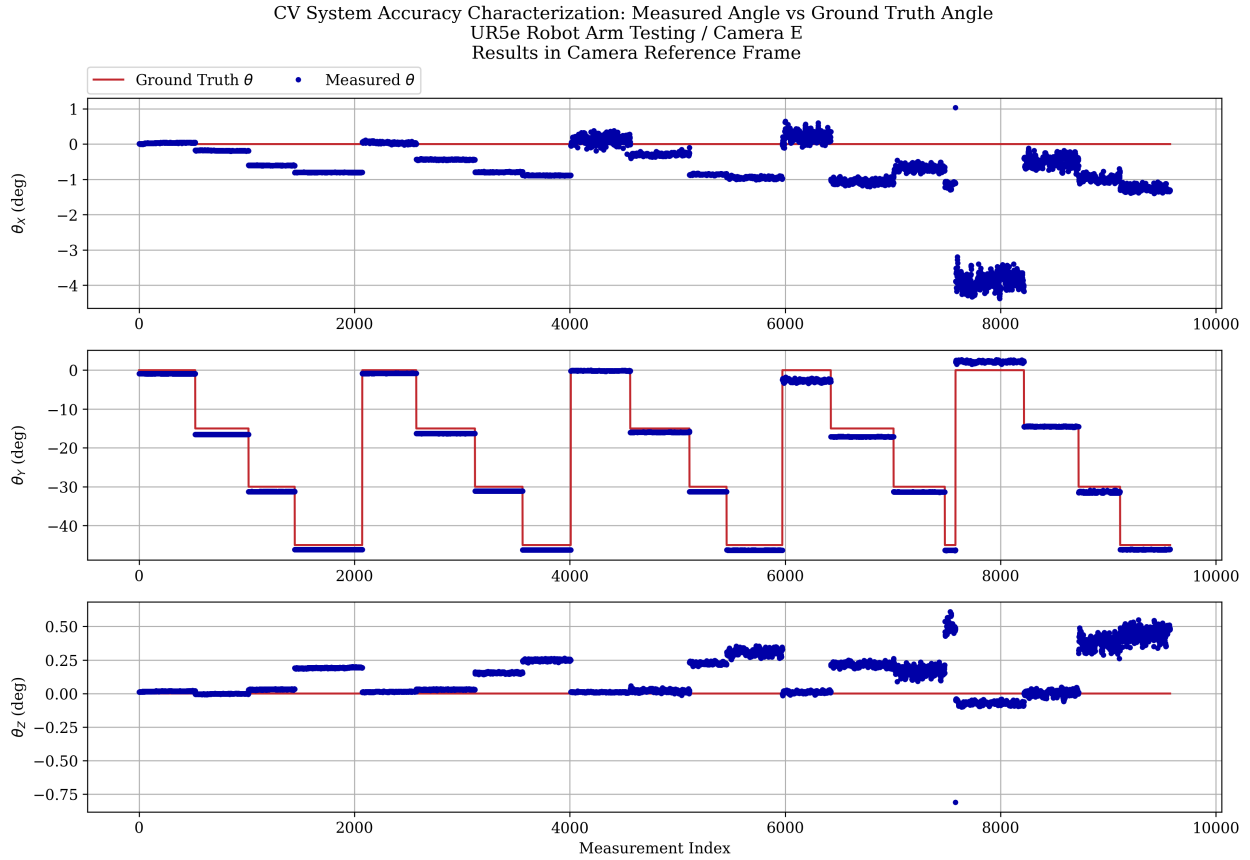


Figure 3.19: CV system ground testing: measured angle versus ground truth angle

Mean Angle Measurement Error Figure 3.20 demonstrates the relationship between the CV system's mean angle estimation error, CubeSat testbed distance in the camera's y axis, and CubeSat testbed orientation relative to the camera. The red, blue, green, and gray lines correspond to the 0° , 15° , 30° , and 45° orientations, respectively.

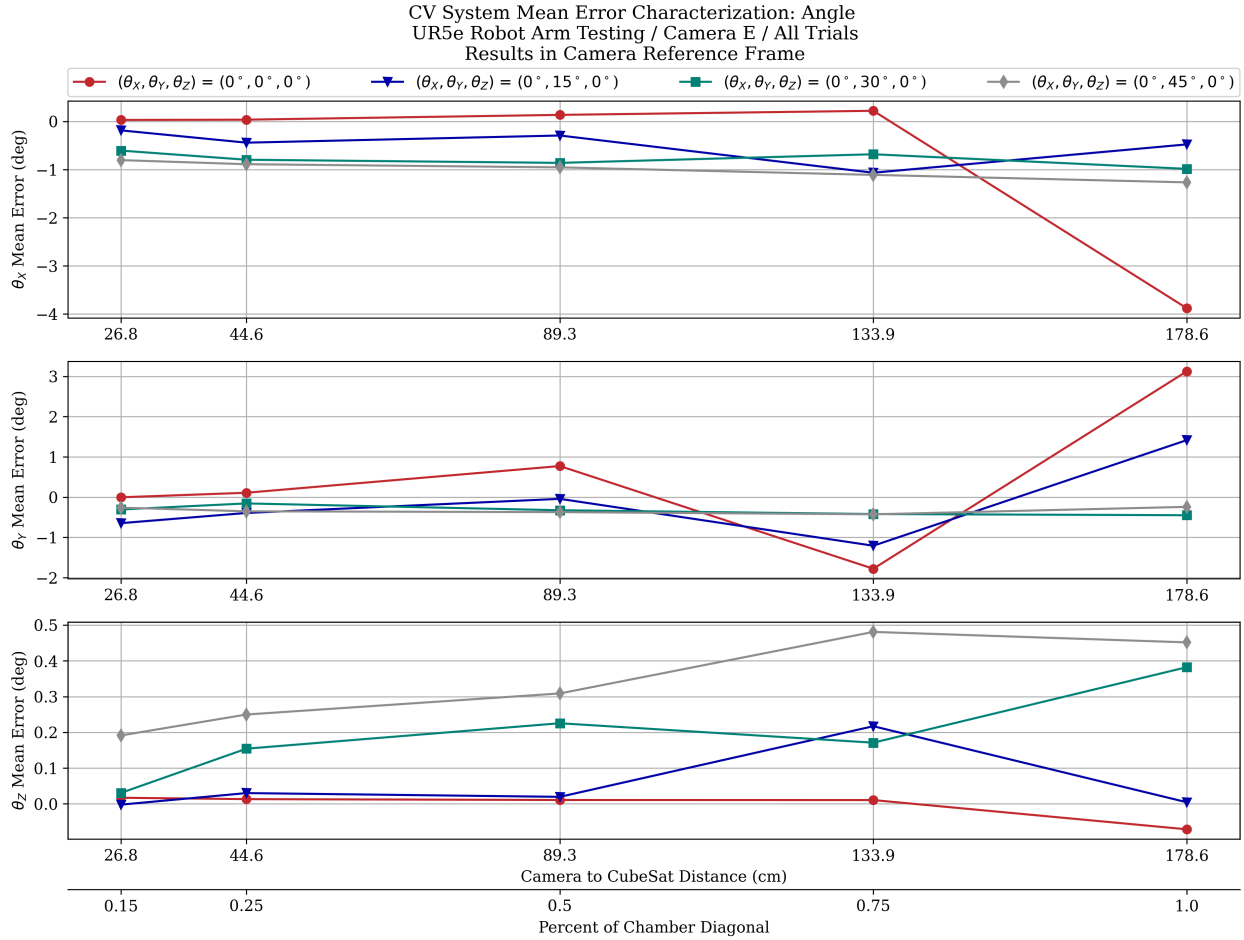


Figure 3.20: CV system ground testing: measured angle error

In the CubeSat testbed’s X axis, the 45° orientation demonstrated a nearly linear relationship between mean θ_X error and CubeSat testbed distance to the camera. The 15° orientation exhibited a slope discontinuity at 75% of the chamber’s diagonal, while the 0° and 30° orientations exhibited slope discontinuities at 75% and 100% of the chamber’s diagonal. Mean θ_X errors were all positive for the 15°, 30°, and 45° orientations, while only the final measurement error was positive for the 0° orientation. The minimum and maximum mean θ_X errors in the 0° orientation were 0.033 and -3.878°, corresponding to 15% of the chamber’s diagonal and 100% of the chamber’s diagonal. The minimum and maximum mean θ_X errors in the 15° orientation were -0.183° and -1.064°, corresponding to 15% of the chamber’s diagonal and 75% of the chamber’s diagonal. The minimum and maximum mean θ_X errors in the 30° orientation were -0.604° and -0.983°, corresponding to 15% of the chamber’s diagonal and 100% of the chamber’s diagonal. The minimum and maximum mean θ_X

errors in the 45° orientation were -0.801° and -1.264°, corresponding to 15% of the chamber’s diagonal and 100% of the chamber’s diagonal.

In the CubeSat testbed’s Y axis, the 30° and 45° orientations both demonstrated a nearly linear relationship between mean θ_Y error and CubeSat testbed distance to the camera. The 0° and 15° orientations both exhibited slope discontinuities at 50% and 75% of the chamber’s diagonal. Mean θ_Y errors were all negative for the 30° and 45° orientations, while the 0° and 15° fluctuated between positive and negative. The minimum and maximum mean θ_Y errors in the 0° orientation were -0.003° and 3.125°, corresponding to 15% of the chamber’s diagonal and 100% of the chamber’s diagonal. The minimum and maximum mean θ_Y errors in the 15° orientation were -0.041° and 1.416°, corresponding to 50% of the chamber’s diagonal and 100% of the chamber’s diagonal. The minimum and maximum mean θ_Y errors in the 30° orientation were -0.155° and -0.448°, corresponding to 25% of the chamber’s diagonal and 100% of the chamber’s diagonal. The minimum and maximum mean θ_Y errors in the 45° orientation were -0.240° and -0.426°, corresponding to 100% of the chamber’s diagonal and 75% of the chamber’s diagonal.

In the CubeSat’s testbed’s Z axis, the 15°, 30°, and 45° orientations all exhibited slope discontinuities at 75% of the chamber’s diagonal and 50% of the chamber’s diagonal. The 0° orientation also exhibited a subtle slope discontinuity at 75% of the chamber’s diagonal. Mean θ_Z errors were all positive, with the exception of the 0° and 15° orientations at 100% and 15% of the chamber’s diagonal, respectively. The minimum and maximum mean θ_Z errors in the 0° orientation were 0.011° and -0.071°, corresponding to 50% of the chamber’s diagonal and 100% of the chamber’s diagonal. The minimum and maximum mean θ_Z errors in the 15° orientation were -0.002° and 0.217°, corresponding to 15% of the chamber’s diagonal and 75% of the chamber’s diagonal. The minimum and maximum mean θ_Z errors in the 30° orientation were 0.031° and 0.382°, corresponding to 15% of the chamber’s diagonal and 100% of the chamber’s diagonal. The minimum and maximum mean θ_Z errors in the 45° orientation were 0.191° and 0.481°, corresponding to 15% of the chamber’s diagonal and 75% of the chamber’s diagonal.

Angle Measurement Noise The CV system angle measurement noise was observed to be approximately Gaussian across most poses in the experiment set. For example, Figure [3.21](#)

below demonstrates the histograms and Gaussian fits for the x, y, and z angle measurements in all tested orientations at 25% of the chamber’s diagonal.

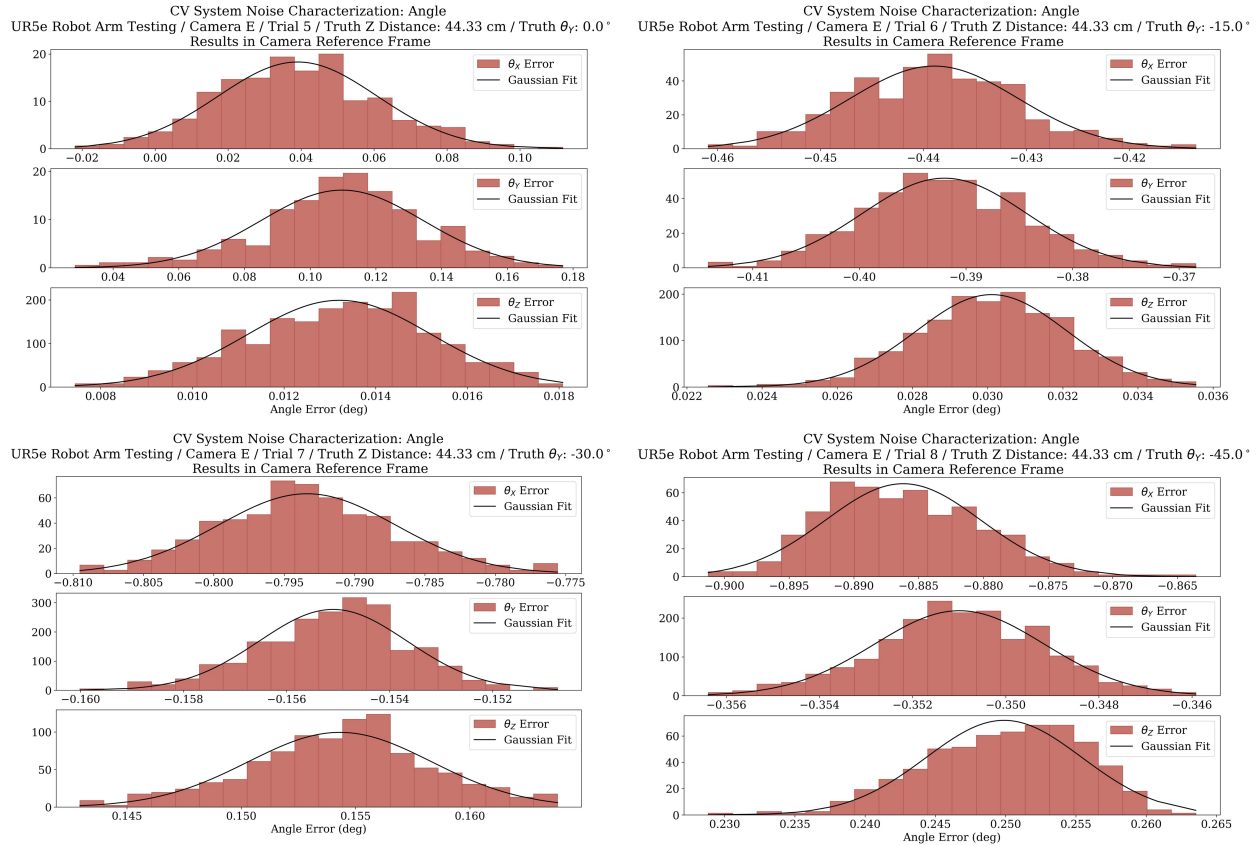


Figure 3.21: CV system ground testing: angle measurement noise at 25% of the chamber’s diagonal

Angle Results Summary All mean angle error and standard deviation values are listed below in Table 3.16 for the experiment set. In each column, the lowest absolute value is highlighted in green and the highest absolute value is highlighted in red. The θ_X and θ_Z estimates experienced their minimum mean angle error at 15% of the chamber’s diagonal, while θ_Y experienced its minimum mean angle error at 50% of the chamber’s diagonal. The θ_Y and θ_Z estimates experienced their maximum mean angle error at 75% of the chamber’s diagonal, while θ_X experienced its minimum mean angle error at 100% of the chamber’s diagonal. The θ_X and θ_Z estimates experienced their minimum standard deviation at 25% of the chamber’s diagonal, while θ_Y experienced its minimum standard deviation at 15% of the chamber’s diagonal. The θ_X , θ_Y , and θ_Z estimates experienced their maximum standard deviations at 50%, 75%, and 100% of the chamber’s diagonal, respectively. In general, the

angle error results did not follow a linear trend like the distance results, making them more difficult to estimate and correct for when post-processing the CV data from parabolic flight. Much higher angle error was observed past 75% of the chamber's diagonal; therefore, limiting the operating distance of each camera would be beneficial.

Table 3.16: CV system angle accuracy and standard deviation results (green = lowest absolute value, red = highest absolute value)

Ground Truth Pose		Mean Angle Error (deg)			Standard Deviation (deg)		
Distance (cm)	Rotation	X	Y	Z	X	Y	Z
15% Chamber Diagonal: 26.785 cm	(0°, 0°, 0°)	0.033	-0.003	0.017	0.012	0.006	0.002
	(0°, 15°, 0°)	-0.183	-0.645	-0.002	0.007	0.003	0.002
	(0°, 30°, 0°)	-0.604	-0.306	0.031	0.004	0.002	0.002
	(0°, 45°, 0°)	-0.801	-0.260	0.191	0.003	0.003	0.003
25% Chamber Diagonal: 44.641 cm	(0°, 0°, 0°)	0.039	0.110	0.013	0.022	0.025	0.002
	(0°, 15°, 0°)	-0.439	-0.392	0.030	0.008	0.008	0.002
	(0°, 30°, 0°)	-0.793	-0.155	0.154	0.006	0.001	0.004
	(0°, 45°, 0°)	-0.886	-0.351	0.250	0.006	0.002	0.006
50% Chamber Diagonal: 89.282 cm	(0°, 0°, 0°)	0.139	0.773	0.011	0.106	0.043	0.002
	(0°, 15°, 0°)	-0.290	-0.041	0.020	0.035	0.033	0.009
	(0°, 30°, 0°)	-0.859	-0.325	0.225	0.012	0.005	0.008
	(0°, 45°, 0°)	-0.952	-0.371	0.309	0.023	0.002	0.019
75% Chamber Diagonal: 133.924 cm	(0°, 0°, 0°)	0.223	-1.777	0.011	0.129	0.282	0.007
	(0°, 15°, 0°)	-1.064	-1.206	0.217	0.053	0.031	0.012
	(0°, 30°, 0°)	-0.679	-0.419	0.171	0.070	0.021	0.029
	(0°, 45°, 0°)	-1.108	-0.426	0.481	0.223	0.019	0.136
100% Chamber Diagonal: 178.565 cm	(0°, 0°, 0°)	-3.878	3.125	-0.071	0.194	0.195	0.011
	(0°, 15°, 0°)	-0.474	1.416	0.005	0.137	0.057	0.017
	(0°, 30°, 0°)	-0.983	-0.448	0.382	0.068	0.177	0.039
	(0°, 45°, 0°)	-1.264	-0.240	0.452	0.063	0.035	0.040

3.4.4 Operating Range Selection

From the results in Section 3.4.3, it was apparent that in general, increasing the distance between the CubeSat testbed and camera resulted in increased error and noise in both the distance and angle results. Since the CV system had redundant camera coverage of the chamber, as described in Section 3.3.3, the operating range for the CV system was limited to 50% of the chamber’s diagonal to minimize CV measurement error; that is, if the CubeSat testbed was within the FOV of multiple cameras, only the estimates from the cameras $\leq 50\%$ of the chamber’s diagonal away from the CubeSat testbed were considered. This eliminated many of the observed slope discontinuities and high noise poses. The ground testing mean error results are replotted below in Figure 3.22 and Figure 3.23, with the operating range set to 50% of the chamber’s diagonal.

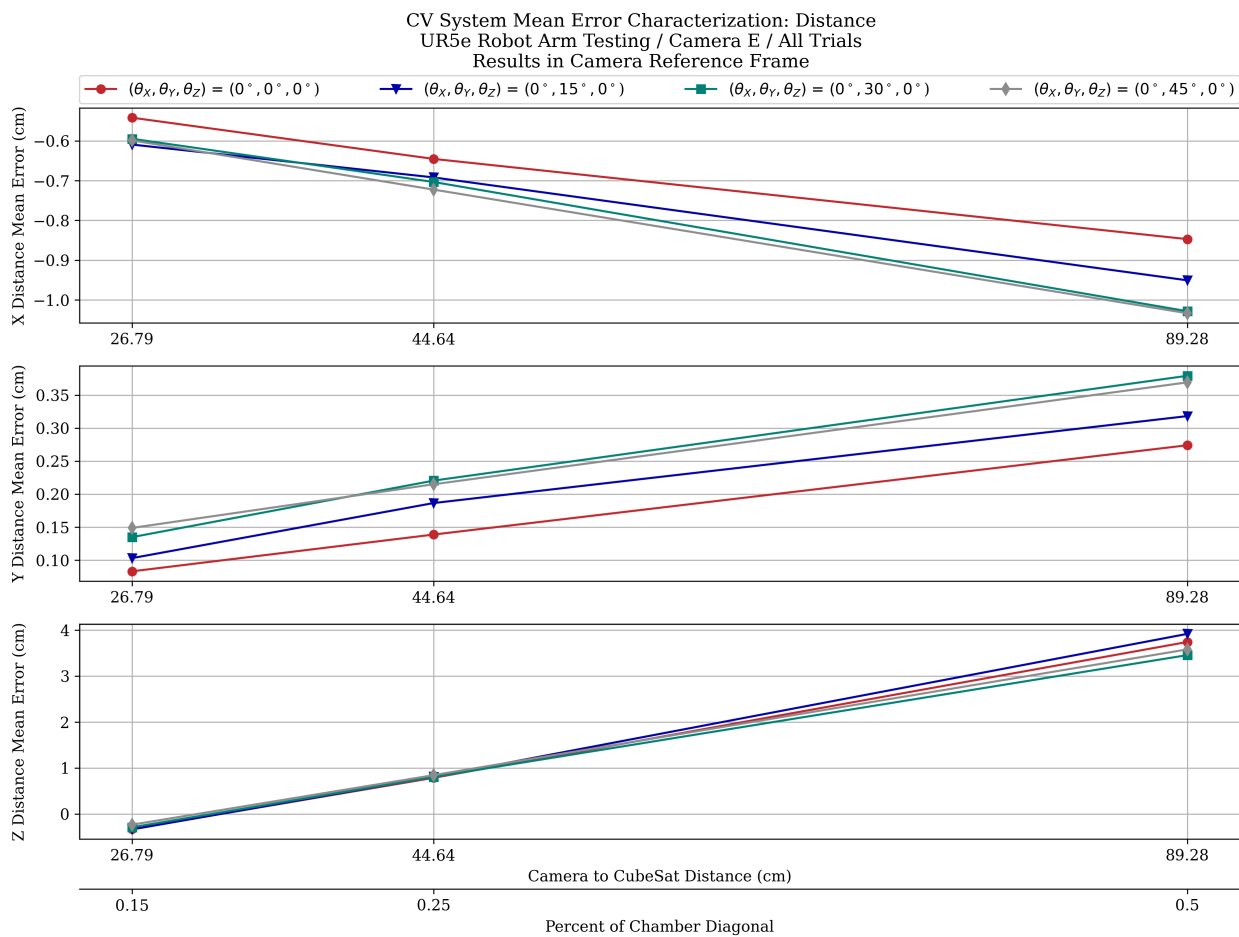


Figure 3.22: CV system ground testing: measured distance error within specified operating range

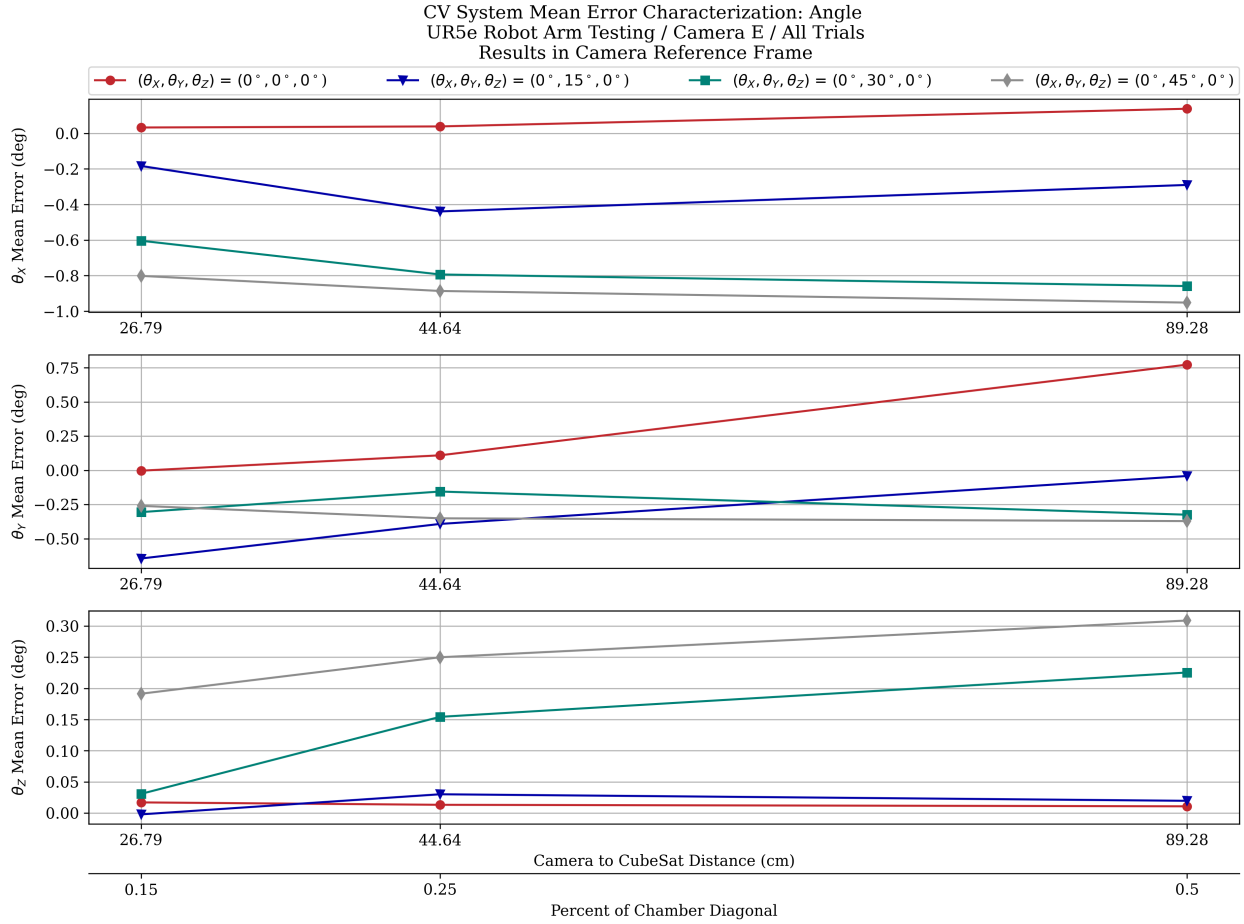


Figure 3.23: CV system ground testing: measured angle error within specified operating range

3.4.5 Ground Testing Conclusions

The purpose of ground testing was to characterize the accuracy and noise of the CV system across various poses in the chamber’s internal volume. The CubeSat testbed was mounted to a UR5e robot arm and placed in 20 different poses along the camera’s centerline, where the distance was varied from 15% of the chamber’s diagonal distance to 100% of the chamber’s diagonal distance and from 0° rotation to 45° rotation in a single axis.

The ground testing assisted in defining the maximum operating range for each camera to CubeSat testbed; in general, distance and angle errors experienced slope discontinuities, less predictable behavior, and increased measurement noise past 50% of the chamber’s diagonal distance; therefore, the maximum operating distance for any camera to a CubeSat testbed was taken as 50% of the chamber’s diagonal. Within the 50% maximum operating distance,

the maximum observed distance error was 3.917 cm (approximately 4.3% distance error) and the maximum observed angle error is 0.773 deg.

The measurement noise for both distance and angle was observed to be approximately Gaussian across all poses. This indicated that the CV system was appropriate for use as a measurement source in the EKF used for post processing Zero-G flight data. The magnitude of the noise provided insight into the tuning parameters for the EKF.

3.4.6 Ground Testing Limitations

While this testing did provide insight into the performance of the Zero-G HDD-RW CV system, there were certain limitations that must be recognized in the test setup. First, the testing only characterized the accuracy and noise of the CV system when 1-2 faces of the CubeSat testbed were visible; however, in the Zero-G flights, up to 3 faces were visible at any time. Second, the testing only characterized the accuracy and noise of the CV system when the CubeSat testbed was positioned along the centerline of the camera's FOV. During the Zero-G flights, the CubeSat testbed had full 3DOF translational freedom, and could end up in any area of the camera's FOV. The calibration parameters determined in Section 3.3.5 did account for the lens distortion; however, imperfections in the calibration procedure may have led to small variations in the CV system's accuracy and noise at different x and y locations in any camera's frame. Next, the testing was performed in a laboratory environment which did not perfectly match the aircraft environment. Differences in lighting conditions, such as brightness and color temperature, may have impacted the CV system's performance. Finally, the testing only characterized the accuracy and noise of the CubeSat testbed in static poses; however, in the Zero-G flights the CubeSat testbed could move in 6DOF. This introduced translational and rotational motion blur, making the ArUco markers more difficult to detect and yielding additional pose estimation error and noise. Given additional time, it is recommended that a more extensive set of tests is performed to address the noted limitations - especially on the effect that translational and rotational motion blur have on the performance of the system.

Chapter 4

CubeSat Testbed In-Flight Attitude Estimation and Validation

4.1 Introduction

The CubeSat testbed attitude was estimated through two different methods: 1) Internal: numerically integrating the testbed's onboard gyroscope data to propagate the attitude, and 2) External: post-processing CV system videos to perform ArUco board pose estimation. The purpose of the CV system was to validate the CubeSat testbed's onboard gyroscope-integrated attitude determination method, which would confirm that the inputs to the CubeSat testbed's attitude controller were correct during each experiment. Since the attitude determination method was the same across all experiments in all flights, this analysis focuses on a subset of trials performed within the chamber. Validation of the CubeSat testbed's onboard attitude determination method in the subset of trials validates the attitude determination method for all trials. The chapter is structured as follows: Section 4.2 describes the process to convert the CV pose estimates into an inertial reference frame, Section 4.3.4 characterizes the noise and uncertainty in each of the sensors used for attitude estimation, Section 4.3 combines the data from the CubeSat testbed's onboard attitude estimates and the CV system's attitude estimates into an Extended Kalman Filter (EKF), Section 4.4 describes the conclusions drawn from the EKF results, and Section 4.5 describes the limitations of the EKF.

4.2 Reference Frame Conversion

4.2.1 Introduction

Comparing and combining the CV system attitude estimates with the CubeSat testbed’s onboard attitude estimates first required transforming all of the data into the same reference frame. All CV data was first provided in each camera’s individual reference frame. The cameras were attached to the chamber which was attached to the aircraft floor; therefore, the cameras and camera IMUs were all rotating with the aircraft and their readings were not in an inertial reference frame. The CubeSat testbed was in free-fall as it freely floated within the aircraft cabin; the testbed was both rotating and accelerating, so its body frame was also not considered inertial. The reference frame from which all data was analyzed was defined as the very first pose of the CubeSat testbed in each trial, where the initial attitude was taken as the identity quaternion (0 degrees rotation in all axes); this frame was fixed in space, not falling or rotating with the CubeSat, so it was considered an inertial frame.

The CubeSat testbed could be detected by multiple cameras at once while in the chamber experiment, due to the redundant volumetric coverage described in Section 3.3.3. First, the CV pose estimates from each camera were converted into the chamber’s reference frame. This was used as an intermediate frame to compare the CV data from each camera, and to visualize the motion of the CubeSat within the chamber. The CV data was then converted to the inertial reference frame by accounting for the aircraft’s rotation (as measured by the chamber IMUs) since the beginning of the experiment trial.

4.2.2 Cameras A-D to Chamber Reference Frame Conversion

The chamber reference frame was attached to the bottom of the chamber, with the z axis pointing upwards and the y axis pointing towards the front of the aircraft, as shown below in Figure 4.1. Each camera’s coordinate system was offset from the chamber’s coordinate system in both rotation and translation. First, the pose estimates were rotated to be aligned with the chamber’s coordinate system. Next, distance estimates were translated to account for the offset between the camera’s origin and the chamber’s origin. The resulting rotation matrices and translation offsets are shown for each camera below in Table 4.1. Five CubeSat testbed trials from Flight 6 are then presented in the following section to validate the CV

system data conversion into the chamber reference frame.

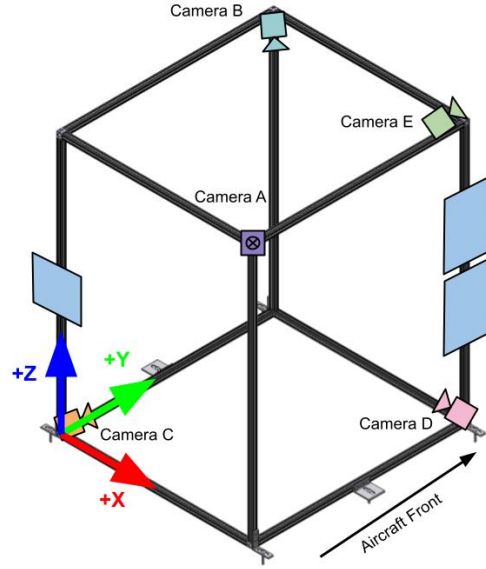


Figure 4.1: Chamber Coordinate System Definition

Table 4.1: Cameras A-D to Chamber Reference Frame Conversion

Camera	Rotation Matrix	Translation Offset (m)		
		X	Y	Z
A	$R_{chamber,camA} = \begin{bmatrix} 0.7071 & 0.5 & -0.5 \\ 0.7071 & -0.5 & 0.5 \\ 0 & -0.7071 & -0.7071 \end{bmatrix}$	0.8378	0.0258	1.1516
B	$R_{chamber,camB} = \begin{bmatrix} -0.7071 & -0.5 & 0.5 \\ -0.7071 & 0.5 & -0.5 \\ 0 & -0.7071 & -0.7071 \end{bmatrix}$	0.0258	0.9521	1.1516
C	$R_{chamber,camC} = \begin{bmatrix} 0.7071 & 0.5 & 0.5 \\ -0.7071 & 0.5 & 0.5 \\ 0 & -0.7071 & 0.7071 \end{bmatrix}$	0.0258	0.0258	0.0676
D	$R_{chamber,camD} = \begin{bmatrix} -0.7071 & -0.5 & -0.5 \\ 0.7071 & -0.5 & -0.5 \\ 0 & -0.7071 & 0.7071 \end{bmatrix}$	0.8378	0.9521	0.0676

Validation of Camera A-D Data in Chamber Reference Frame (Flight 6)

Trial 1, presented in Figures 4.2 and 4.3, demonstrated the use of all four chamber experiment cameras to estimate the testbed pose. ArUco detection failed for each of the cameras between 3 and 6 seconds due to quick translation of the testbed, which caused high motion blur in the videos. Nonetheless, the successful pose estimates overlapped in both position and attitude for all four cameras, indicating that the data conversion into the chamber reference frame was successful for all cameras.

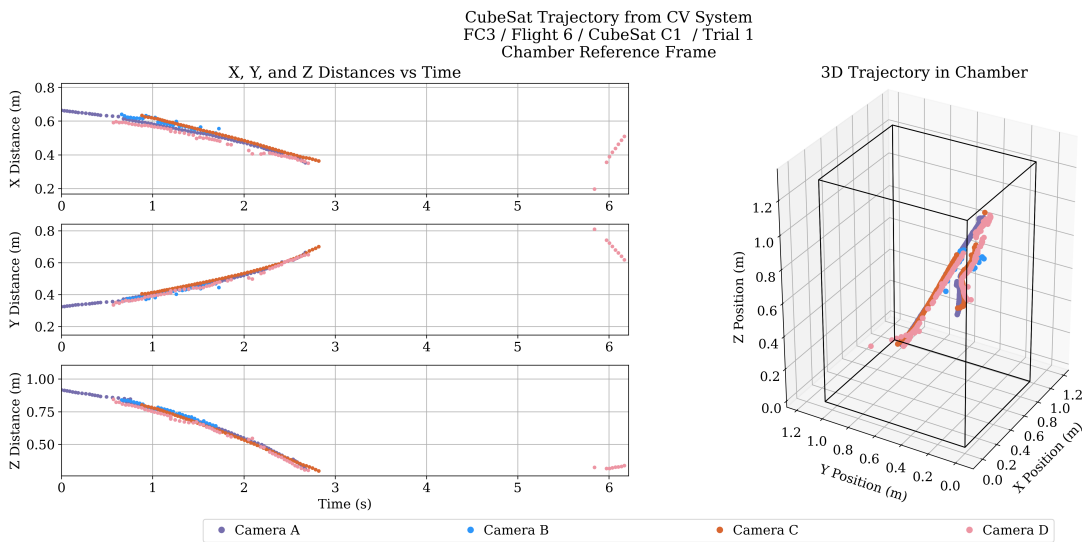


Figure 4.2: CubeSat testbed trajectory in the chamber reference frame estimated from cameras A-D: Flight 6, CubeSat C1, Trial 1)

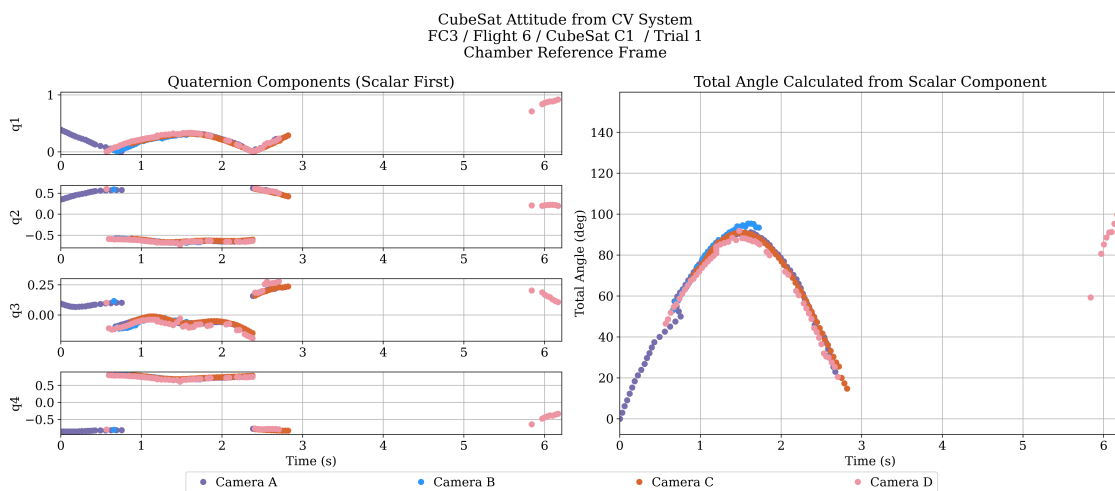


Figure 4.3: CubeSat testbed attitude in the chamber reference frame estimated from cameras A-D: Flight 6, CubeSat C1, Trial 1)

Trial 5, presented in Figures 4.4 and 4.5, demonstrated the use of Cameras A and D (Cameras B and C failed to detect the testbed). The initial Camera D measurements were noisier because the testbed was positioned at the top of the chamber; it floated downwards closer to Camera D over the trial, resulting in more stable and accurate pose estimates from the camera later in the trial. ArUco detection failed for both cameras between 4-5 seconds due to motion blur. The pose estimates overlapped in position and attitude for both cameras indicating that the data conversion into the chamber reference frame was successful.

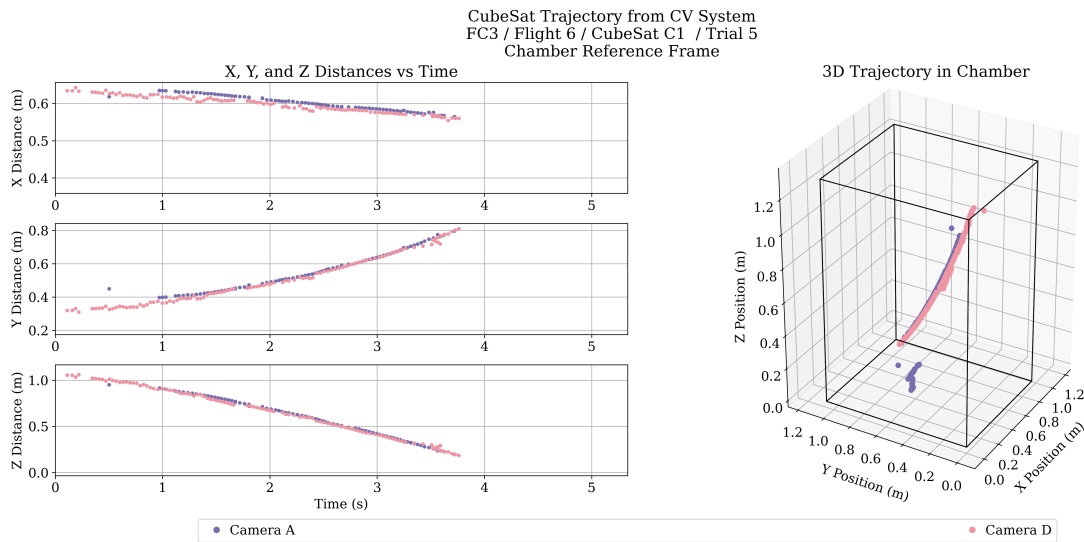


Figure 4.4: CubeSat testbed attitude in the chamber reference frame estimated from cameras A-D: Flight 6, CubeSat C1, Trial 5)

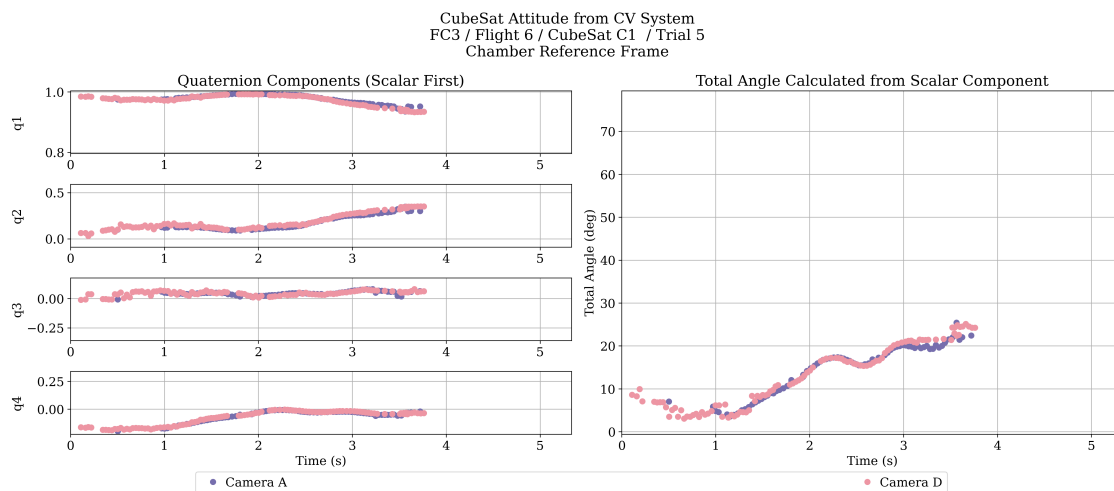


Figure 4.5: CubeSat testbed trajectory in the chamber reference frame estimated from cameras A-D: Flight 6, CubeSat C1, Trial 5)

Trial 7, presented in Figures 4.6 and 4.7, demonstrated the use of Cameras C and D to estimate the testbed pose (Cameras A and B failed to detect the testbed). Camera D experienced high measurement noise for most of the trial, and therefore was trusted less than Camera C for this trial. The pose estimates overlapped in both position and attitude for both cameras, indicating that the data conversion into the chamber reference frame was successful.

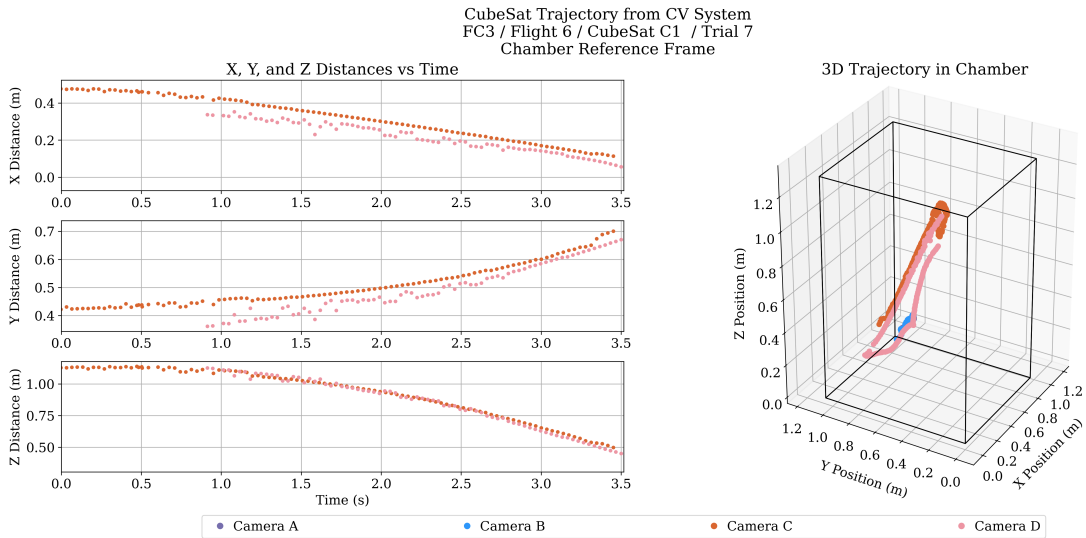


Figure 4.6: CubeSat testbed attitude in the chamber reference frame estimated from cameras A-D: Flight 6, CubeSat C1, Trial 7)

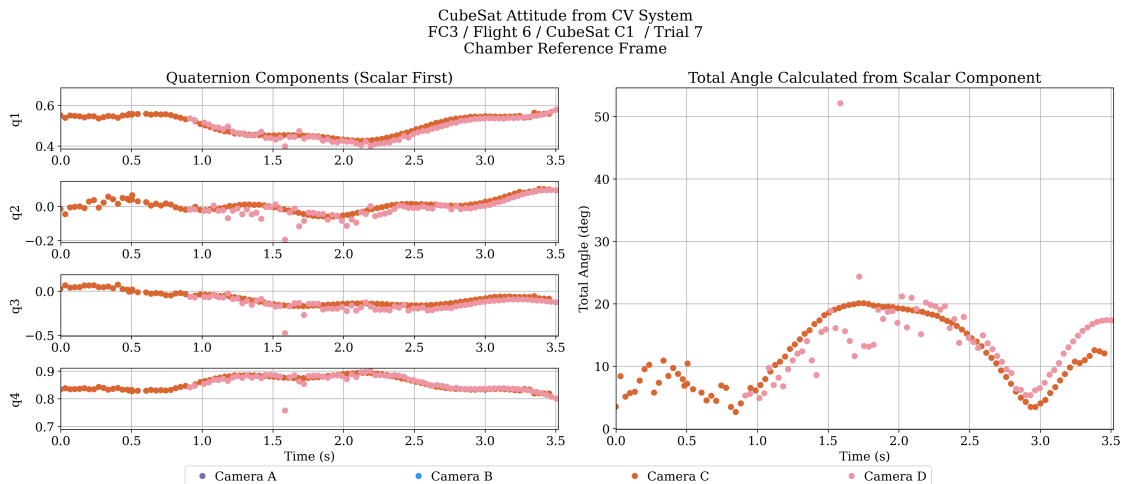


Figure 4.7: CubeSat testbed trajectory in the chamber reference frame estimated from cameras A-D: Flight 6, CubeSat C1, Trial 7)

Trial 8, presented in Figures 4.8 and 4.9, demonstrated the use of Cameras C and D to estimate the testbed pose (Cameras A and B failed to detect the testbed). Camera D experienced high measurement noise for the first half of the trial, and therefore was trusted less than Camera C in this range. ArUco detection failed for both of the cameras between 3 and 4 seconds due to quick translation of the testbed, which caused high motion blur in the videos. The pose estimates overlapped in both position and attitude for both cameras, despite the high noise in Camera D, indicating that the data conversion into the chamber reference frame was successful for both cameras.

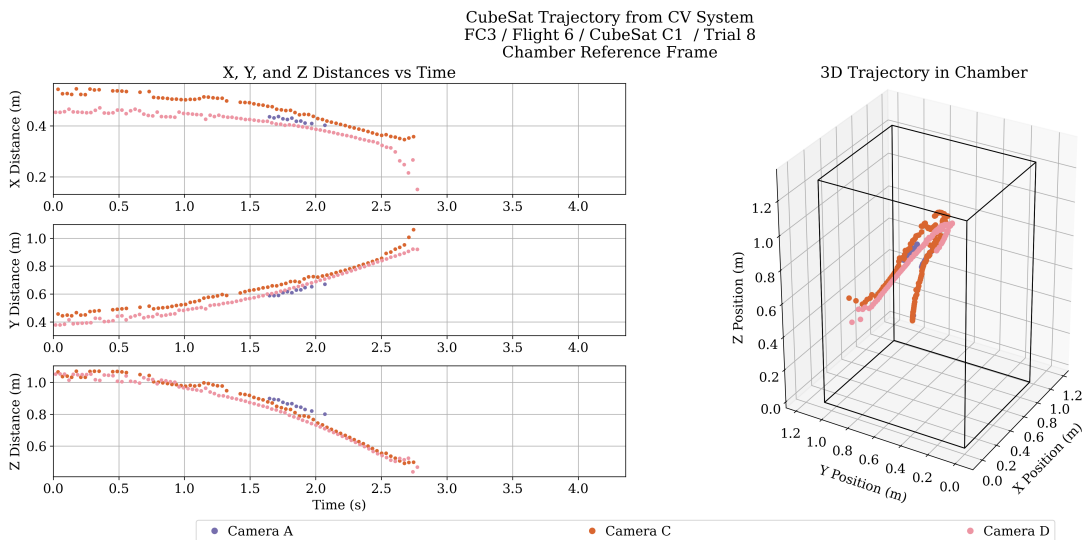


Figure 4.8: CubeSat testbed attitude in the chamber reference frame estimated from cameras A-D: Flight 6, CubeSat C1, Trial 8)

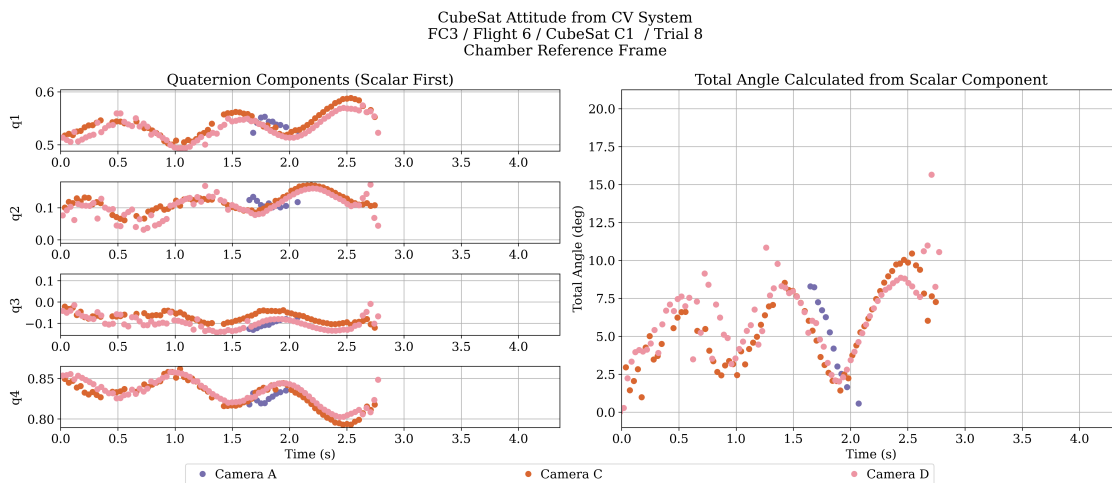


Figure 4.9: CubeSat testbed trajectory in the chamber reference frame estimated from cameras A-D: Flight 6, CubeSat C1, Trial 8)

Trial 10, presented in Figures 4.10 and 4.11, demonstrated the use of Cameras A and D to estimate the testbed pose (Cameras B and C failed to detect the testbed). The testbed was out of view of Camera D for the first half of the trial, but was captured by Camera A in this range. ArUco detection failed for both of the cameras after 3 seconds due to quick translation of the testbed, which caused high motion blur in the videos. The pose estimates overlapped in both position and attitude for both cameras, indicating that the data conversion into the chamber reference frame was successful.

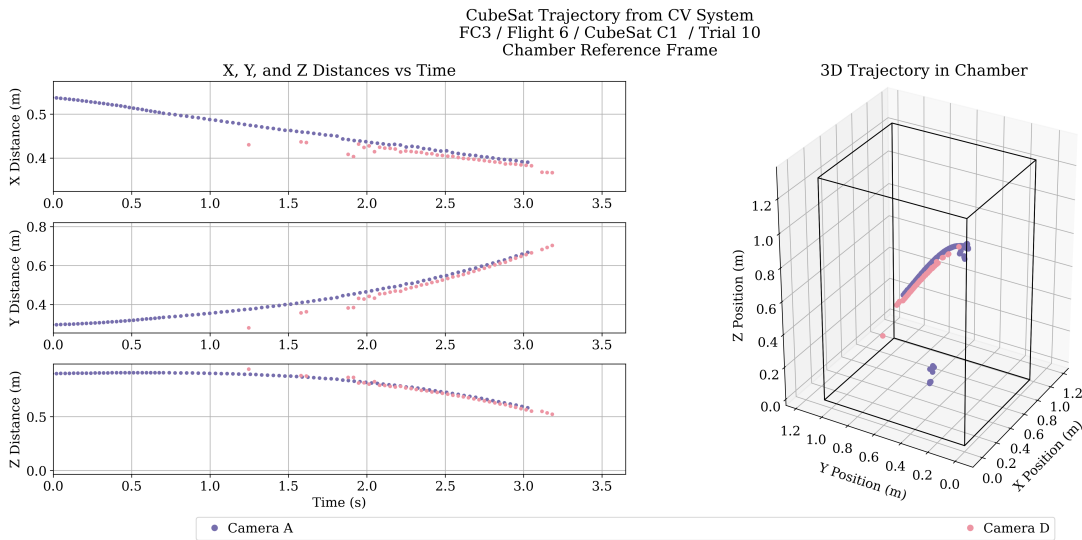


Figure 4.10: CubeSat testbed attitude in the chamber reference frame estimated from cameras A-D: Flight 6, CubeSat C1, Trial 10)

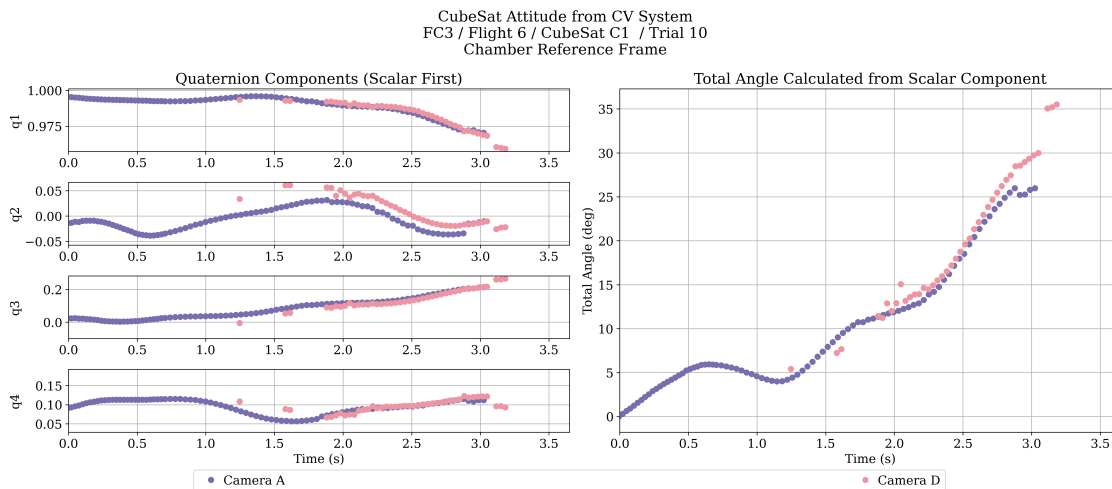


Figure 4.11: CubeSat testbed trajectory in the chamber reference frame estimated from cameras A-D: Flight 6, CubeSat C1, Trial 10)

4.2.3 Chamber IMUs Reference Frames Definitions

IMUs A-D were mounted on the Camera A-D assemblies, respectively. First, the rotation matrix $R_{cam,imu}$ was defined to rotate each IMU's measurements into the corresponding camera's reference frame. Next, the previously defined $R_{chamber,cam}$ matrices, which rotate the CV system measurements into the chamber reference frame, were multiplied with $R_{cam,imu}$ to achieve $R_{chamber,imu}$. This rotation matrix defined the transformation between the IMU reference frame and the chamber reference frame. Table 4.2 below lists the resulting $R_{cam,imu}$ and $R_{chamber,imu}$ matrices.

Table 4.2: Camera IMUs A-D to Chamber Reference Frame Conversion

IMU	Rotation Matrix: IMU to Camera	Rotation Matrix: IMU to Chamber
A	$R_{camA,imuA} = \begin{bmatrix} -1 & 0 & 0 \\ 0 & -0.7071 & 0.7071 \\ 0 & 0.7071 & 0.7071 \end{bmatrix}$	$R_{chamber,imuA} = \begin{bmatrix} 0.7071 & 0 & -0.7071 \\ -0.7071 & 0 & -0.7071 \\ 0 & 1 & 0 \end{bmatrix}$
B	$R_{camB,imuB} = \begin{bmatrix} -1 & 0 & 0 \\ 0 & -0.7071 & 0.7071 \\ 0 & 0.7071 & 0.7071 \end{bmatrix}$	$R_{chamber,imuB} = \begin{bmatrix} 0.7071 & 0 & -0.7071 \\ -0.7071 & 0 & -0.7071 \\ 0 & 1 & 0 \end{bmatrix}$
C	$R_{camC,imuC} = \begin{bmatrix} 1 & 0 & 0 \\ 0 & 0.7071 & -0.7071 \\ 0 & 0.7071 & 0.7071 \end{bmatrix}$	$R_{chamber,imuC} = \begin{bmatrix} -0.7071 & -0.7071 & 0 \\ 0.7071 & -0.7071 & 0 \\ 0 & 0 & 1 \end{bmatrix}$
D	$R_{camD,imuD} = \begin{bmatrix} 1 & 0 & 0 \\ 0 & 0.7071 & -0.7071 \\ 0 & 0.7071 & 0.7071 \end{bmatrix}$	$R_{chamber,imuD} = \begin{bmatrix} -0.7071 & -0.7071 & 0 \\ 0.7071 & -0.7071 & 0 \\ 0 & 0 & 1 \end{bmatrix}$

Validation of IMU D Data in Chamber Reference Frame (Flight 6)

The chamber gyroscope and accelerometer readings were converted into the chamber reference frame for the same trials studied in Section 4.2.2, and the results are shown below in Figures 4.12 - 4.16. Only the IMU attached to Camera D was used to represent the aircraft's dynamics; IMU characterization in Section 4.3.4 found significant nonlinear drift and high bias in IMUs A-C. The positive x-axis of the gyroscope was approximately aligned

with the aircraft's right wing, and measured a rotation rate of -2 deg/s to -4 deg/s for each trial, which was in the expected aircraft rotation rate range during a zero-g parabola [7]. The accelerometer recorded near-zero g levels in each axis for all trials, as expected.

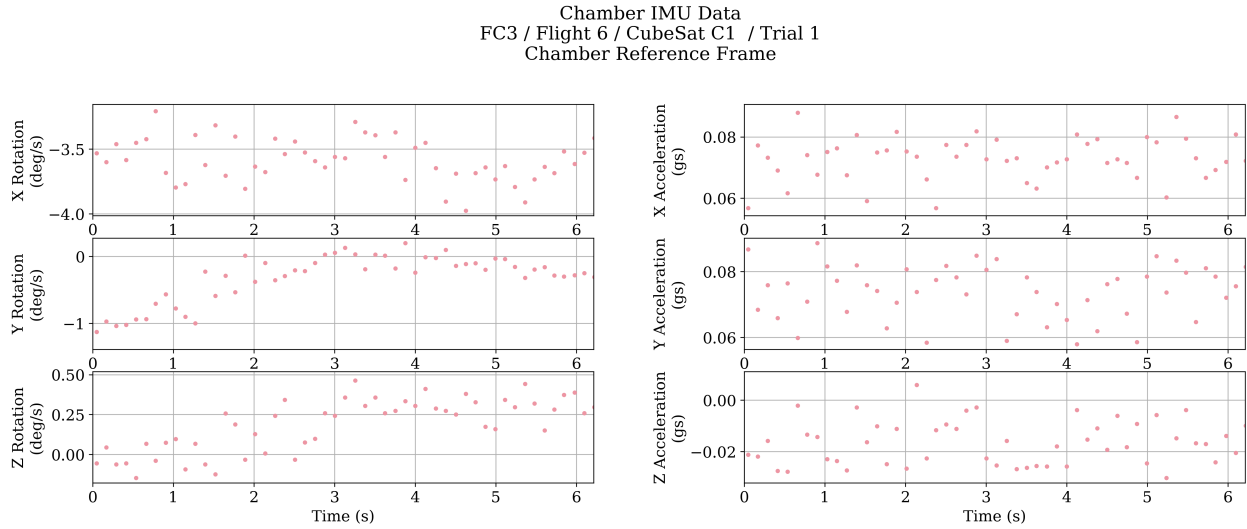


Figure 4.12: IMU D Rotation and Acceleration Rates in the Chamber Reference Frame: Flight 6, CubeSat C1, Trial 1)

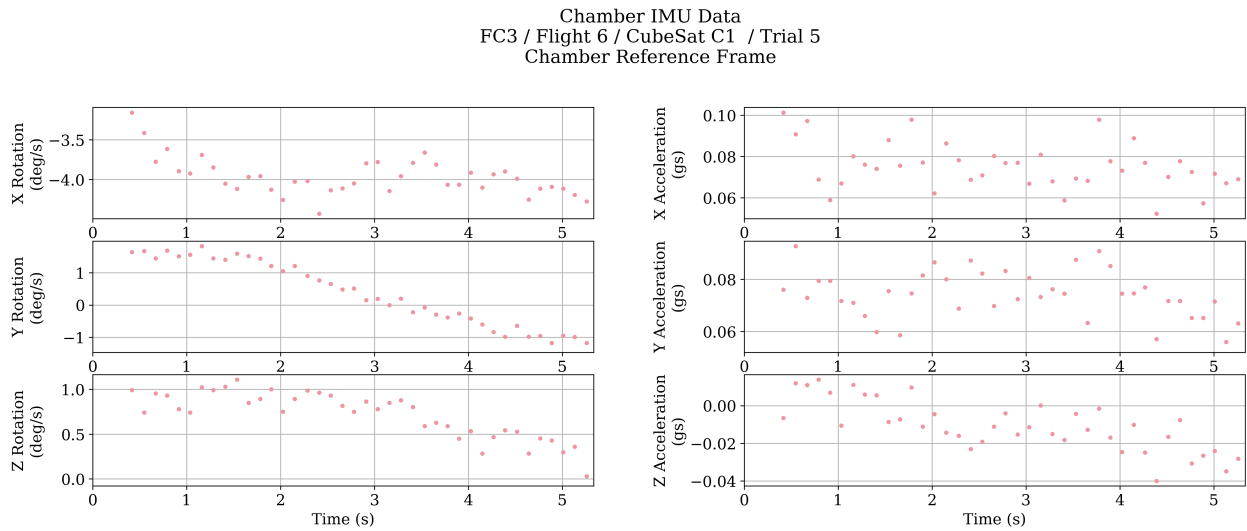


Figure 4.13: IMU D Rotation and Acceleration Rates in the Chamber Reference Frame: Flight 6, CubeSat C1, Trial 5)

Chamber IMU Data
 FC3 / Flight 6 / CubeSat C1 / Trial 7
 Chamber Reference Frame

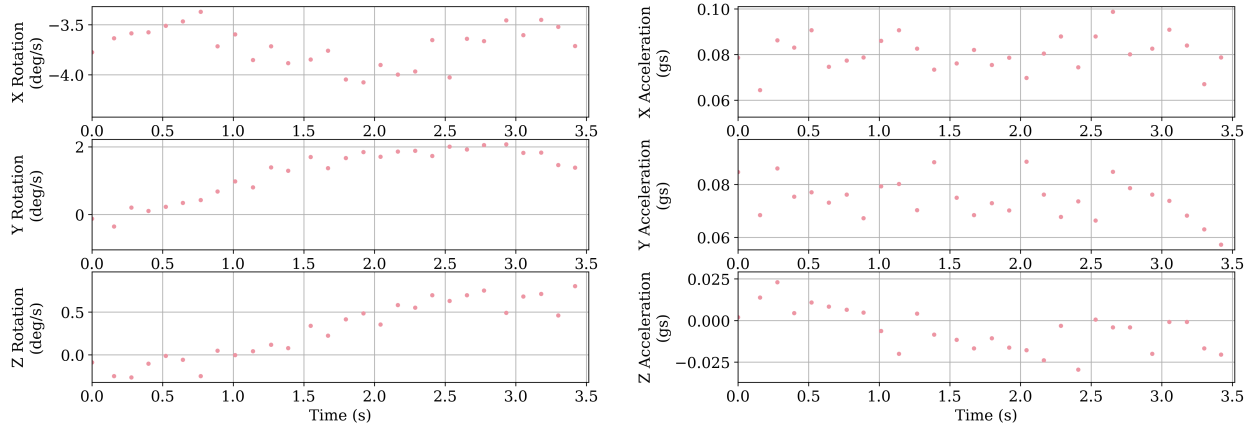


Figure 4.14: IMU D Rotation and Acceleration Rates in the Chamber Reference Frame: Flight 6, CubeSat C1, Trial 7)

Chamber IMU Data
 FC3 / Flight 6 / CubeSat C1 / Trial 8
 Chamber Reference Frame

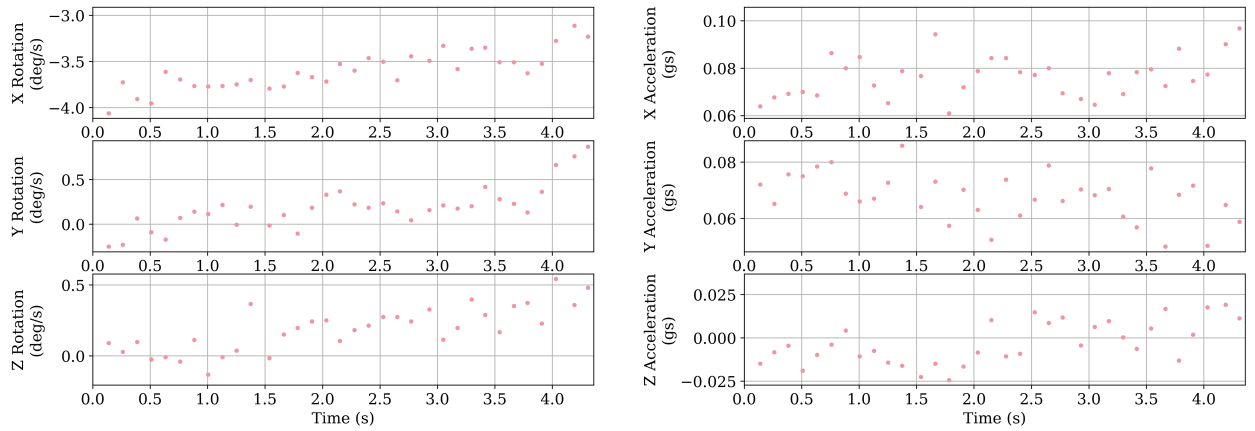


Figure 4.15: IMU D Rotation and Acceleration Rates in the Chamber Reference Frame: Flight 6, CubeSat C1, Trial 8)

Chamber IMU Data
FC3 / Flight 6 / CubeSat C1 / Trial 10
Chamber Reference Frame

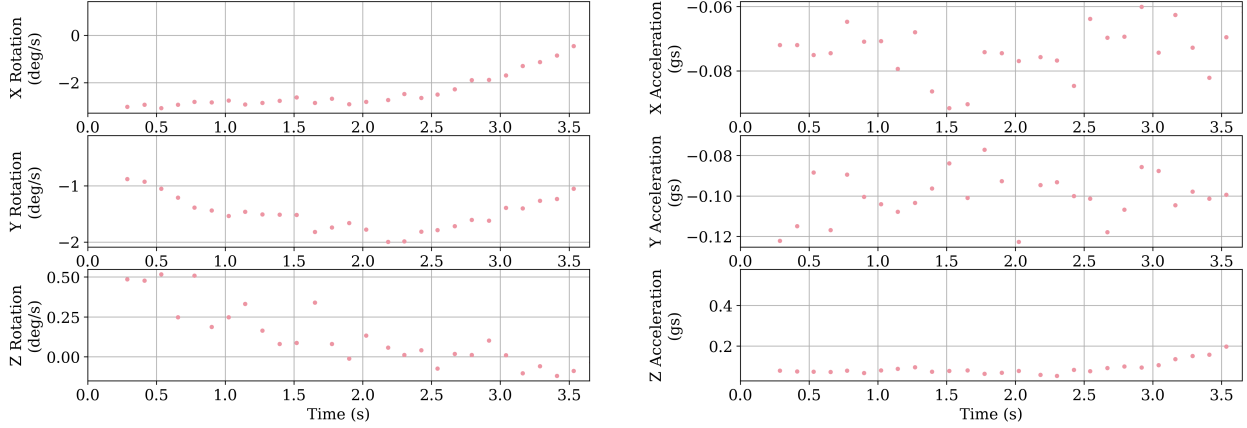


Figure 4.16: IMU D Rotation and Acceleration Rates in the Chamber Reference Frame: Flight 6, CubeSat C1, Trial 10)

4.2.4 Cameras A-D to Inertial Reference Frame Conversion

The CV system attitude estimates were converted into the inertial reference frame by accounting for the chamber’s rotation over the course of experiment trial, as measured by the chamber IMU’s gyroscope. Note that the chamber was attached to the floor of the aircraft, so the rotation of the chamber also represented the rotation of the aircraft over time. The CubeSat testbed’s attitude in the inertial reference frame, q_{cs_i} , was represented as the product of the chamber’s attitude in the inertial reference frame $q_{chamber_i}$, and the CV system measurements in the chamber reference frame, q_{cs_c} , as shown below in Equation 4.1.

$$q_{cs_i} = q_{chamber_i} \otimes q_{cs_c} \quad (4.1)$$

The first step in transforming the CV data into the inertial reference frame was to identify a synchronization point for each camera where the CubeSat testbed’s onboard attitude estimate and the CV attitude estimate matched closely in time. Ideally, this would be taken as the very first point in the CubeSat testbed’s onboard attitude estimate, defined as the identity quaternion; however, each camera may not capture this point due to the position of the CubeSat testbed, ArUco detection failure, or video frame dropouts. Therefore, the synchronization point for each camera in each trial was taken as the first point within which the camera-provided attitude estimate and the CubeSat testbed’s onboard attitude estimate

were within 0.05 seconds of each other. Once the synchronization point was identified, the chamber’s attitude in the inertial reference frame, $q_{chamber_i}$, was solved for at that point by rearranging 4.1 into Equation 4.2. The CV attitude estimate was also set equal to the CubeSat testbed’s onboard attitude estimate at this point.

$$q_{chamber_i} = q_{cs_i} \otimes q_{cs_c}^{-1} \quad (4.2)$$

Once the synchronization step was performed, the subsequent chamber rotations were estimated through propagation with the chamber IMU data, as shown below in Equation 4.3. Since $q_{chamber_i}$ and q_{cs_c} were now known at each time step, Equation 4.1 was used to transform the CV attitude estimates into the inertial frame at each point following the synchronization point.

$$q_{chamber_i,k+1} = q_{chamber_i,k} + \frac{\Delta t}{2} q_{chamber_i,k} \otimes \omega_k \quad (4.3)$$

Validation of Camera A-D Data in Inertial Reference Frame (Flight 6)

The results of 4.2.2 and 4.2.3 were used to convert Trials 1, 5, 7, 8, and 10 into the inertial reference frame. The CV data was then plotted against a gyroscope-propagated attitude estimate of the CubeSat testbed in Figures 4.17 - 4.21. The gyroscope readings were recorded in higher temporal resolution and demonstrated less dropouts than the CV system attitude estimates. While some noise was observed in the CV system attitude estimates, as described in Section 4.2.2, the gyroscope-propagated attitude estimates and CV attitude estimates generally aligned in the inertial reference frame. This validated the CubeSat testbed’s onboard attitude estimation method, ensuring that the inputs to the HDD-RW controller were correct during flight.

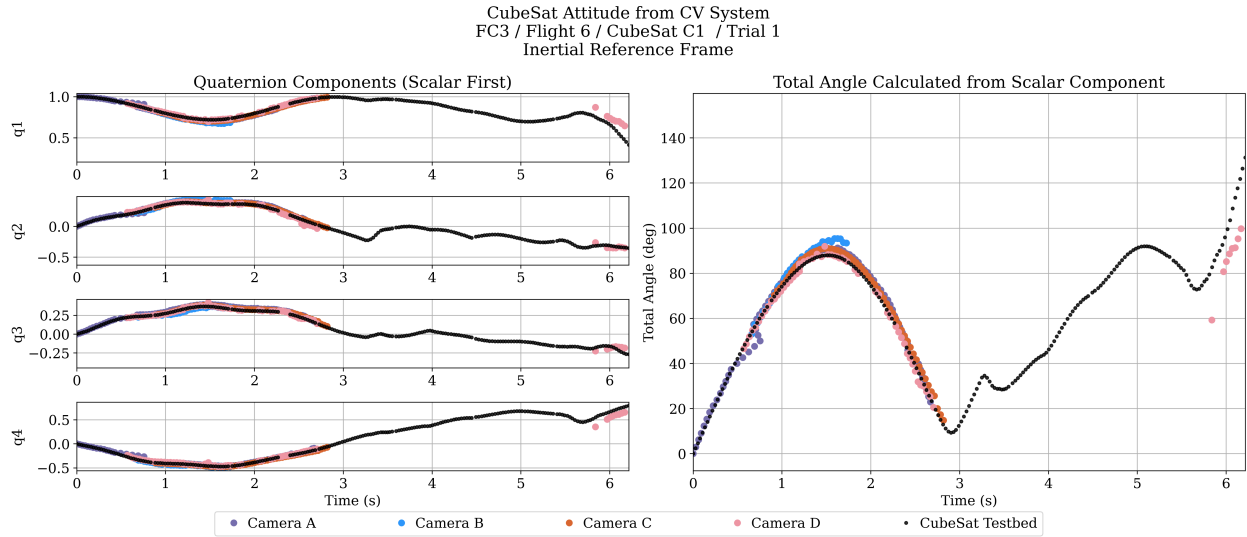


Figure 4.17: CubeSat testbed attitude in the inertial reference frame estimated from cameras A-D: Flight 6, CubeSat C1, Trial 1)

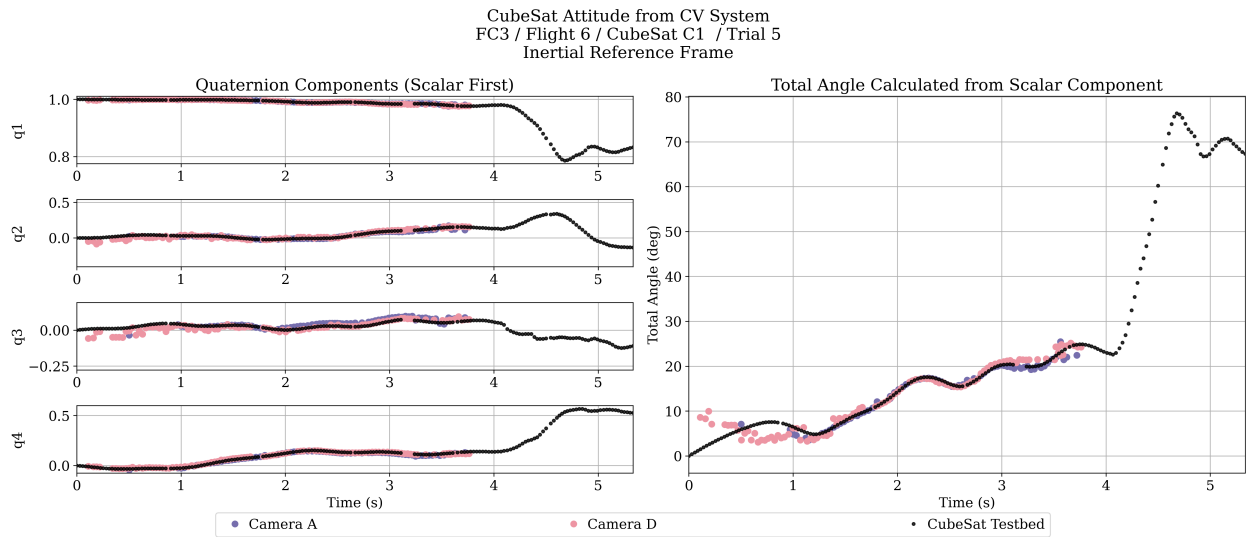


Figure 4.18: CubeSat testbed trajectory in the inertial reference frame estimated from cameras A-D: Flight 6, CubeSat C1, Trial 5)

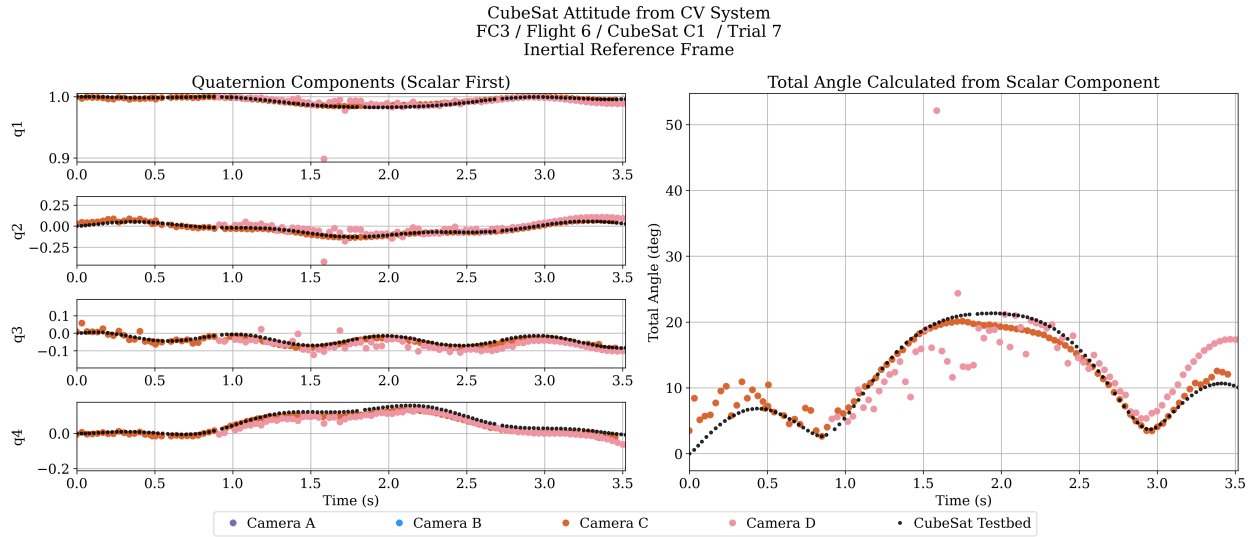


Figure 4.19: CubeSat testbed trajectory in the inertial reference frame estimated from cameras A-D: Flight 6, CubeSat C1, Trial 7)

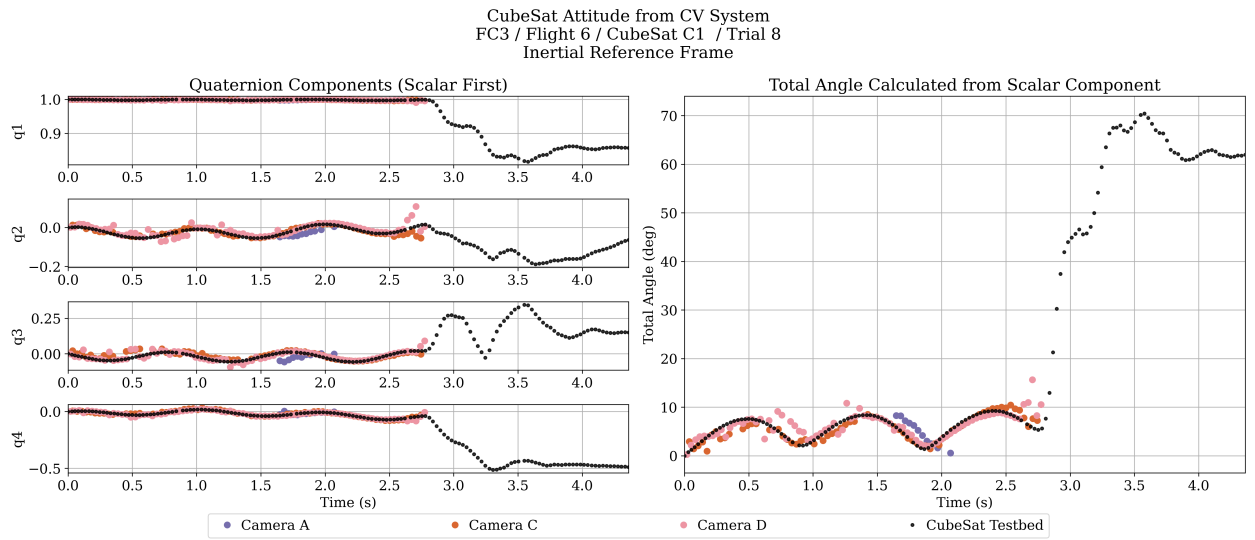


Figure 4.20: CubeSat testbed attitude in the inertial reference frame estimated from cameras A-D: Flight 6, CubeSat C1, Trial 8)

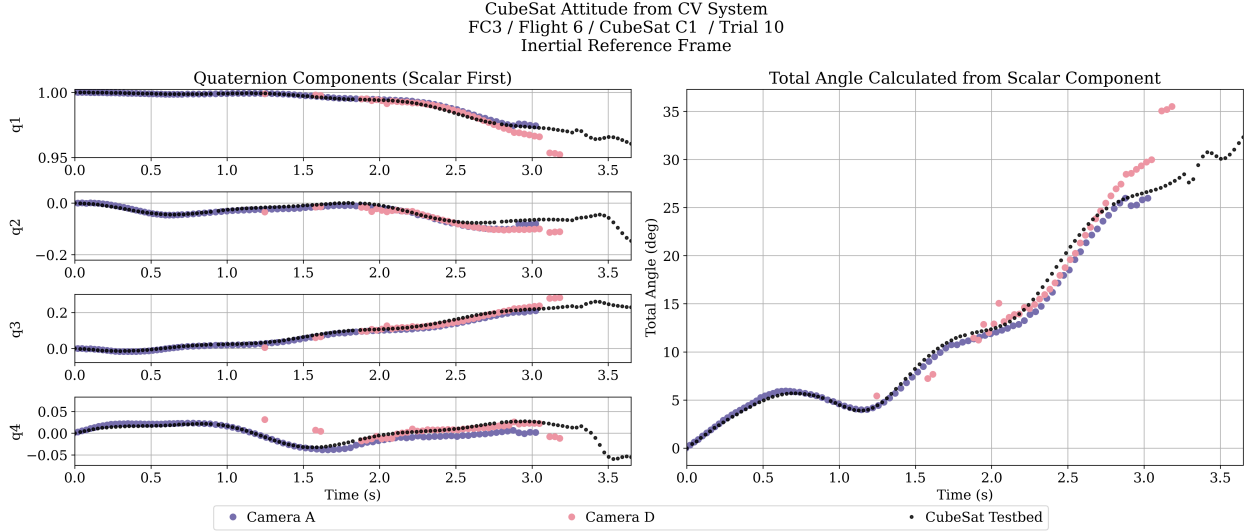


Figure 4.21: CubeSat testbed trajectory in the inertial reference frame estimated from cameras A-D: Flight 6, CubeSat C1, Trial 10)

4.3 Extended Kalman Filter Overview

4.3.1 Introduction

After transforming the CV system attitude estimates into the previously-defined inertial frame, the CV system data and the CubeSat onboard gyroscope data were combined in an Extended Kalman Filter (EKF) to produce a final estimate of the CubeSat testbed's attitude over the experiment. An Additive quaternion EKF (AEKF) was selected over a Multiplicative quaternion EKF (MEKF) for simplicity; however, given additional time, the MEKF is a suggested improvement to this project [23]. For this system, the gyroscope readings were used in the model prediction step to compute a quaternion rotation over each time step and propagate the estimated attitude. The ArUco readings were used in the measurement update step to provide direct measurement of the state. An overview of the EKF structure is shown below in Figure 4.22.

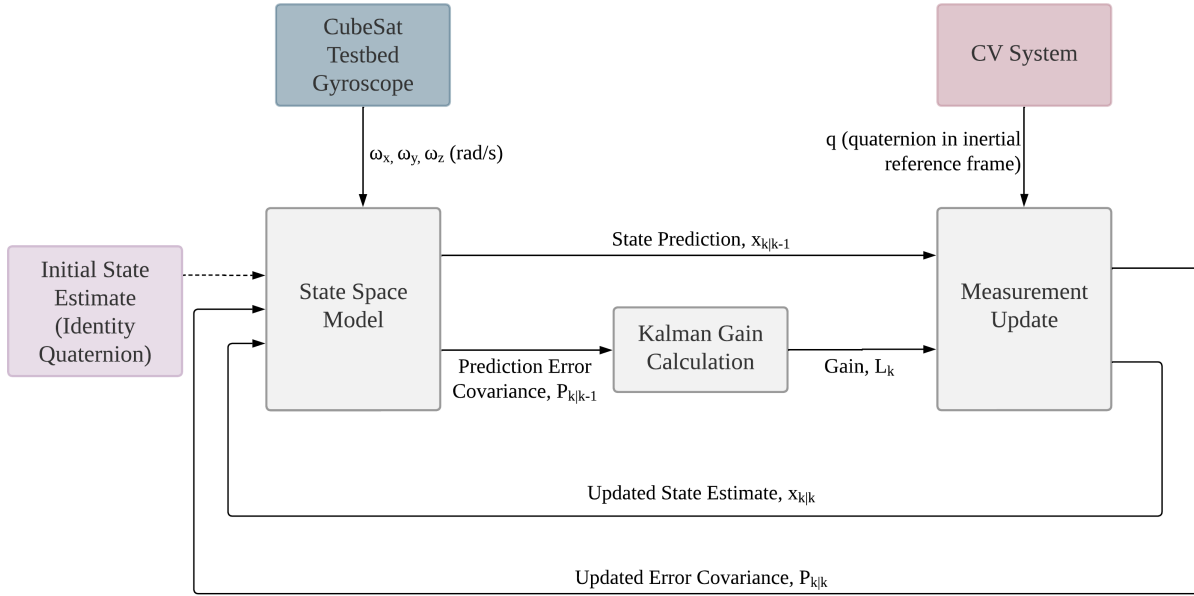


Figure 4.22: Extended Kalman Filter Overview

A few key assumptions were made in developing this EKF. The first assumption was that the gyroscope bias was constant for the duration of all tests. While it is normal practice to estimate gyroscope bias as a state in attitude estimation problems, especially for spacecraft missions, the gyroscope demonstrated no significant drift in the calibration tests described in Section 4.3.4, and all experiments were short duration (between 3-5 seconds). Accordingly, the bias was considered to be a constant. If future tests are performed with longer durations, or if the gyroscope drift becomes more significant, the bias estimation step should be performed.

The other key assumption that the EKF rested on was that the sensor noise for both the IMU and ArUco measurements could be well approximated as Gaussian. As described in Section 4.3.4, the static noise tests for both sensors both demonstrated nearly Gaussian behavior. The resulting variances were used as the basis for the Q and R matrices in the EKF.

4.3.2 State Space Model

The state space model was based on rigid body dynamics and used the previous EKF estimate state along with the gyroscope measurement, ω^b , to predict the next CubeSat

testbed state. The rigid body rotational equation of motion in quaternion form is given by Equation 4.4. This equation was discretized for the EKF by linearizing the continuous Equation 4.4 about the previous time step, as shown in Equation 4.5. The discrete form in Equation 4.5 was rewritten as Equation 4.7 using the quaternion multiplication form shown in Equation 4.6. The observability matrix, \mathbf{O} , was calculated as shown in Equation 4.8 and was found to be of full rank; therefore the system was fully observable and thus detectable.

$$\dot{\mathbf{q}}(t) = \frac{\Delta t}{2} \mathbf{q}(t) \otimes \boldsymbol{\omega}^b(t) \quad (4.4)$$

$$\mathbf{q}_{k+1} = \mathbf{q}_k + \frac{\Delta t}{2} \mathbf{q}_k \otimes \boldsymbol{\omega}_k^b \quad (4.5)$$

$$\mathbf{q} \otimes \boldsymbol{\omega}^b = \begin{bmatrix} q_0\omega_0 - q_1\omega_x - q_2\omega_y - q_3\omega_z \\ q_0\omega_x + q_1\omega_0 + q_2\omega_z - q_3\omega_y \\ q_0\omega_y - q_1\omega_z + q_2\omega_0 + q_3\omega_x \\ q_0\omega_z + q_1\omega_y - q_2\omega_x + q_3\omega_0 \end{bmatrix} \quad (4.6)$$

$$\mathbf{q}_{k+1} = \mathbf{q}_k + \frac{\Delta t}{2} \begin{bmatrix} 0 & -\omega_x^b & -\omega_y^b & -\omega_z^b \\ \omega_x^b & 0 & \omega_z^b & -\omega_y^b \\ \omega_y^b & -\omega_z^b & 0 & \omega_x^b \\ \omega_z^b & \omega_y^b & -\omega_x^b & 0 \end{bmatrix} \mathbf{q}_k \quad (4.7)$$

$$\mathbf{O} = \begin{bmatrix} C \\ CA \\ CA^2 \\ CA^3 \end{bmatrix} \quad (4.8)$$

$$\text{rank}(\mathbf{O}) = 4 \quad (4.9)$$

4.3.3 Extended Kalman Filter Design

The estimated state, \mathbf{x} , was the attitude quaternion vector, \mathbf{q} , describing the CubeSat testbed's attitude in the inertial reference frame. The CV system measurement, \mathbf{y} , directly

measured the attitude quaternion, \mathbf{q} , with some error, \mathbf{v} , that was modeled to be a zero-mean Gaussian vector.

$$\mathbf{x} \triangleq \mathbf{q} = \begin{bmatrix} q_0 \\ q_1 \\ q_2 \\ q_3 \end{bmatrix} \quad (4.10)$$

$$\mathbf{y} \triangleq \mathbf{q} + \mathbf{v} \quad (4.11)$$

$$u \triangleq 0 \quad (4.12)$$

The state space equation given by Equation 4.7 was used to define the EKF state space equation, f , as shown in Equation 4.13. The resulting value from the state space equation, $\hat{\mathbf{x}}_{k|k-1}$, was normalized to ensure it was a unit-quaternion. Taking the Jacobian of the state space equation resulted in the matrices for the EKF, shown in Equations 4.14 through 4.17. The matrices C and F were equivalent to the identity matrix as the measurement represented the state itself. The matrix A was a large 4×4 matrix explicitly defined in Appendix B.1 .

$$\hat{\mathbf{x}}_{k|k-1} = \mathbf{f}_k(\hat{\mathbf{x}}_{k-1|k-1}, u_{k-1}, 0) = \left(I + \frac{\Delta t}{2} \begin{bmatrix} 0 & -\omega_x^b & -\omega_y^b & -\omega_z^b \\ \omega_x^b & 0 & \omega_z^b & -\omega_y^b \\ \omega_y^b & -\omega_z^b & 0 & \omega_x^b \\ \omega_z^b & \omega_y^b & -\omega_x^b & 0 \end{bmatrix} \right) \hat{\mathbf{q}}_{k-1|k-1} \quad (4.13)$$

$$\mathbf{A}_{k-1} = \left. \frac{\partial \mathbf{f}_k}{\partial \mathbf{x}_k} \right|_{\hat{\mathbf{x}}_{k-1|k-1}} = [\mathbf{A}_{k-1}(\hat{\mathbf{q}}_{k-1|k-1}, \boldsymbol{\omega}_k)]_{4 \times 4} \quad (4.14)$$

$$\mathbf{E}_{k-1} = \left. \frac{\partial \mathbf{f}_k}{\partial \boldsymbol{\omega}_k} \right|_{\hat{\mathbf{x}}_{k-1|k-1}} = \frac{\Delta t}{2} \frac{1}{\mathbf{q}_{k-1|k-1}} \begin{bmatrix} q_1 & q_2 & q_3 \\ -q_0 & q_3 & -q_2 \\ -q_3 & -q_0 & q_1 \\ q_2 & -q_1 & -q_0 \end{bmatrix} \quad (4.15)$$

$$\mathbf{C}_k = \left. \frac{\partial \mathbf{h}_k}{\partial \mathbf{x}_k} \right|_{\hat{\mathbf{x}}_{k|k-1}} = I_{4 \times 4} \quad (4.16)$$

$$\mathbf{F}_k = \left. \frac{\partial \mathbf{h}_k}{\partial \mathbf{v}_k} \right|_{\hat{\mathbf{x}}_{k|k-1}} = I_{4 \times 4} \quad (4.17)$$

4.3.4 Sensor Characterization

CubeSat Gyroscopes

An Adafruit ICM20649 6DOF IMU, which consists of an accelerometer and gyroscope, was packaged inside each CubeSat testbed. Each CubeSat testbed recorded accelerometer and gyroscope data at approximately 30Hz during experiment operations. The angular velocity values read from the gyroscope were fed into the model prediction step of the EKF. The gyroscope axes were not physically aligned with the CubeSat testbed body axes; angular velocity readings were read in the gyroscope reference frame, then transformed into the CubeSat testbed body frame in the CubeSat testbed's flight software. All gyroscope data in this section will be presented in the CubeSat testbed's body reference frame.

Gyroscope error can be characterized by three parameters: offset bias, drift rate, and stochastic noise. The offset bias is an offset between the true rotation rate of the sensor and the measured rotation rate of the sensor. Offset bias typically changes approximately linearly with time - the rate at which the offset bias changes over time is called the drift rate. The stochastic noise causes error that can not be predicted but can be characterized by its distribution. The offset bias, drift rate, and stochastic noise of the gyroscope used was characterized by measuring gyroscope data from each of the sensor's three axes for 30 minutes while the sensor was at rest. The gyroscope data was then transformed into the CubeSat testbed body reference frame. A linear regression was applied to the measured data; the offset bias was taken to be the y-intercept of the linear fit and the drift-rate was taken to be the slope of the linear fit. The stochastic noise was characterized by the standard deviation of the difference between the measured data and linear fit. The drift rate found from the static test of the gyroscope was small enough such that the offset bias could be considered constant over the periods of time where data was collected for this project. The offset bias, drift rate, and stochastic noise of the gyroscope are presented in Figures [4.23-4.25](#)

and summarized in Table 4.3. While only CubeSat testbed C1 will be analyzed with the EKF, the calibration results for testbeds B and C2 are also presented for comparison.

The error distribution of the gyroscope rotation rates from the static measurements was approximately Gaussian, as shown by the measurement data distribution and Gaussian fit in Figures 4.23-4.25. The Gaussian fit provided standard deviations and variances are shown in Table 4.3. Since the noise was approximately Gaussian, the gyroscope measurements were appropriate to use in the EKF.

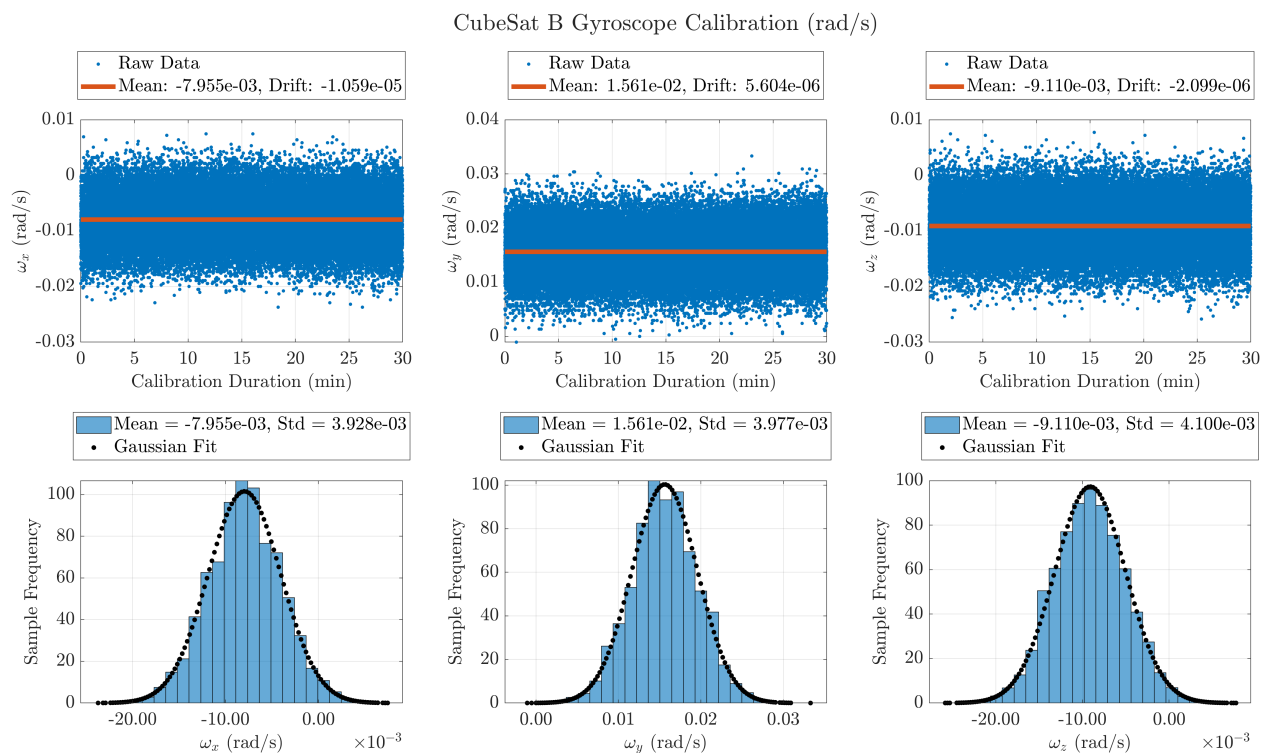


Figure 4.23: CubeSat Testbed B Gyroscope Calibration (Presented in Testbed Body Reference Frame)

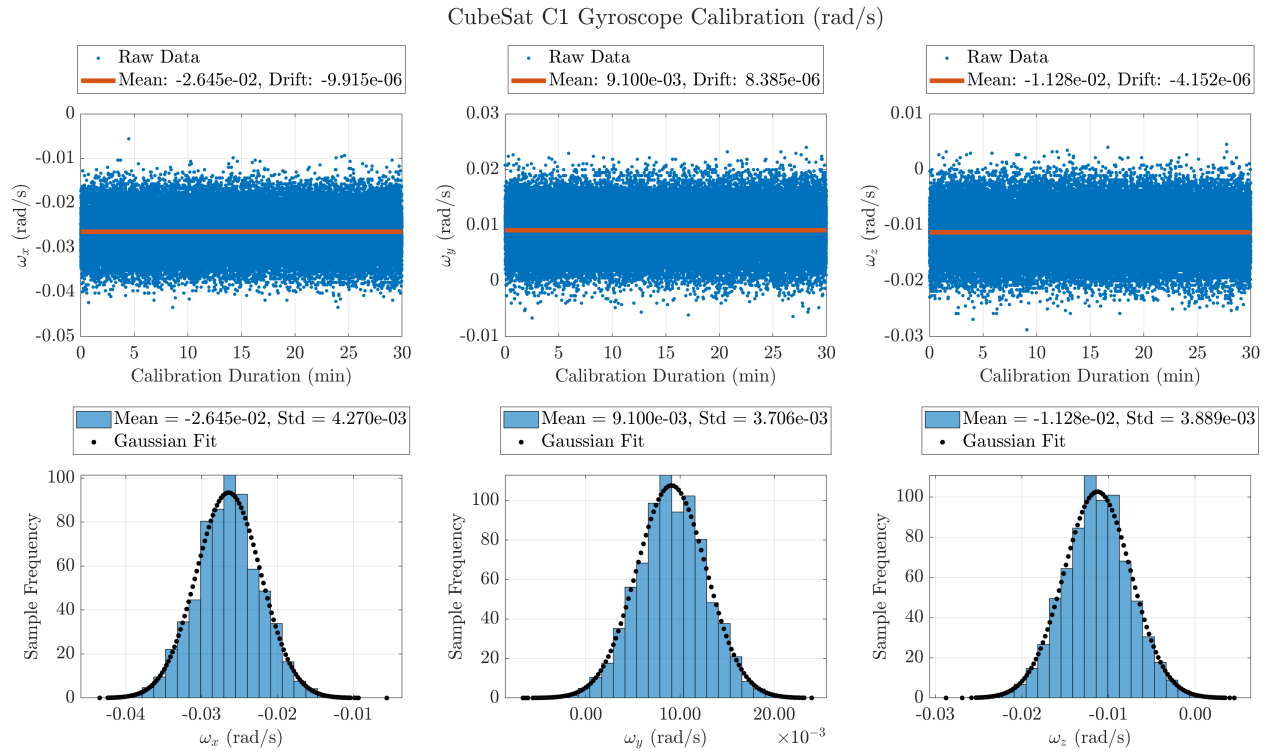


Figure 4.24: CubeSat Testbed C1 Gyroscope Calibration (Presented in Testbed Body Reference Frame)

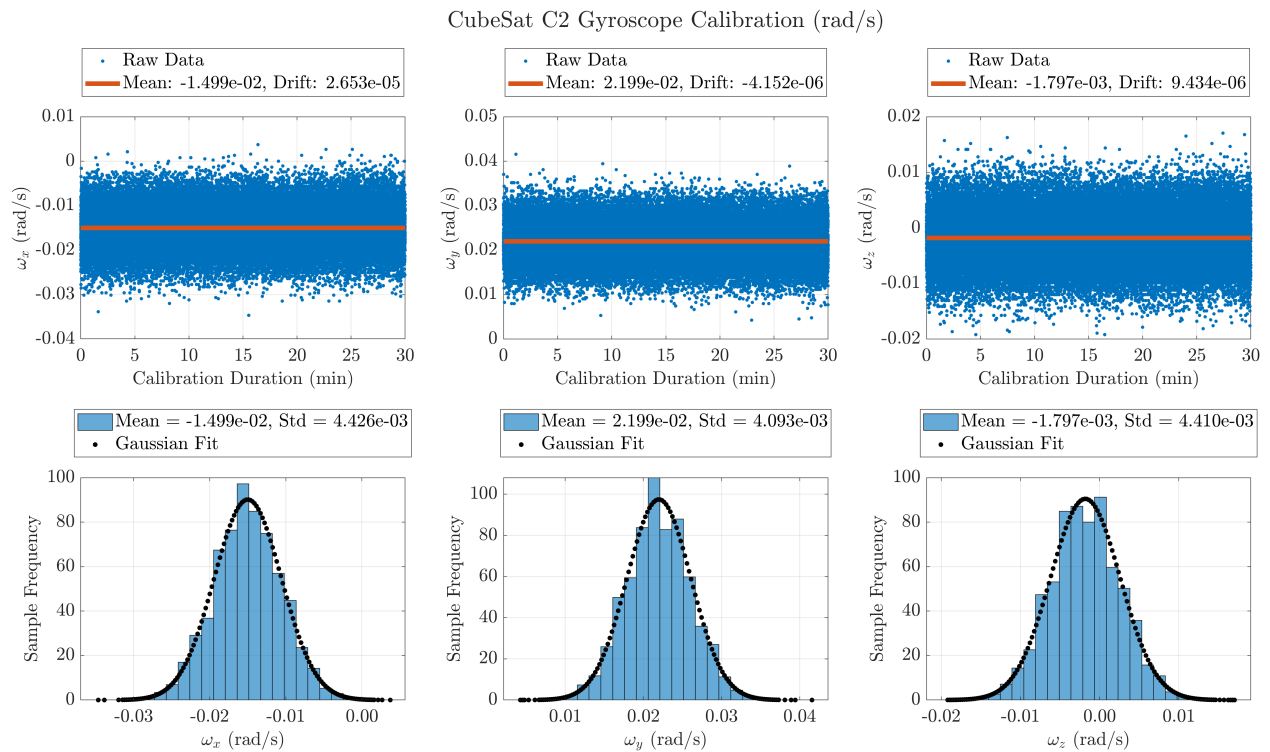


Figure 4.25: CubeSat Testbed C2 Gyroscope Calibration (Presented in Testbed Body Reference Frame)

Table 4.3: Gyroscope Measurement Characteristics, Presented in the CubeSat Testbed Body Frame

CubeSat Testbed	CubeSat Testbed Axis	Offset Bias (rad/s)	Drift Rate (rad/s ²)	Noise Std. Dev. (rad/s)	Noise Variance (rad ² /s ²)
B	x	-7.954e-03	-1.764e-07	3.928e-03	1.543e-05
	y	1.561e-02	9.340e-08	3.977e-03	1.582e-05
	z	-9.110e-03	-3.498e-08	4.100e-03	1.680e-05
C1	x	-2.645e-02	-1.652e-07	4.270e-03	1.823e-05
	y	9.100e-02	1.398e-07	3.706e-03	1.373e-05
	z	-1.128e-02	-6.919e-08	3.889e-03	1.512e-05
C2	x	-1.499e-02	4.421e-07	4.426e-03	1.958e-05
	y	2.199e-02	6.919e-08	4.093e-03	1.675e-05
	z	-1.797e-03	1.572e-07	4.410e-03	1.945e-05

Chamber Gyroscopes

As described in Section 4.2.4, the gyroscopes attached to the CV system cameras were used to propagate the aircraft attitude. Cameras A-D each had a MPU6050 6DOF IMU attached to their Raspberry Pi computer. Each gyroscope on the chamber was calibrated with the same process as described in for the CubeSat testbed gyroscopes. Chamber gyroscopes A-C all demonstrated significant nonlinear drift and high bias; therefore, only gyroscope D was used to propagate the aircraft attitude. The offset bias, drift rate, and stochastic noise of the gyroscope are presented in Figure 4.26 and summarized in Table 4.4.

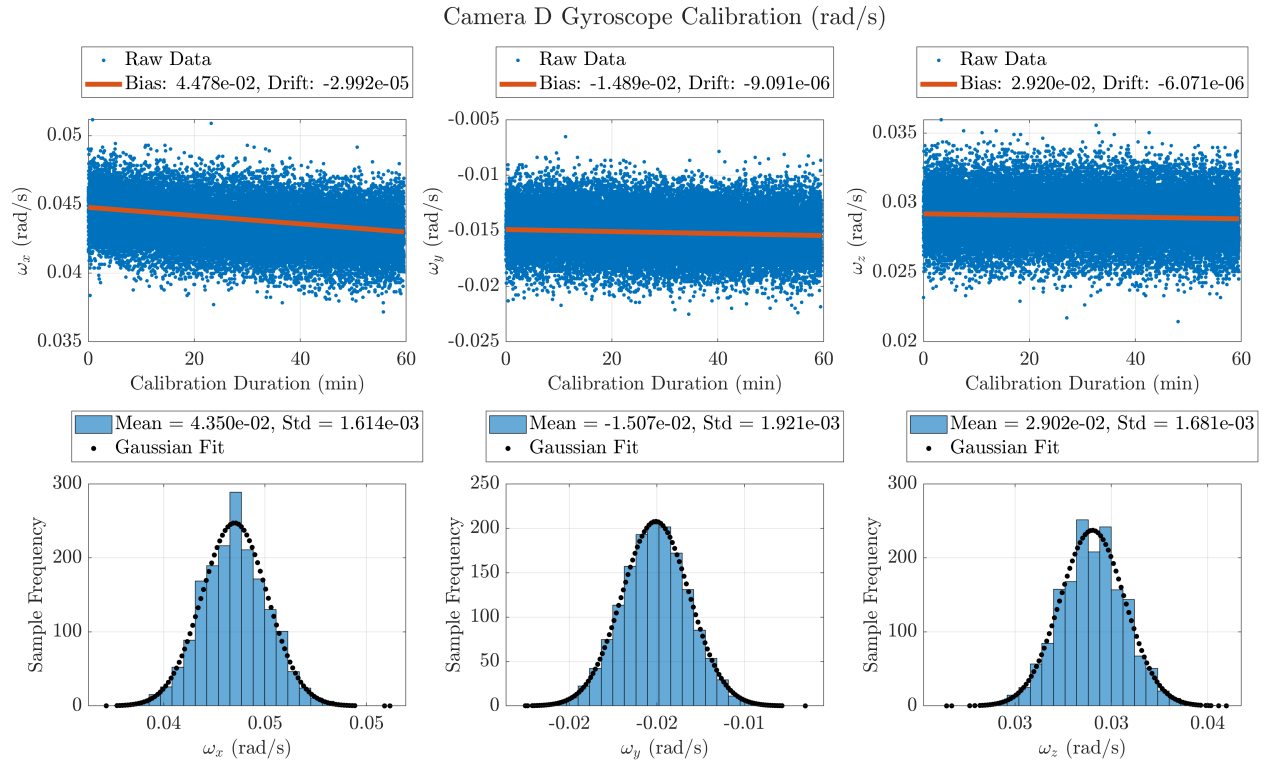


Figure 4.26: Camera D Gyroscope Calibration (Presented in Gyroscope Reference Frame)

Table 4.4: Camera D Gyroscope Measurement Characteristics, Presented in the Gyroscope Reference Frame

Camera	Gyroscope Axis	Offset Bias (rad/s)	Drift Rate (rad/s ²)	Noise Std. Dev. (rad/s)	Noise Variance (rad ² /s ²)
D	x	4.478e-02	-2.992e-05	1.614e-03	2.605e-06
	y	-1.489e-02	-9.091e-06	1.921e-03	3.689e-06
	z	2.920e-02	-6.071e-06	1.681e-03	2.827e-06

CV System

The CV system CubeSat testbed attitude estimates, provided as quaternions, served as the measurement update source for the EKF. As explained in Chapter 3, the CV system performance was dependent on the CubeSat testbed’s distance and orientation relative to each camera, as well as lighting conditions, motion blur, and marker occlusion. When combining the CV system pose estimates with the IMU measurements in the EKF, it was necessary

to account for the uncertainty in the ArUco board detection process. The CV system accuracy and uncertainty was characterized in Section 3.4 by placing the testbed in various positions and orientations relative to Camera E, and comparing the resulting pose estimates to ground truth values. The attitude noise distribution from the static measurements was approximately Gaussian, as shown by the measurement data distribution and Gaussian fit in Section 3.4.3, and therefore was appropriate for use in the EKF. At each step in the EKF, a CV measurement was selected from only the most trustworthy camera at that point; this was dependent on successful ArUco detection, the time difference between the CV measurement and CubeSat gyroscope measurement, the measurement noise level, and the proximity of the CubeSat testbed relative to each camera.

4.3.5 EKF Results

The EKF was run for the same five trials previously analyzed in Sections 4.2 and 4.3.4, and the results are displayed below in both quaternion and Euler angle form. For each plot, the CV system attitude estimates are displayed as red dots, the open loop attitude estimates from gyroscope propagation are shown as a blue line, and the EKF results are displayed as a black line. The green line on each plot represents the CubeSat testbed's onboard attitude estimate during the each experiment trial - these used the same attitude estimation method as the open loop method, but differed slightly in results due to the controller frequency and the presence of a low-pass filter on the input gyroscope data in flight. For most trials, the EKF results closely followed the open loop estimation results, since the CubeSat testbed gyroscopes demonstrated low measurement uncertainty in Section 4.3.4.

Trial 1

The CubeSat testbed underwent a large rotation in the first three seconds of the trial, as shown in Figures 4.27 and 4.28, and was captured by all cameras in the CV system. The EKF was robust to the measurement noise in the CV system in this area, and was not largely affected by measurement outliers. The CV system measurements then experienced a dropout between 3-6 seconds, where the EKF compensated by relying on the gyroscope-propagated attitude estimates. For the most part, all attitude estimates closely aligned in value, with the EKF providing a smoother, higher frequency CubeSat testbed attitude estimate than the testbed's own controller.

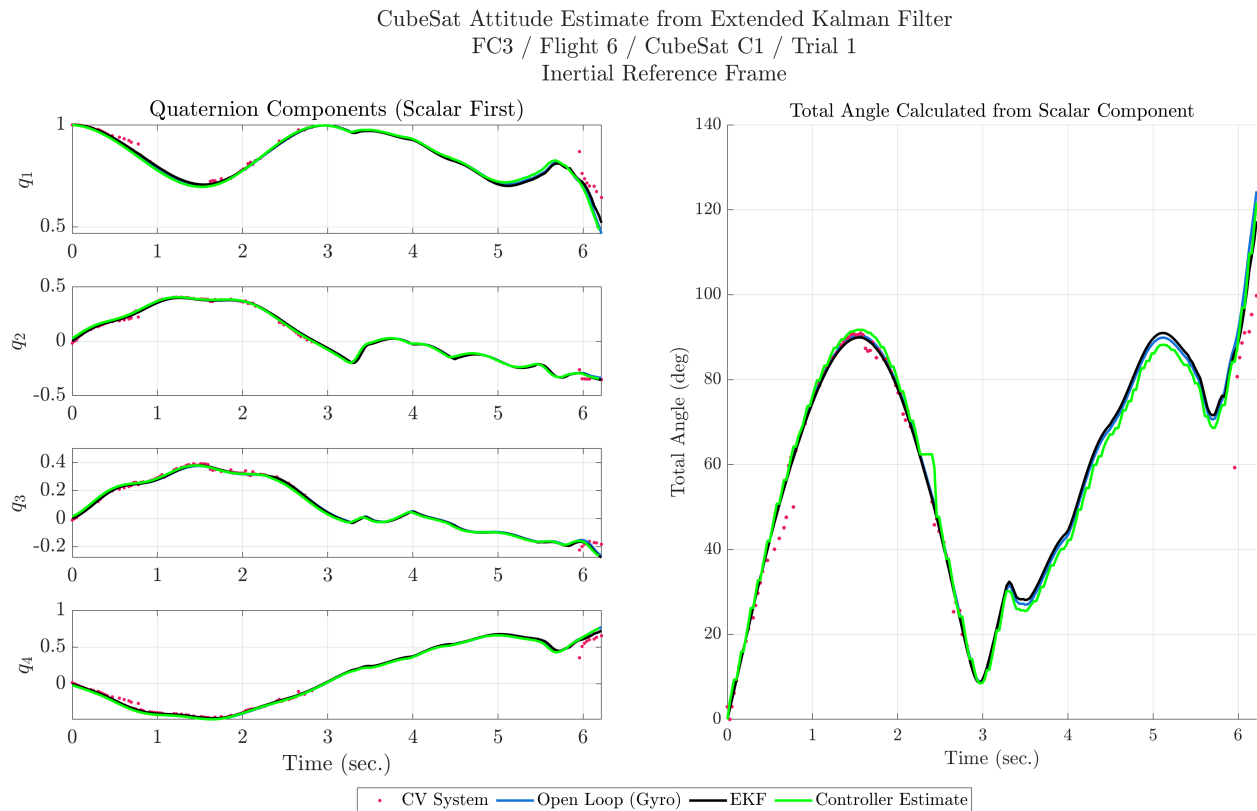


Figure 4.27: CubeSat testbed attitude estimated by EKF: Flight 6, CubeSat C1, Trial 1)

CubeSat Attitude Estimate from Extended Kalman Filter - Euler Angles
FC3 / Flight 6 / CubeSat C1 / Trial 1
Inertial Reference Frame

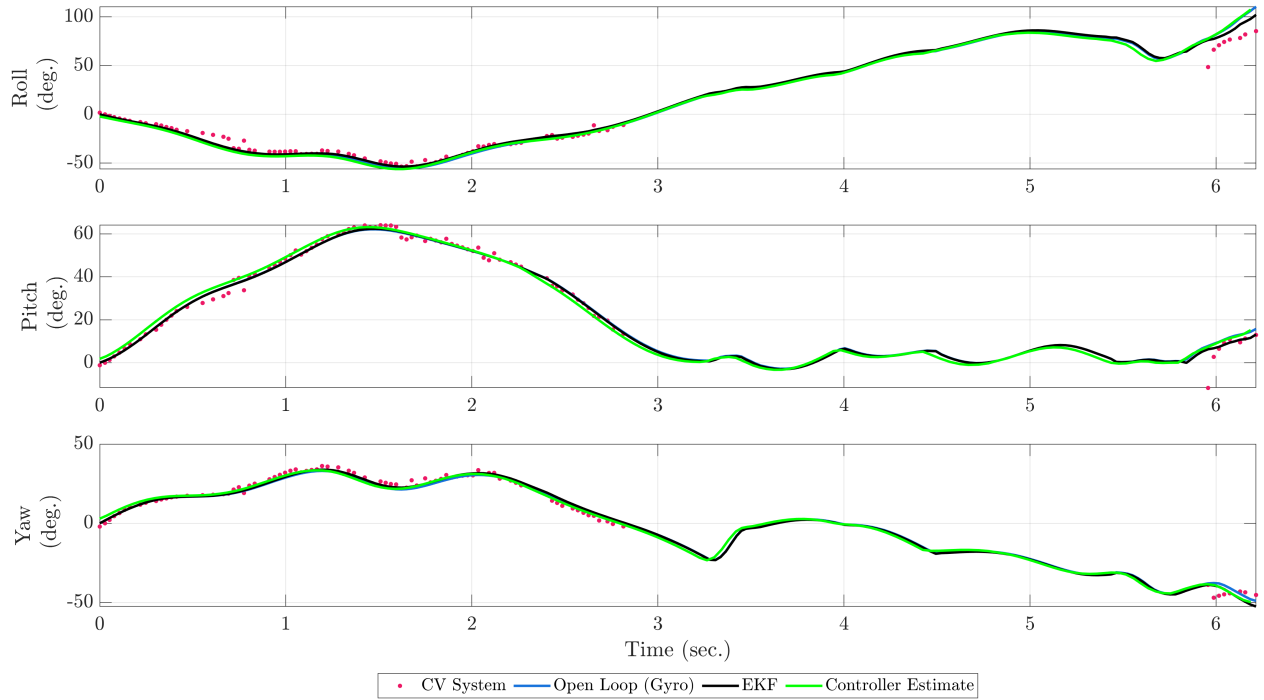


Figure 4.28: CubeSat testbed attitude (euler angles) estimated by EKF: Flight 6, CubeSat C1, Trial 1)

Trial 5

The CubeSat testbed underwent multiple small oscillations in attitude over the first four seconds of the trial, followed by a large rotation near the end of the trial, as shown in Figures 4.29 and 4.28. Attitude estimates from Cameras A and D were used as measurement updates to the EKF, which was robust to the CV system measurement outliers in the first second of the trial. The CV system measurements then experienced a dropout for the final portion of the experiment, where the EKF compensated by relying on the gyroscope-propagated attitude estimates. All attitude estimates closely aligned in value, with the exception of the CV system measurement outliers at the beginning of the trial. The EKF results verified the controller attitude estimates, indicating that the onboard attitude determination procedure was implemented correctly.

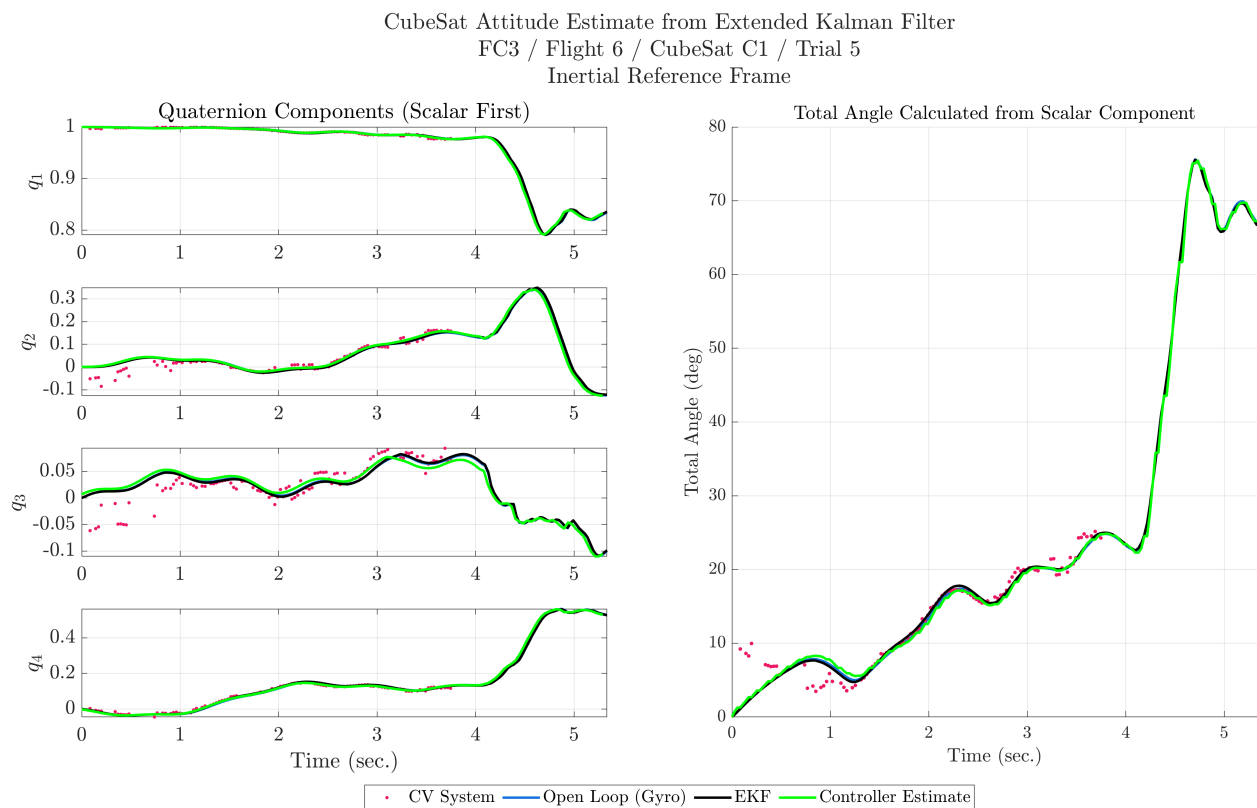


Figure 4.29: CubeSat testbed attitude estimated by EKF: Flight 6, CubeSat C1, Trial 5)

CubeSat Attitude Estimate from Extended Kalman Filter - Euler Angles
FC3 / Flight 6 / CubeSat C1 / Trial 5
Inertial Reference Frame

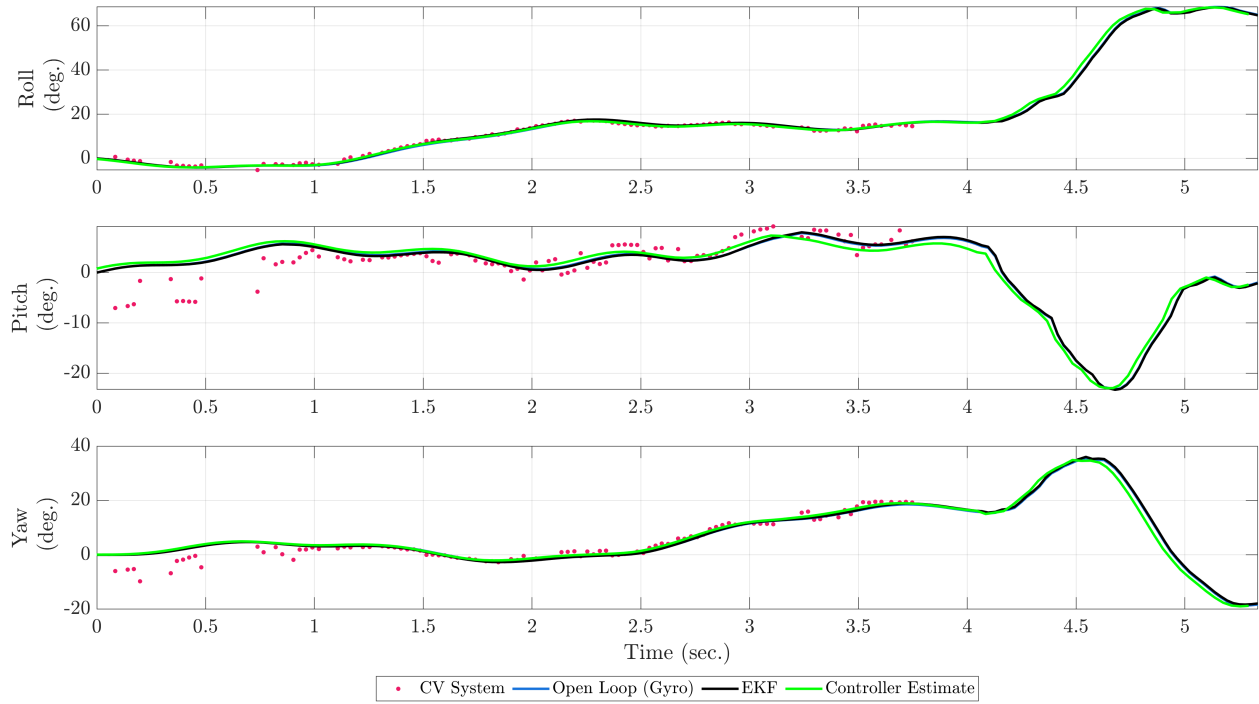


Figure 4.30: CubeSat testbed attitude (euler angles) estimated by EKF: Flight 6, CubeSat C1, Trial 5)

Trial 7

The CubeSat testbed first performed a small rotation in the first second of the trial, followed by a large rotation, as shown in Figures 4.31 and 4.32. Attitude estimates from Camera C were used as measurement updates to the EKF, which was robust to the CV system measurement outliers in the first second of the trial. All attitude estimates closely aligned in value, with the exception of the measurement outliers between 1.5-2.5 seconds, where the CV system underestimated the testbed's total angle. The EKF results verified the controller attitude estimates, indicating that the onboard attitude determination procedure was implemented correctly.

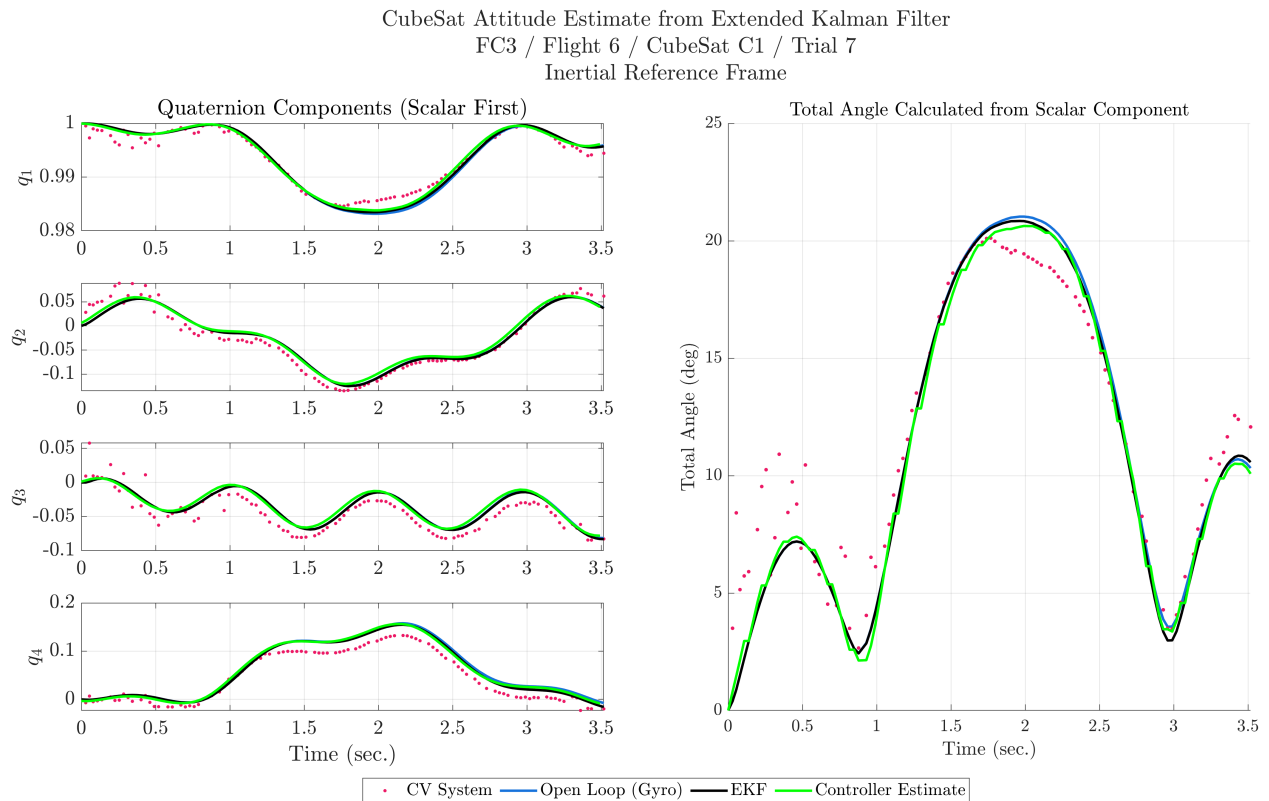


Figure 4.31: CubeSat testbed attitude estimated by EKF: Flight 6, CubeSat C1, Trial 7)

CubeSat Attitude Estimate from Extended Kalman Filter - Euler Angles
FC3 / Flight 6 / CubeSat C1 / Trial 7
Inertial Reference Frame

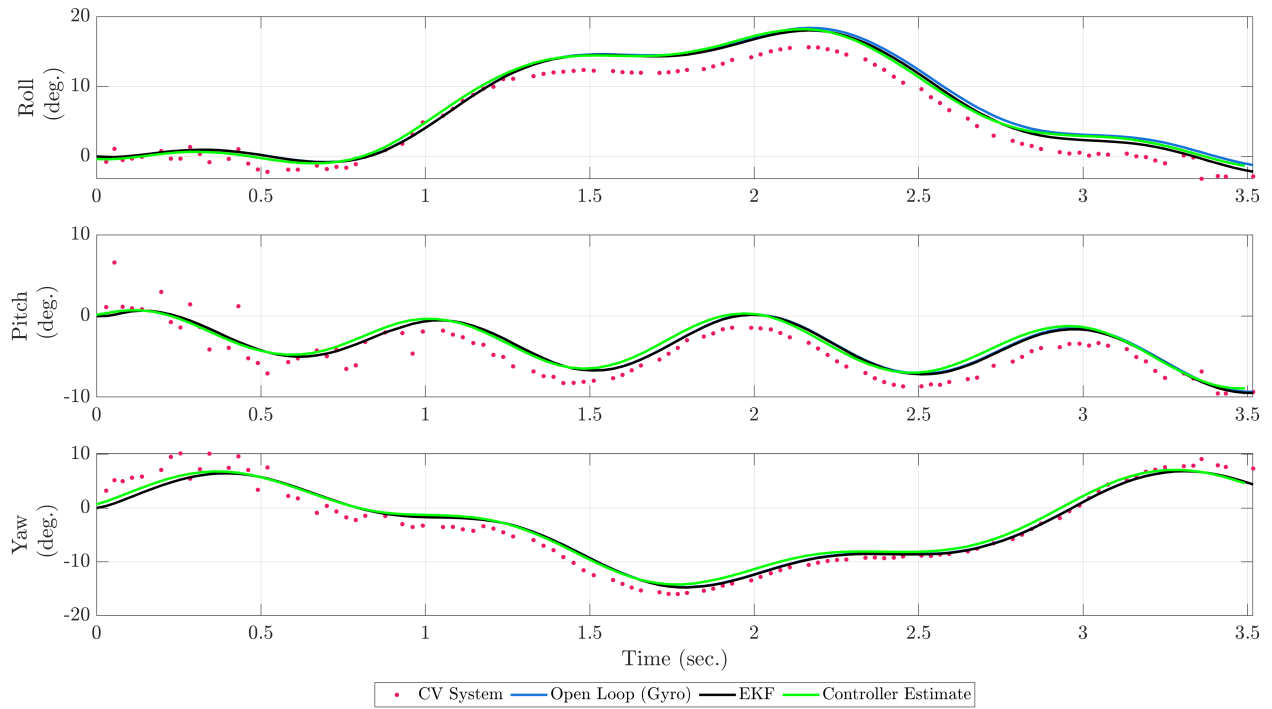


Figure 4.32: CubeSat testbed attitude (euler angles) estimated by EKF: Flight 6, CubeSat C1, Trial 7)

Trial 8

The CubeSat testbed underwent multiple small oscillations in attitude over the first three seconds of the trial, followed by a large rotation near the end of the trial, as shown in Figures 4.33 and 4.34. Attitude estimates from Cameras C and D were used as measurement updates to the EKF, which was robust to the CV system measurement outliers in the first 1.5 seconds of the trial. The CV system measurements then experienced a dropout between 3-4.5 seconds, where the EKF compensated by relying on the gyroscope-propagated attitude estimates. All attitude estimates closely aligned in value, with the exception of the CV system measurement outliers at the beginning of the trial. The EKF results verified the controller attitude estimates, indicating that the onboard attitude determination procedure was implemented correctly.

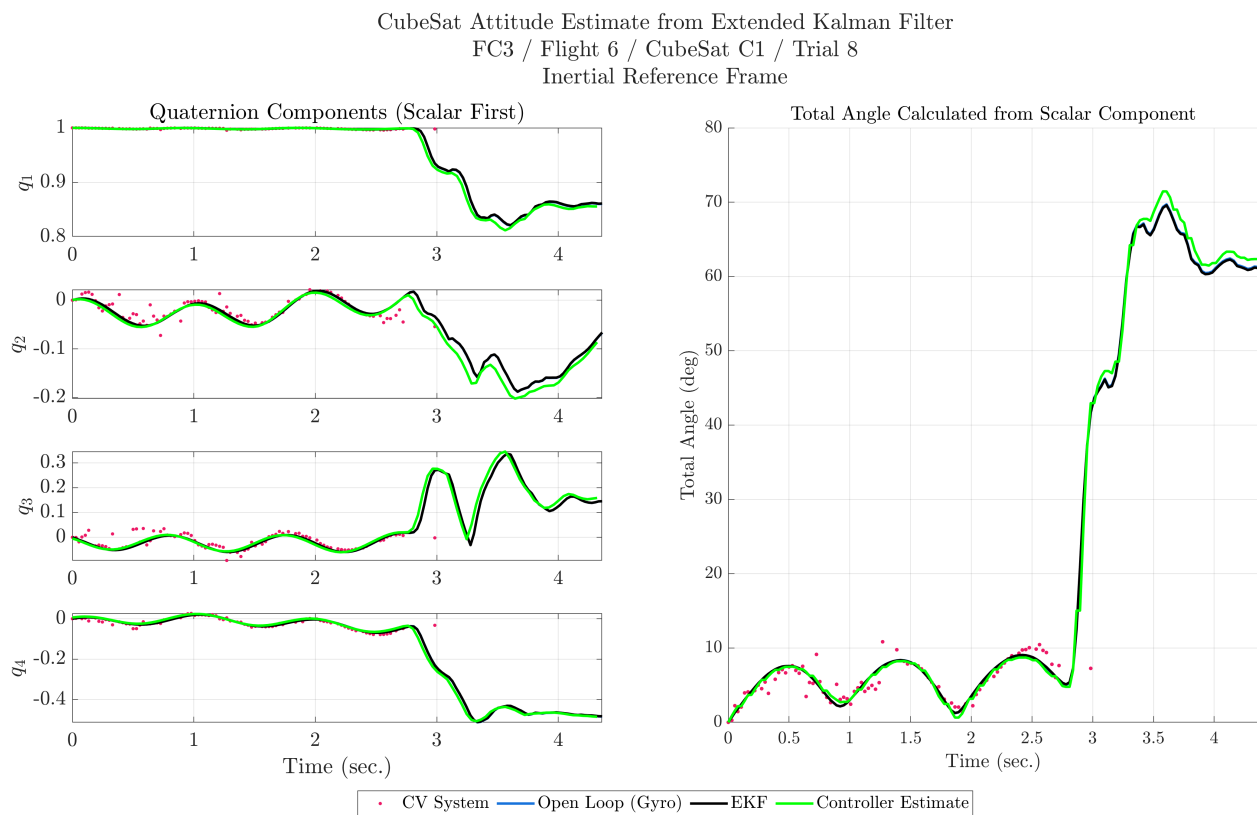


Figure 4.33: CubeSat testbed attitude estimated by EKF: Flight 6, CubeSat C1, Trial 8)

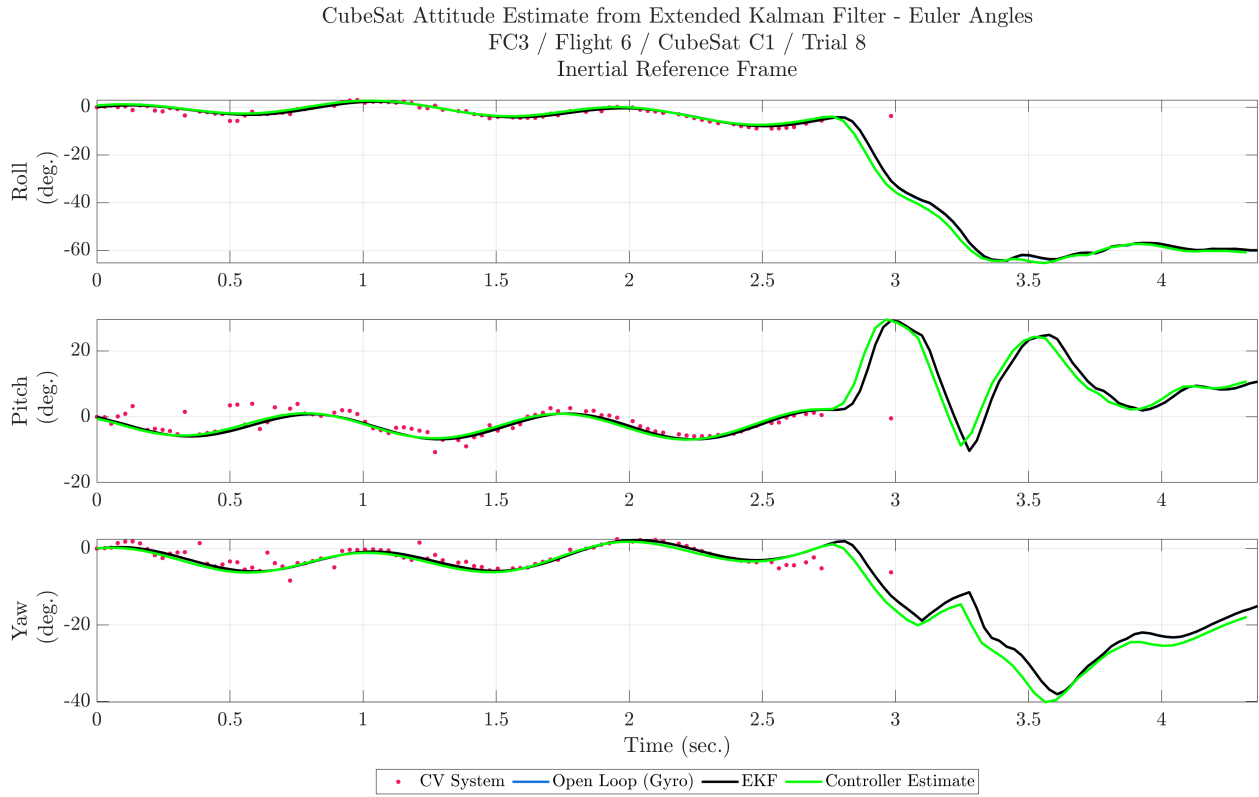


Figure 4.34: CubeSat testbed attitude (euler angles) estimated by EKF: Flight 6, CubeSat C1, Trial 8)

Trial 10

The CubeSat testbed underwent multiple small oscillations as it performed a large rotation over the trial, as shown in Figures 4.35 and 4.36. Attitude estimates from Camera A were used as measurement updates to the EKF, and did not demonstrate significant noise or outliers. While the CV system slightly underestimated the total rotation angle of the CubeSat testbed between 2-3 seconds, all attitude estimates closely aligned in value. The EKF results verified the controller attitude estimates, indicating that the onboard attitude estimation procedure was implemented correctly.

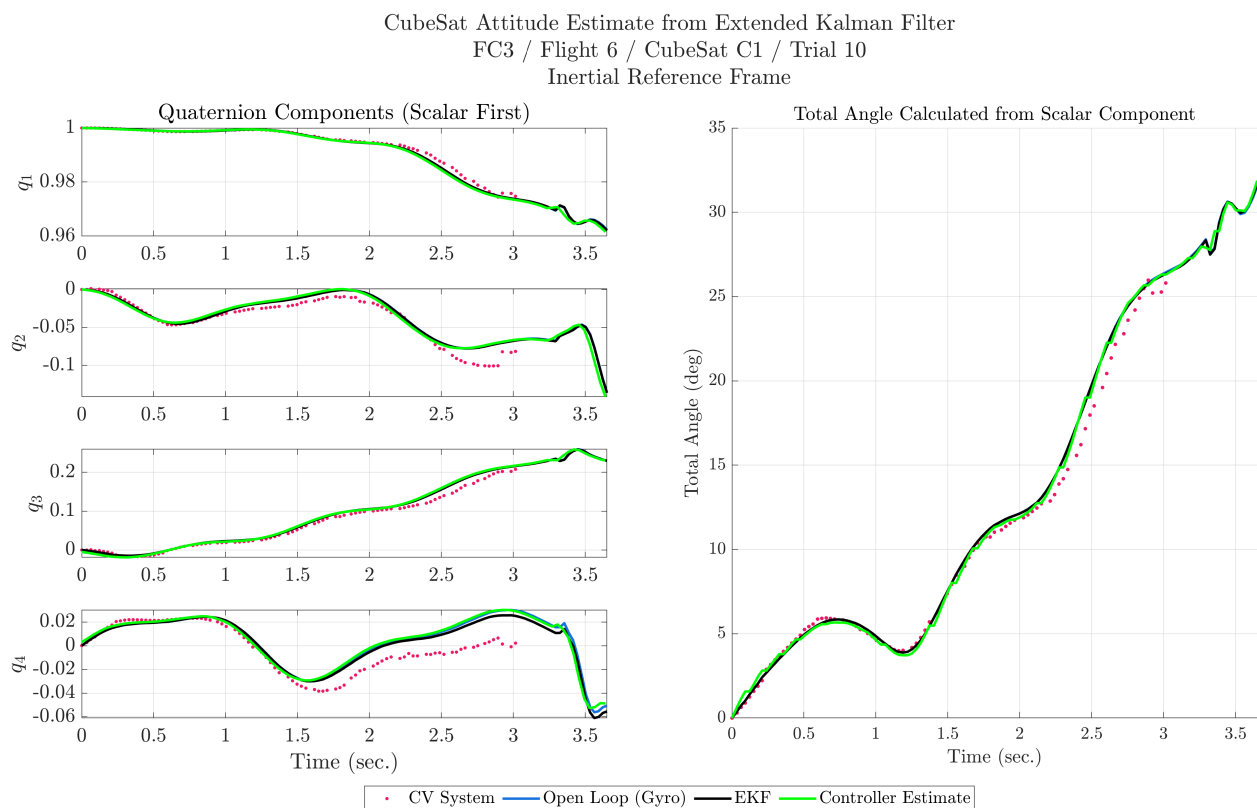


Figure 4.35: CubeSat testbed attitude estimated by EKF: Flight 6, CubeSat C1, Trial 10)

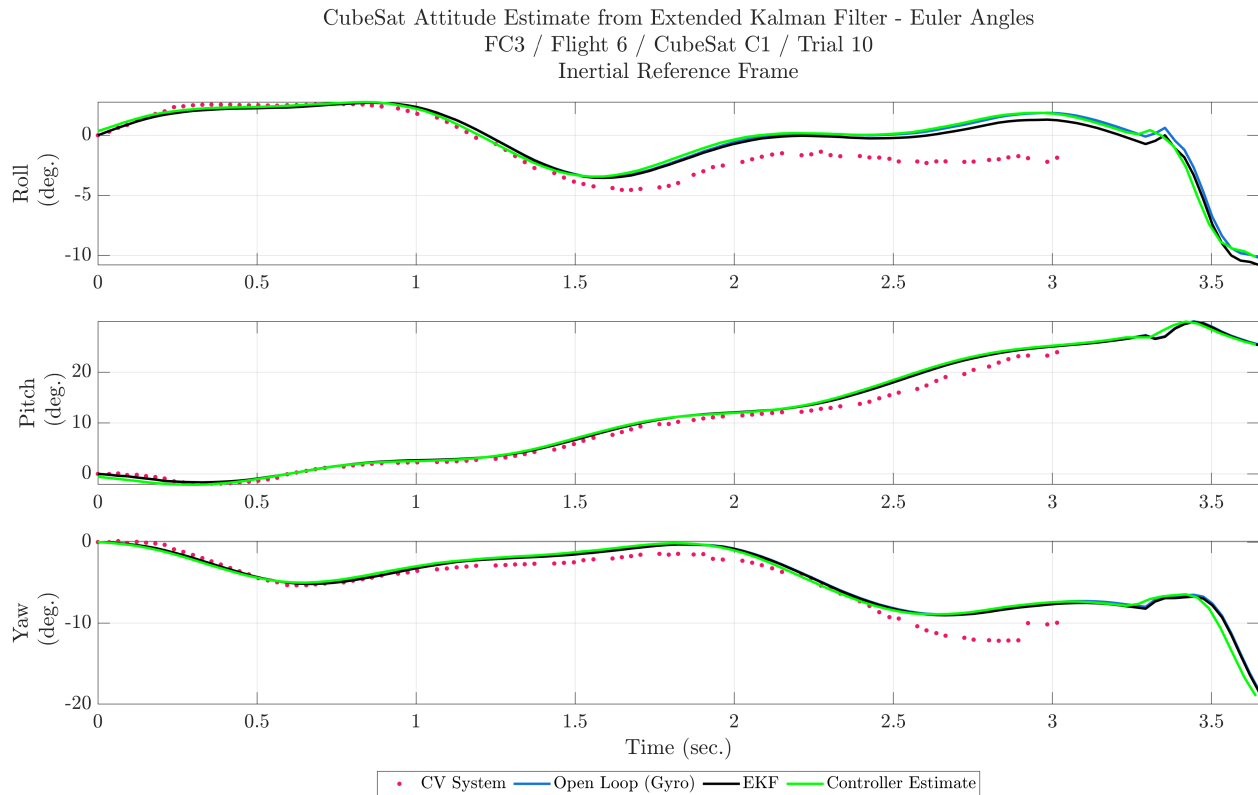


Figure 4.36: CubeSat testbed attitude (euler angles) estimated by EKF: Flight 6, CubeSat C1, Trial 10)

4.4 CubeSat Testbed Attitude Estimation Conclusions

This chapter presented the process for combining the CV system attitude estimates with the CubeSat testbed’s gyroscope readings to verify the testbed’s onboard attitude determination method. First, the CV pose estimates were transformed into the chamber reference frame and the pose estimates from each camera were compared against each other to verify that the transformations were performed correctly. Next, the chamber gyroscope data was converted into the chamber’s reference frame and the magnitude and direction of the measurements were verified against literature review. Then, the CV system attitude estimates were converted into the inertial reference frame by accounting for the aircraft’s rotation measured with the chamber gyroscope. The CV system attitude estimates were verified in the inertial reference frame by comparison against propagation of the CubeSat’s gyroscope readings over the experiment trial.

Once the CV attitude estimates were successfully transformed into the inertial reference

frame, they were combined with the testbed’s gyroscope readings in an Additive Extended Kalman Filter to produce a final attitude estimate of the CubeSat testbed over each of the selected trials. Physical testing of the CV system and the CubeSat testbed gyroscope characterized the uncertainty in both measurement sources. The EKF was then tuned based on the results of the uncertainty characterization tests, resulting in a smooth output that was robust to the CV system noise. The EKF successfully verified the CubeSat testbed attitude estimates that were fed into the testbed’s attitude controller, and provided a smoother attitude estimate for analysis of the HDD-RW performance. Verification of the CubeSat testbed’s attitude determination method supports the analysis of the HDD-RW performance in [1], which presents evidence for raising the TRL of the HDD-RW technology.

4.5 CubeSat Testbed Attitude Estimation Limitations

As described in Chapter 3, the CV system performance was dependent on multiple factors while in the parabolic flights, such as the CubeSat testbed’s distance and orientation relative to each camera, lighting conditions, motion blur, and marker occlusion. On-ground testing of the system in Section 3.4 demonstrated that the position error of the CubeSat testbed could be well-characterized as a function of distance and orientation; however, the attitude error was more difficult to characterize. Significant dropouts in the CV data were also observed due to motion blur, especially when the CubeSat floated into the chamber walls or the aircraft ground, which would cause it to bounce or twist suddenly.

Since the CV system attitude estimates were used as the measurement source in the EKF, the uncertainty, noise, and dropouts had to be accounted for. The CubeSat testbed’s onboard gyroscope proved more reliable than the CV system, and was therefore trusted more in the EKF tuning. While the CV data served its purpose of verifying the CubeSat testbed’s attitude determination method, improving the accuracy and reliability of the CV system would be very beneficial for future tests. Testing the EKF on longer duration trials would also be advised, since most of the parabolic flight trials were very short (3-5 seconds), based on the microgravity quality achieved by the flight provider. Finally, given additional time, it is recommended to implement a Multiplicative Extended Kalman Filter (MEKF) in replacement of the AEKF for more accurate attitude estimation [23].

Chapter 5

Conclusion

This chapter will first summarize the development of the Zero-G HDD-RW flight experiment and the accompanying CV system. Lessons learned are then presented with the intention of guiding future developers that are developing similar experiments or systems. Final remarks are then presented with regards to future work, followed by an evaluation of the TRL of the HDD-RW technology as the culmination of the Zero-G HDD-RW project.

5.1 Summary of Contributions

With the conclusion of the Zero-G HDD-RW project, the Technology Readiness Level of the HDD-RW technology has successfully been raised from TRL 4, component and/or breadboard validation in laboratory environment, to TRL 6, system/subsystem model or prototype demonstration in a relevant environment (ground or space). Although many challenges arose with testing in the Zero-G environment, such as unexpectedly short sustained floating periods, sufficient data has been gathered to demonstrate that the HDD-RWs are promising alternatives to commercial or in-house manufactured reaction wheels [1]. As a product of the Zero-G HDD-RW project, the HRVIP lab in the UC Davis Center for Spaceflight Research now has five fully functioning CubeSat testbeds and the software structure upon which the HDD-RWs and supporting attitude controllers can be further tested as the technology is prepared for future spaceflight opportunities.

While the computer vision system did experience significant measurement noise and dropouts during certain portions of the experiment, it was successfully used to produce atti-

tude estimates of the CubeSat testbeds in flight and to verify the CubeSat testbed's onboard attitude determination method. Fusion of the CubeSat's onboard gyroscope measurements and the computer vision system's attitude estimates into an Extended Kalman Filter produced a smooth final attitude estimate of the CubeSat testbed over each of the selected trials. On-ground characterization of the CV system's measurement accuracy and noise through testing on a UR5e robot arm proved very useful in tuning the EKF. The HRVIP lab is currently developing an air bearing table upon which the HDD-RWs can be further tested; the CV system used in the Zero-G project will serve as the foundation for the development of an external attitude determination system surrounding the testbed.

5.2 Lessons Learned

5.2.1 Experiment Methodology

Parabolic flight provided much less sustained floating time than initially expected, because the microgravity quality is dependent on the flight conditions in the airspace and on manual control by the aircraft pilots. While subtle variations in the microgravity quality may be acceptable for experiments that are bolted to the aircraft floor, such as fluids or heat transfer experiments, or for human subject testing and training, it has a greater impact on free-floating experiments such as the Zero-G HDD-RW project. Variations in the microgravity quality caused the CubeSat testbeds to have significant drift across the aircraft cabin, which would often end an experiment trial prematurely, due to the testbeds impacting the sides of the chamber, the aircraft walls, or the aircraft floor. This had a significant impact on the quality of the results that were collected; while the CubeSat testbed attitude controllers were initially tuned to react within the expected 10-15 second floating time, realistically, they had to react within 3-5 seconds before the CubeSat testbed would impact a nearby barrier. Having sustained floating periods is the most important factor in a successful CubeSat testbed attitude maneuver in parabolic flights; future developers are advised to consider the microgravity quality achieved in parabolic flight when assessing it as a potential test environment.

That being said, the key to success in the Zero-G HDD-RW experiments was on-ground preparation and experimenter training for the parabolic flight operations. While the ex-

periment operators had no control over the microgravity quality or the floating time of the CubeSats testbeds, extensive on-ground training allowed for seamless in-flight operations that maximized the number of experiment trials that were performed. Parabolic flights are a very dynamic environment, and the parabolas are performed back-to-back, giving little to no time for hardware or operations adjustment. The aircraft environment is also very loud during the pulls and transition periods, so parabola callouts were often not heard by all team members. Hand signals were implemented to ensure that everyone was aware of all parabola callouts at all times.

Minimizing head movement during the pulls and transition periods of the parabola, as well as using prescription scopolamine patches, significantly reduced the motion sickness experienced by experiment operators. However, in the event that any experimenter experienced motion sickness and needed to step away from the experiment, all other experimenters were cross-trained in all roles and were prepared to take over the additional responsibilities.

5.2.2 Computer Vision System Design

Camera calibration was found to be the most important step in ensuring accurate ArUco marker detection for this project. While processing the videos from FC1, it became apparent that the focus for the selected Arducam 12MP cameras changed with the varying gravity levels of the parabolic flight. While the focus was tuned on-ground to be clear in 1g, the cameras would become slightly blurry during the 1.8g or 0g periods of flight, making ArUco detection much more difficult. FC2 and FC3 flight operations addressed this by tuning the camera focus value on the touch screens to be clear in 0g. Thus, the calibration process needed to also be performed in 0g to accurately estimate the camera calibration parameters during the experiment trials.

5.2.3 CubeSat Testbed In-Flight Attitude Estimation and Validation

Upon processing the CV system data from the Zero-G HDD-RW flight experiments, it became clear that the system experienced more measurement noise and dropouts than expected from ground testing. This was most noticeable when the CubeSat testbeds were moving quickly in translation or rotation, such as when the testbed drift rate in the aircraft

was fast due to the microgravity quality, when the CubeSat testbeds were deployed with too high of a rotational velocity during stabilization tests, or after impacting a barrier such as the chamber straps, the aircraft walls, or the aircraft floor. Having redundancy in the system (i.e. four cameras recording the chamber experiment instead of one) helped to mitigate this issue; however, for future experiments, it is advised to also characterize the translational and rotational velocity thresholds at which ArUco marker detection drops out.

5.3 Future Work

Looking to the future, the next steps in raising the TRL of the HDD-RW technology are to perform thorough environmental testing of the HDD-RWs and to perform an on-orbit CubeSat attitude control demonstration with the HDD-RWs. During the development of the Zero-G HDD-RW project, a single-axis HDD-RW payload was also designed by the Zero-G HDD-RW team and delivered to NASA Johnson Space Center (JSC). The single-axis HDD-RW payload will be integrated as a secondary payload on a NASA JSC R5 CubeSat, to be launched in 2024. Successful mission operations onboard the R5 CubeSat will raise the TRL of the HDD-RW technology to 8. Table 5.1 below paints a picture of the technology's current status after the completion of the Zero-G HDD-RW project, and the path forward to raise the technology's readiness level to the maximum value of 9. The Zero-G HDD-RW project has proven the HDD-RWs to be promising alternatives to commercial and in-house manufactured reaction wheels; with additional testing, the HDD-RWs can mature into a viable option for low-budget or rapid development CubeSat missions.

Table 5.1: TRL evaluation of HDD-RW technology after the completion of the Zero-G HDD-RW project

TRL	Definition	HDD Reaction Wheel Development Timeline	TRL Met?
1	Basic principles observed and reported	Observed that HDDs have similar components (motor + flywheel), size, and momentum storage to industry-standard CubeSat reaction wheels	Yes
2	Technology concept and/or application formulated	Developed the concept of repurposing HDDs as CubeSat reaction wheels Performed literature review to assess the status of HDD-RWs Performed market analysis to confirm the technology's need	Yes
3	Analytical and experimental critical function and/or characteristic proof-of-concept	Replaced HDD ESC to achieve bidirectional motor spin at variable speeds Performed 1 rotational DOF fishing line stabilization and pointing demonstrations with each size HDD-RW. Rotational DOF was aligned with HDD-RW's spindle axis.	Yes
4	Component and/or breadboard validation in laboratory environment	Integrated 3 identical HDD-RWs of each size into CubeSat testbeds to provide 3 axis control. Performed stabilization and pointing demonstrations with each CubeSat testbed around arbitrary axes aligned with a fishing line. (1 DOF maneuvers that require up to 3 HDD-RWs acting together)	Yes

Continued on next page

Table 5.1: TRL evaluation of HDD-RW technology after the completion of the Zero-G HDD-RW project (Continued)

5	Component and/or breadboard validation in relevant environment	Zero-G Flight Campaign 1: 3-axis ramp tests with HDD-RWs in a microgravity environment. No stabilization or pointing tests performed. CubeSat testbeds consisted of proto boards, and preliminary electrical design Short duration vacuum tests performed with no failures.	Yes
6	System/subsystem model or prototype demonstration in a relevant environment (ground or space)	Zero-G Flight Campaign 2: 3-axis stabilization tests performed with prototype CubeSats and each size HDD-RW Zero-G Flight Campaign 3: 3-axis pointing tests performed with prototype CubeSats and each size HDD HDD-RW ESCs changed, electrical system matured into PCBs	Yes
7	System prototype demonstration in a space environment	Single axis HDD-RW payload integrated on NASA JSC CubeSat Vibration tests performed on each HDD-RW size, with no failures	No (In Progress)
8	Actual system completed and “flight qualified” through test and demonstration (ground or space)	Single axis HDD-RW test performed in space onboard NASA JSC CubeSat, with no failures observed Long-duration vacuum tests performed on each HDD-RW size, with no failures	No

Continued on next page

Table 5.1: TRL evaluation of HDD-RW technology after the completion of the Zero-G HDD-RW project (Continued)

9	Actual system “flight proven” through successful mission operations	HDD-RWs integrated into a CubeSat for full 3-axis control HDD-RWs demonstrate essential CubeSat ADCS functions (pointing, stabilization) No failures from observed on-orbit testing HDD-RWs are ready for integration into future missions	No
---	--	--	----

BIBLIOGRAPHY

- [1] Abhay Negi, “CubeSat Attitude Control Using Hard Disk Drives as Reaction Wheels,” Master’s thesis, University of California, Davis, 2023.
- [2] *NASA Systems Engineering Handbook*, Dec. 2007, nTRS Report/Patent Number: NASA/SP-2007-6105 Rev1 NTRS Document ID: 20080008301 NTRS Research Center: Headquarters (HQ). [Online]. Available: <https://ntrs.nasa.gov/citations/20080008301>
- [3] J. Schwartz, M. Peck, and C. Hall, “Historical Review of Air-Bearing Spacecraft Simulators,” *Journal of Guidance, Control, and Dynamics*, vol. 26, May 2003.
- [4] “STMD Flight Opportunities - NASA,” section: Space Technology Mission Directorate. [Online]. Available: <https://www.nasa.gov/stmd-flight-opportunities/>
- [5] “NASA Selects 31 Promising Space Technologies for Commercial Flight Tests - NASA,” Oct. 2020, section: Ames Research Center. [Online]. Available: <https://www.nasa.gov/humans-in-space/commercial-space/nasa-selects-31-promising-space-technologies-for-commercial-flight-tests/>
- [6] Zero-G Corp., “The Zero-G Experience.” [Online]. Available: <https://www.gozerog.com/the-zero-g-experience/>
- [7] F. Karmali and M. Shelhamer, “The dynamics of parabolic flight: flight characteristics and passenger percepts,” *Acta astronautica*, vol. 63, no. 5-6, pp. 594–602, Sep. 2008. [Online]. Available: <https://www.ncbi.nlm.nih.gov/pmc/articles/PMC2598414/>
- [8] M. Kalaitzakis, B. Cain, S. Carroll, A. Ambrosi, C. Whitehead, and N. Vitzilaios, “Fiducial Markers for Pose Estimation: Overview, Applications and Experimental Comparison of the ARTag, AprilTag, ArUco and STag Markers,” *Journal of Intelligent & Robotic Systems*, vol. 101, no. 4, p. 71, Apr. 2021. [Online]. Available: <https://link.springer.com/10.1007/s10846-020-01307-9>
- [9] G. Yu, Y. Hu, and J. Dai, “TopoTag: A Robust and Scalable Topological Fiducial Marker System,” *IEEE Transactions on Visualization and Computer Graphics*, vol. 27, no. 9, pp. 3769–3780, Sep. 2021, conference Name: IEEE Transactions on Visualization and Computer Graphics.
- [10] “ar_track_alvar - ROS Wiki.” [Online]. Available: http://wiki.ros.org/ar_track_alvar#ar_track_alvar.2Fpost-fuerte.Generating_AR_tags
- [11] “AprilTag.” [Online]. Available: <https://april.eecs.umich.edu/software/apriltag>
- [12] “OpenCV: Detection of ArUco Markers.” [Online]. Available: https://docs.opencv.org/4.x/d5/dae/tutorial_aruco_detection.html
- [13] C. Ricolfe-Viala and A. Esparza, “The Influence of Autofocus Lenses in the Camera Calibration Process,” *IEEE Transactions on Instrumentation and Measurement*, vol. 70, pp. 1–15, 2021, conference Name: IEEE Transactions on Instrumentation and Measurement.

- [14] J. W. Day, “Development of a Two-Fault Tolerant Cold Gas Propulsion System and Air Bearing Testbed for Application to a Spacecraft-Inspection CubeSat,” Master’s thesis, University of California, Davis, 2020.
- [15] GoPro, “GoPro Hero 7 Datasheet.” [Online]. Available: https://gopro.com/content/dam/help/hero7-black/manuals/HERO7Black_UM_ENG_REVA.pdf
- [16] “Logitech C920 PRO HD Webcam, 1080p Video with Stereo Audio.” [Online]. Available: <https://www.logitech.com/en-ch/products/webcams/c920-pro-hd-webcam.html>
- [17] Raspberry Pi, “Raspberry Pi Camera Module V2 Datasheet.” [Online]. Available: <http://cdn.sparkfun.com/datasheets/Dev/RaspberryPi/RPiCamMod2.pdf>
- [18] —, “Raspberry Pi High Quality Camera Datasheet,” Apr. 2020. [Online]. Available: https://static.raspberrypi.org/files/product-briefs/Raspberry_Pi_HQ_Camera_Product_Brief.pdf
- [19] Arducam, “Arducam 12MP 477P Autofocus High Quality Camera for Raspberry Pi.” [Online]. Available: <https://www.arducam.com/product/arducam-12mp-imx477-motorized-focus-high-quality-camera-for-raspberry-pi/>
- [20] G. R. Bradski and A. Kaehler, *Learning OpenCV: computer vision with the OpenCV library*, 1st ed., ser. Software that sees. Beijing: O’Reilly, 2011.
- [21] A. Hazard and F. Persson, “Camera Pose Estimation and Multiview 2D to 3D Reconstruction,” Master’s thesis, Chalmers University of Technology, Gothenburg, Sweden, 2022.
- [22] A. Anwar, “What are Intrinsic and Extrinsic Camera Parameters in Computer Vision?” Mar. 2022. [Online]. Available: <https://towardsdatascience.com/what-are-intrinsic-and-extrinsic-camera-parameters-in-computer-vision-7071b72fb8ec>
- [23] F. L. Markley, “Multiplicative vs. Additive Filtering for Spacecraft Attitude Determination.”

Appendices

Appendix A

Experiment Design

A.1 CubeSat Testbed Electrical Schematics

A.1.1 CubeSat Testbed A

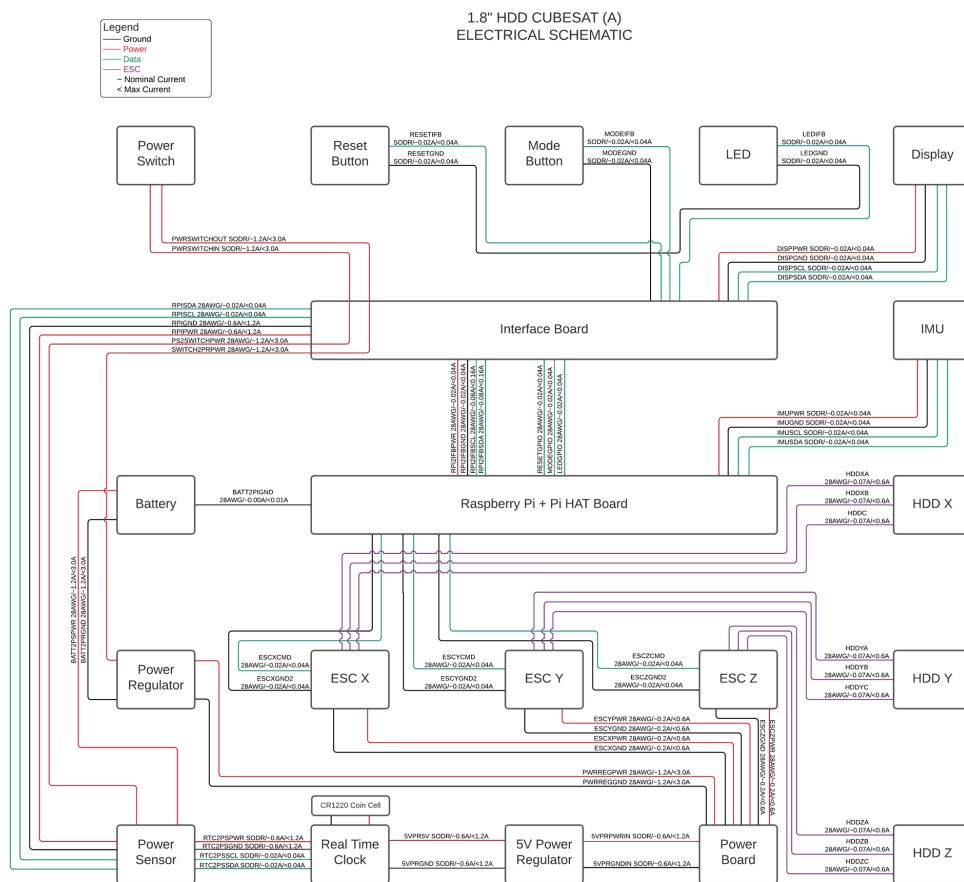


Figure A.1: CubeSat Testbed A Electrical Schematic

CubeSat Testbed B

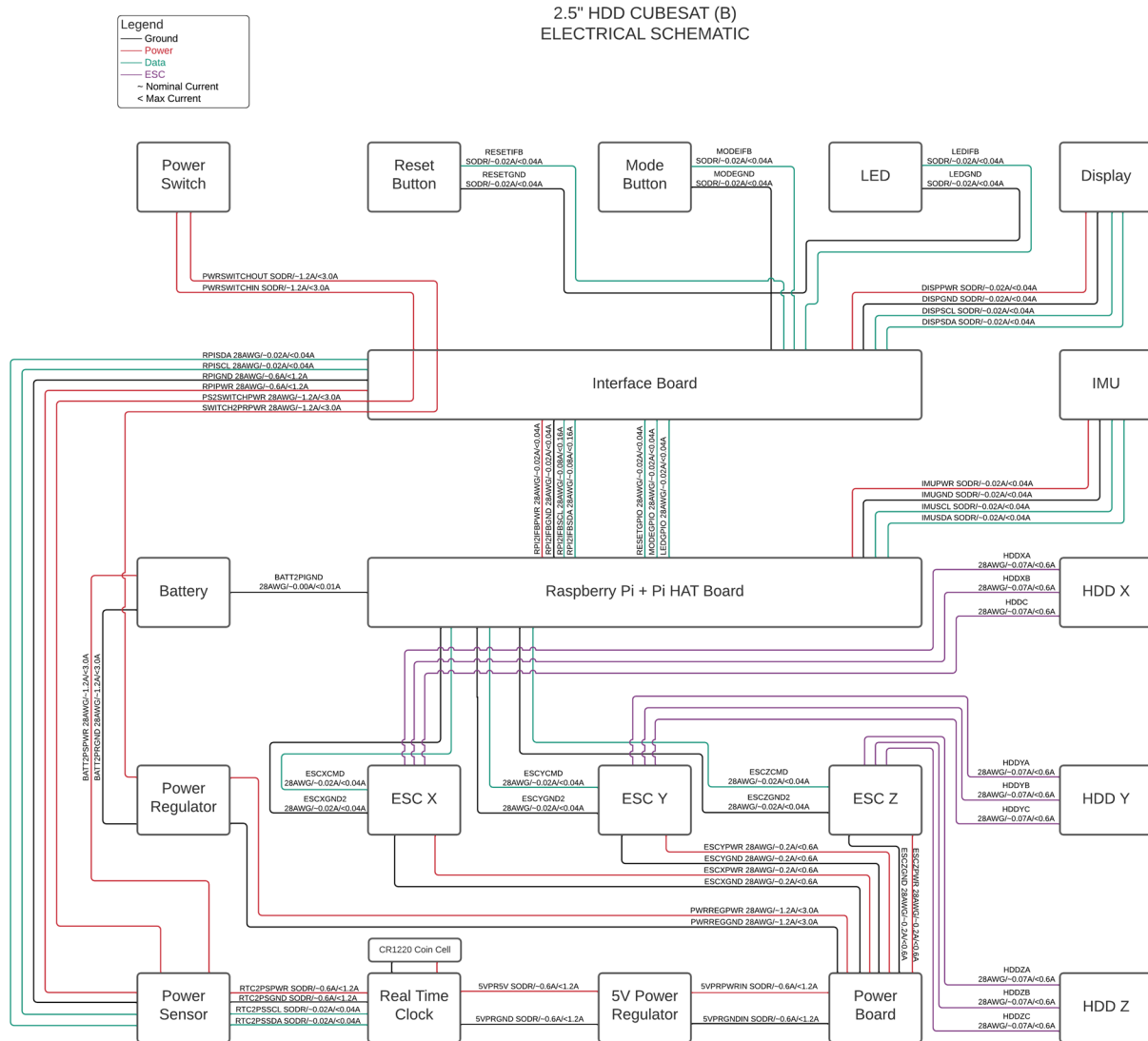


Figure A.2: CubeSat Testbed B Electrical Schematic

CubeSat Testbeds C1 & C2

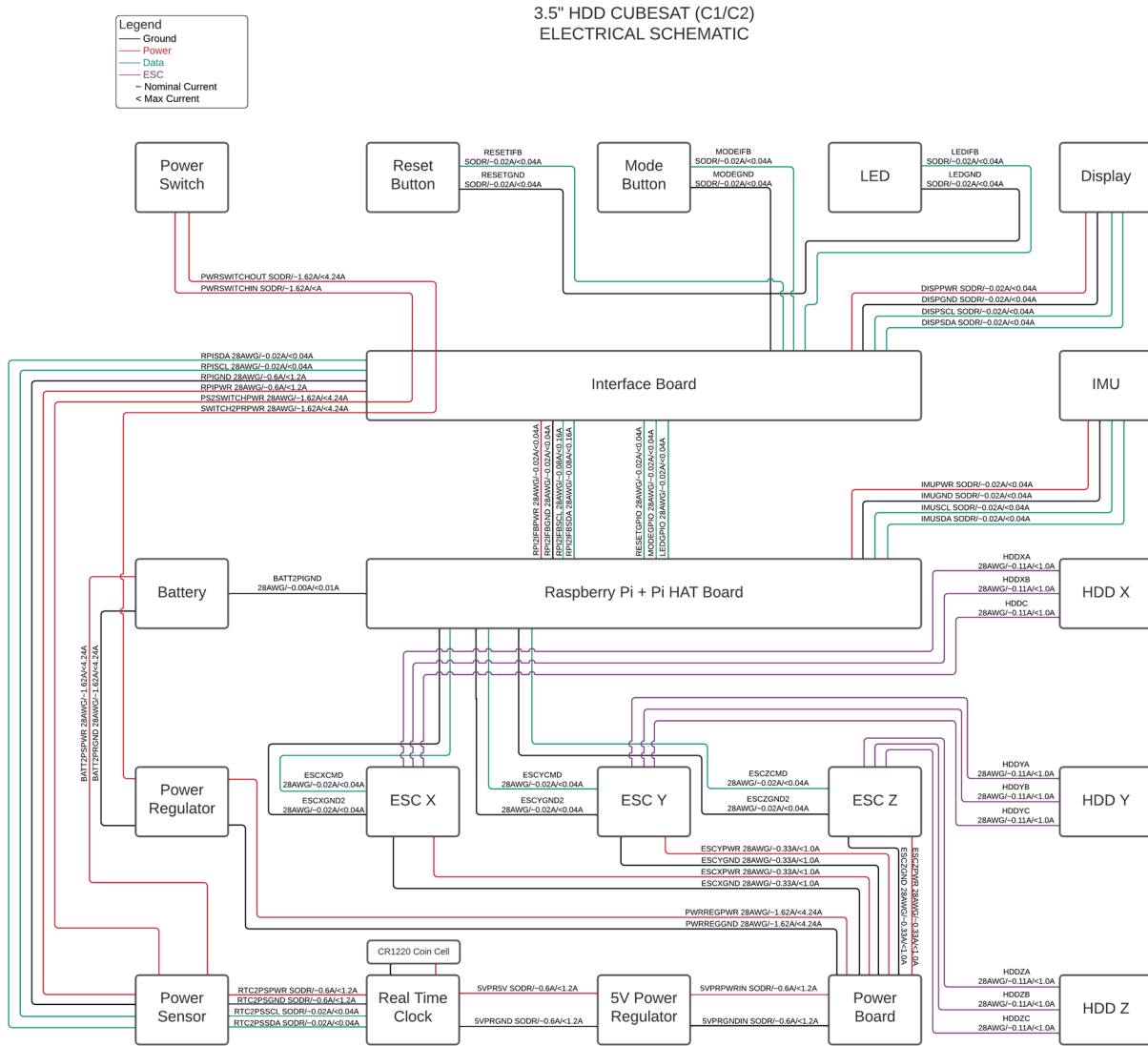


Figure A.3: CubeSat Testbed C1 & C2 Electrical Schematic

A.2 Chamber Drawings

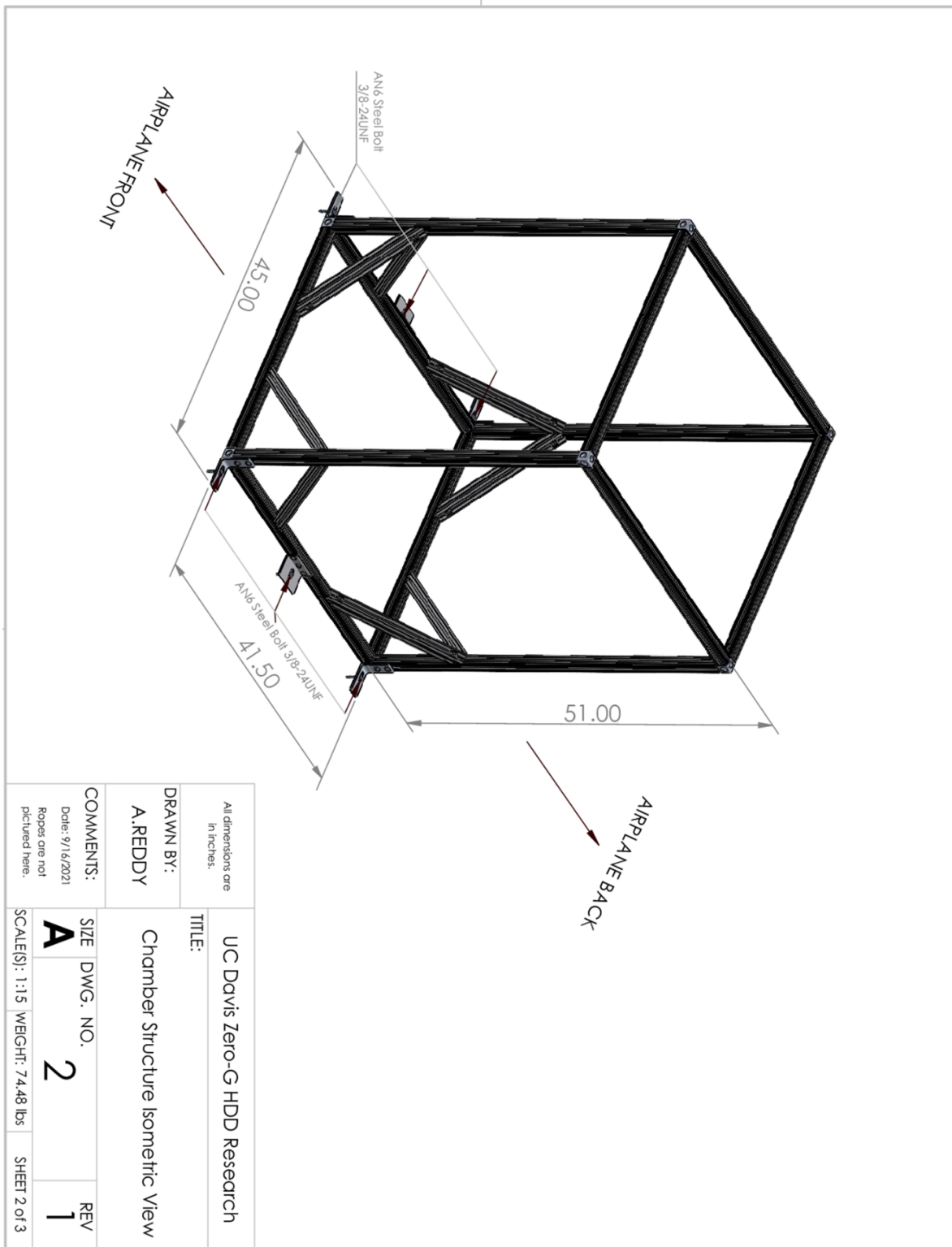


Figure A.4: Chamber Isometric View

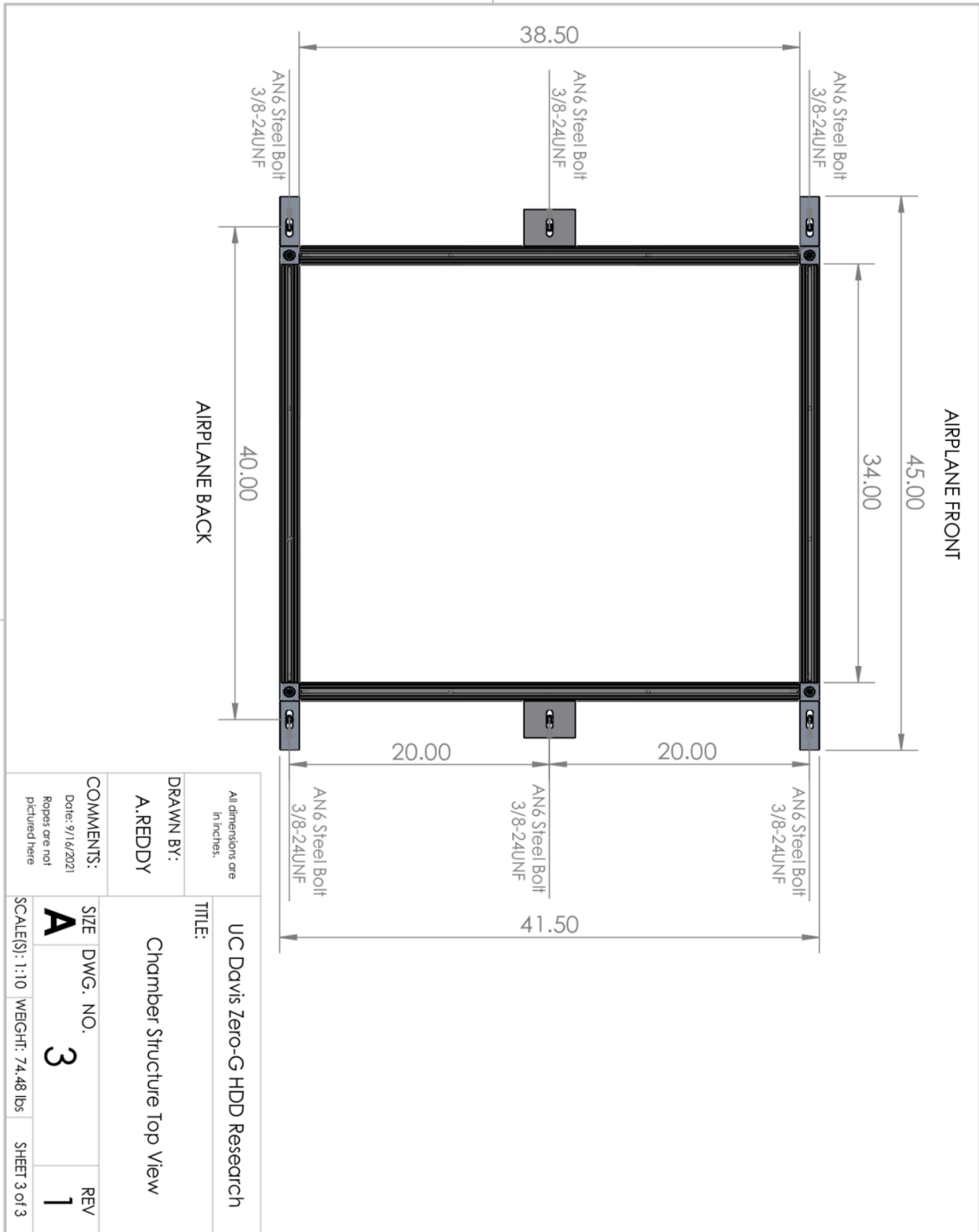


Figure A.5: Chamber Top View

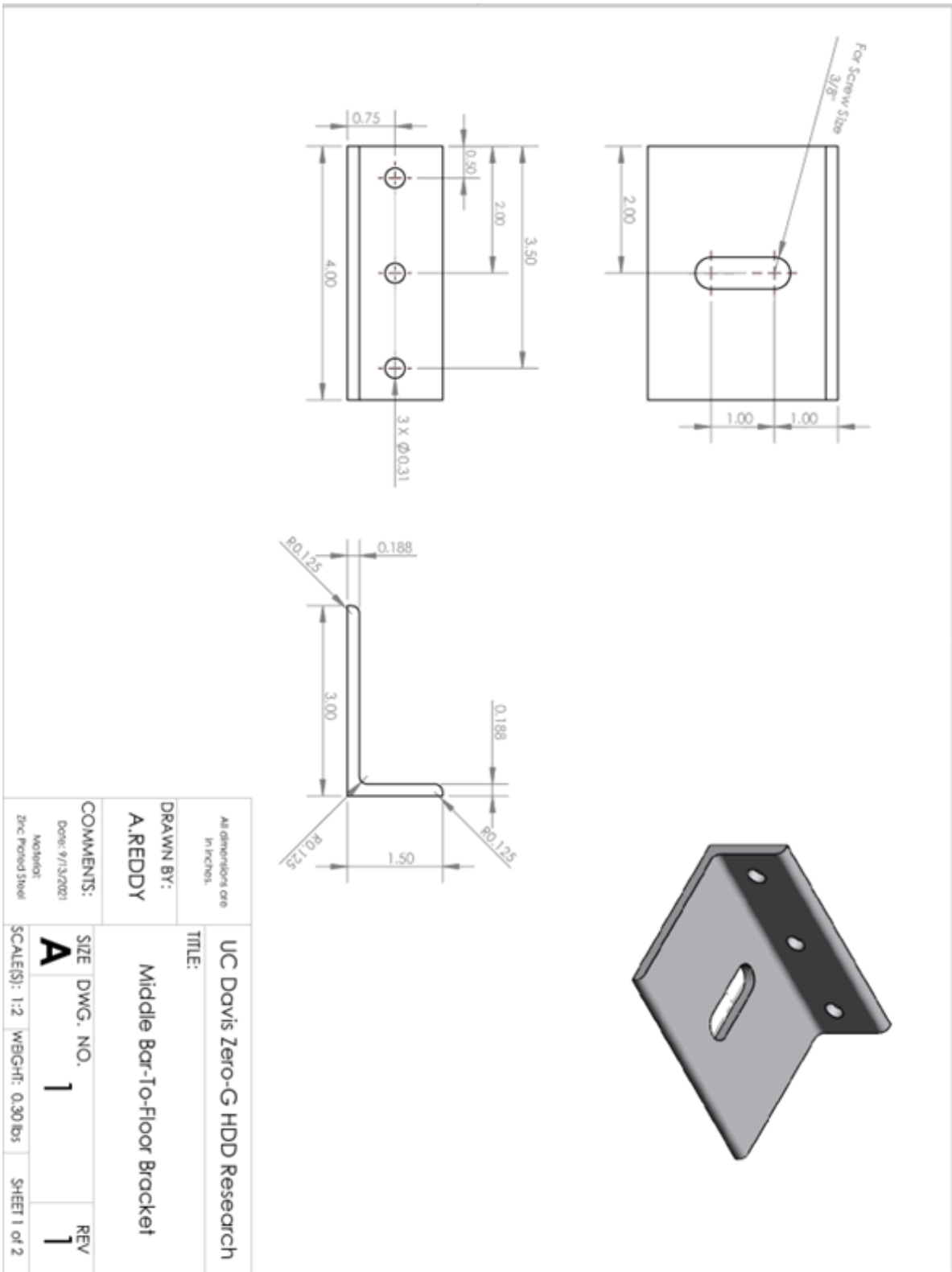


Figure A.6: Chamber Middle Bracket

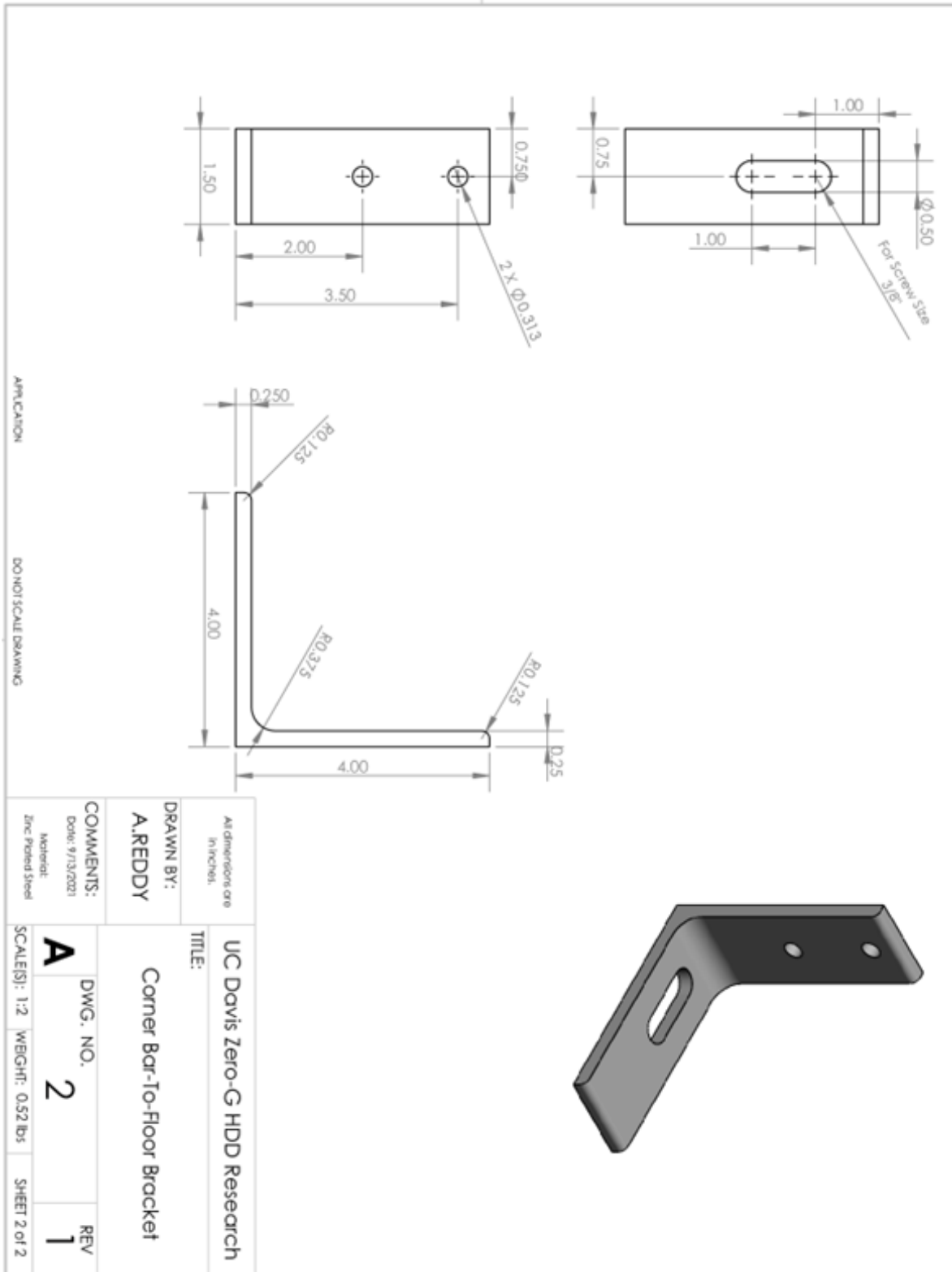


Figure A.7: Chamber Corner Bracket

A.3 CV System Electrical Schematics

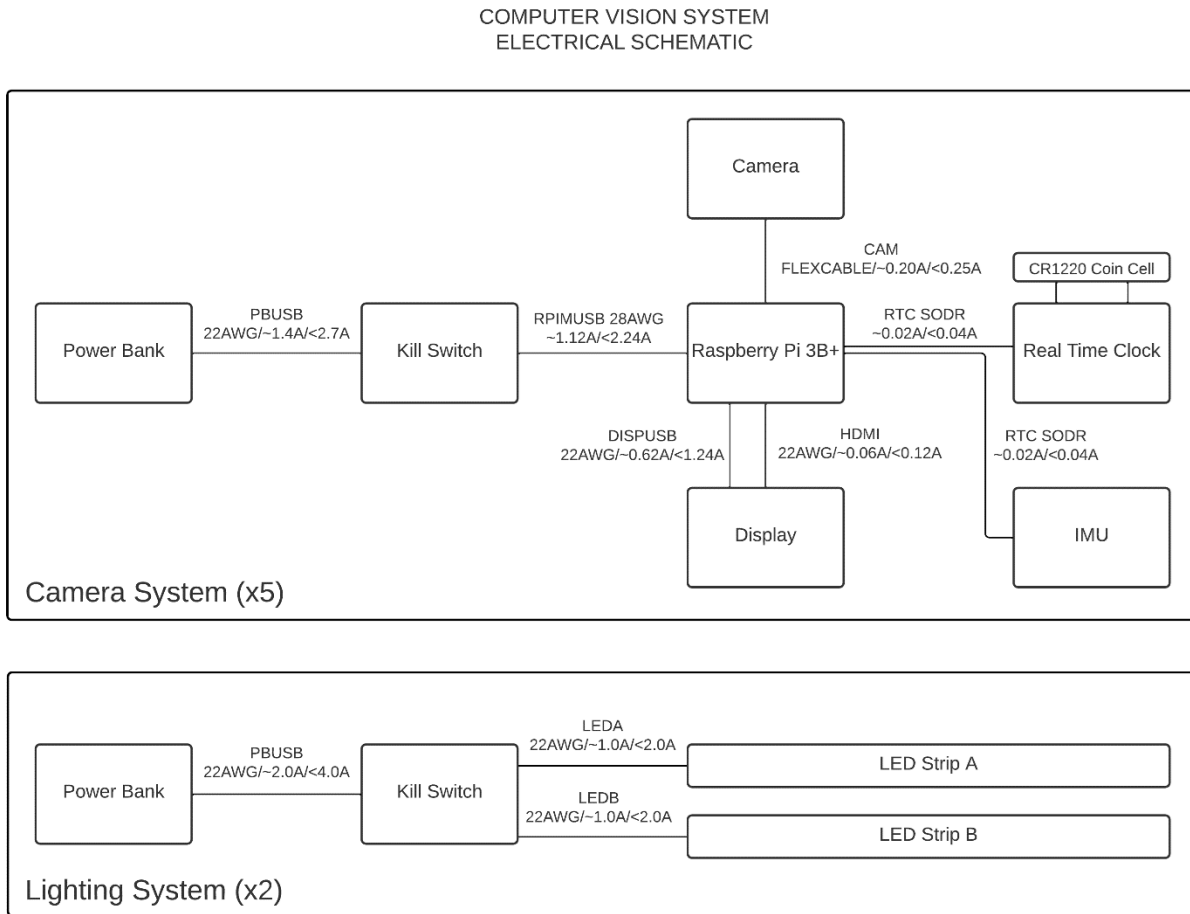


Figure A.8: CV System Electrical Schematic

Appendix B

Extended Kalman Filter Design

B.1 Matrix A Definition

$$A_{1,1} = 1/\mathbf{q} - (q_0(q_0 - (\Delta t(q_1\omega_x + q_2\omega_y + q_3w_z))/2))/\mathbf{q}^3 \quad (\text{B.1})$$

$$A_{1,2} = -(\Delta t\omega_x)/(2\mathbf{q}) - (q_1(q_0 - (\Delta t(q_1\omega_x + q_2\omega_y + q_3w_z))/2))/\mathbf{q}^3 \quad (\text{B.2})$$

$$A_{1,3} = -(\Delta t\omega_y)/(2\mathbf{q}) - (q_2(q_0 - (\Delta t(q_1\omega_x + q_2\omega_y + q_3w_z))/2))/\mathbf{q}^3 \quad (\text{B.3})$$

$$A_{1,4} = -(\Delta tw_z)/(2\mathbf{q}) - (q_3(q_0 - (\Delta t(q_1\omega_x + q_2\omega_y + q_3w_z))/2))/\mathbf{q}^3 \quad (\text{B.4})$$

$$A_{2,1} = (\Delta t\omega_x)/(2\mathbf{q}) - (q_0(q_1 + (\Delta t(q_0\omega_x - q_3\omega_y + q_2w_z))/2))/\mathbf{q}^3 \quad (\text{B.5})$$

$$A_{2,2} = 1/\mathbf{q} - (q_1(q_1 + (\Delta t(q_0\omega_x - q_3\omega_y + q_2w_z))/2))/\mathbf{q}^3 \quad (\text{B.6})$$

$$A_{2,3} = (\Delta tw_z)/(2\mathbf{q}) - (q_2(q_1 + (\Delta t(q_0\omega_x - q_3\omega_y + q_2w_z))/2))/\mathbf{q}^3 \quad (\text{B.7})$$

$$A_{2,4} = -(\Delta t \omega_y)/(2\mathbf{q}) - (q_3(q_1 + (\Delta t(q_0 \omega_x - q_3 \omega_y + q_2 w_z))/2))/\mathbf{q}^3 \quad (\text{B.8})$$

$$A_{3,1} = (\Delta t \omega_y)/(2\mathbf{q}) - (q_0(q_2 + (\Delta t(q_3 \omega_x + q_0 \omega_y - q_1 w_z))/2))/\mathbf{q}^3 \quad (\text{B.9})$$

$$A_{3,2} = -(\Delta t w_z)/(2\mathbf{q}) - (q_1(q_2 + (\Delta t(q_3 \omega_x + q_0 \omega_y - q_1 w_z))/2))/\mathbf{q}^3 \quad (\text{B.10})$$

$$A_{3,3} = 1/\mathbf{q} - (q_2(q_2 + (\Delta t(q_3 \omega_x + q_0 \omega_y - q_1 w_z))/2))/\mathbf{q}^3 \quad (\text{B.11})$$

$$A_{3,4} = (\Delta t \omega_x)/(2\mathbf{q}) - (q_3(q_2 + (\Delta t(q_3 \omega_x + q_0 \omega_y - q_1 w_z))/2))/\mathbf{q}^3 \quad (\text{B.12})$$

$$A_{4,1} = (\Delta t w_z)/(2\mathbf{q}) - (q_0(q_3 + (\Delta t(q_1 \omega_y - q_2 \omega_x + q_0 w_z))/2))/\mathbf{q}^3 \quad (\text{B.13})$$

$$A_{4,2} = (\Delta t \omega_y)/(2\mathbf{q}) - (q_1(q_3 + (\Delta t(q_1 \omega_y - q_2 \omega_x + q_0 w_z))/2))/\mathbf{q}^3 \quad (\text{B.14})$$

$$A_{4,3} = -(\Delta t \omega_x)/(2\mathbf{q}) - (q_2(q_3 + (\Delta t(q_1 \omega_y - q_2 \omega_x + q_0 w_z))/2))/\mathbf{q}^3 \quad (\text{B.15})$$

$$A_{4,4} = 1/\mathbf{q} - (q_3(q_3 + (\Delta t(q_1 \omega_y - q_2 \omega_x + q_0 w_z))/2))/\mathbf{q}^3 \quad (\text{B.16})$$